Interfacial Effects in Viscoplastic Lubrication Flows

by

Geoffrey E. Dunbrack

BASc, The University of British Columbia, 2011

A THESIS SUBMITTED IN PARTIAL FULFILLMENT OF
THE REQUIREMENTS FOR THE DEGREE OF

MASTER OF APPLIED SCIENCE

in

The Faculty of Graduate Studies

(Mechanical Engineering)

THE UNIVERSITY OF BRITISH COLUMBIA

(Vancouver)

August 2013

Abstract

Poiseuille flows with yield stress fluids produce an unyielded central plug which can act as a solid conduit surrounding central (core) flows of Newtonian or power law fluids. Effectively, the annular yield stress fluid acts as a lubricant that isolates the core flow from wall friction. Stable flows with a yield stress annular fluid and a Newtonian or power law core fluid are termed viso-plastic lubrication (VPL) flows. This study examined interfacial effects in vertical VPL Poiseuille flows using a carbopol solution as the annular (yield stress) fluid and xanthan (inelastic shear thinning fluid) or polyethlyeneoxide (PEO; an elastic shear thinning fluid) as the core fluids. Experiments with the inelastic core fluid (xanthan) involved introducing stepped (high to low) or pulsed (high to low to high) changes in the core flow to an established stable VPL flow. Step changes produced a "yield front" (narrowing of the core flow or "interfacial radius") that propagated upward at a velocity considerably greater than the velocity of the annular carbopol plug but close to the average velocity of the xanthan core flow following the step change. Pulsed changes in the core flow produced one of three outcomes depending on the magnitude of the flows preceding and following the step change: (1) a stable ("frozen in") deformation in the carbopol/xanthan interface that moved upward at the velocity of the carbopol plug,(2) no persistent deformation of the interface, or (3) a breakdown of the stable VPL flow characterized by extensive mixing of the core and annular flows. Experiments with the elastic core fluid (PEO) involved introducing multiple pulsed changes (high/low/high, high/low/high, ...) in the core flow to an established VPL flow. These pulsed changes typically produced linked multiple diamond shaped stable deformations ("diamond necklace") in the interface that moved upwards at the velocity of the carbopol plug. The frequency and amplitude (maximum radius) of the diamond deformations could be controlled by the timing of pulses and the respective flow rates, but not the diamond shape itself which appears to be a consequence of the complex rheology of the fluids.

Preface

I carried out all the fluid preparation, experiments, rheological testing, experimental data analysis, Arduino programming, and built the solenoid valve bypass system. All experimental results have been presented at the 2012 Nordic Rheology Society conference in Oslo, Norway and at the 2013 Technical Forum on Unconventional Natural Gas in Victoria, BC, Canada. Preliminary results have been published in [6].

Table of Contents

Appendices

List of Tables

List of Figures

Acknowledgements

I would like to thank Dr. Sarah Hormozi for her training in the lab, helpful insights, and logical suggestions, my supervisor, Professor Ian Frigaard, for his research vision, funding, and clear and helpful suggestions over the past two years, and my father, Professor Robert Dunbrack, for his interest, wisdom and support. The experimental apparatus was built by Billy Fung and Ryan Yee in Sept 2010- Sept 2011 under supervision of Dr Sarah Hormozi. The following people were also very helpful to me during this research:

- Dr. Kamran Alba
- Dr. Mohammed Taghavi
- Gustavo Moises

This research was made possible by the funding of NSERC and Slumberger.

Chapter 1

Introduction to Subject

Figure 1.1 shows a schematic of the type of fluid flow studied in this thesis. The main features of this flow are:

1. Poiseuille flow, driven by a pressure gradient.
2. Pipe flow, inside a cylindrical pipe.
3. Core-annular flow, also called concentric flow, and multilayer pipe flow.
4. Iso density, both fluids have the same density.

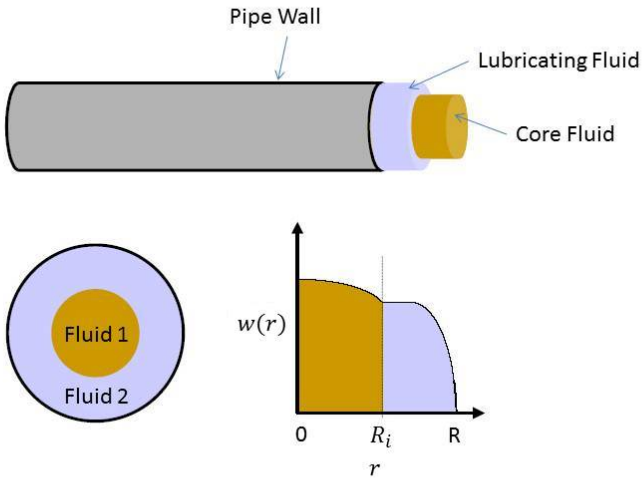

Figure 1.1: Schematic core annular pipe flow.

$w(r)$ is the axial component of velocity as a function of distance from the center (r). The slope of the axial velocity profile changes slope abruptly. This point is known as the 'interface' and is located at the 'interfacial radius' R_i. The abrupt change in slope is caused by the discontinuity in fluid properties across the interface.

A variety of different models exist to express the properties of fluids. These models are called constitutive equations. It must be acknowledged that no constitutive model can fully explain the behaviour of a fluid under all conditions. Constitutive models must be selected that explain the fluid behaviour within the region of interest for the study and that do not complicate the problem to the point of being so complex as to cloud the main phenomena. In this thesis, we use the 'Herschel-Bulkley' model, equation (1.1).

$$|\tau_{ij}| = |\tau_{rz}| = \tau = \tau_y + \kappa\dot{\gamma}^n \tag{1.1}$$

In the 1D pipe flow model we use to model the flow studied, the non zero term of the stress tensor is stress is $|\tau_{rz}|$. The strain rate in this scenario is $\dot{\gamma} = \frac{\partial w}{\partial r}$. τ_y is the yield stress (defined here as the stress at highest effective viscosity). The indices i,j correspond to directions of the stress tensor, defined in cylindrical co-ordinates in this thesis:

$$\begin{pmatrix} \tau_{11} & \tau_{12} & \tau_{13} \\ \tau_{21} & \tau_{22} & \tau_{23} \\ \tau_{31} & \tau_{32} & \tau_{33} \end{pmatrix} = \begin{pmatrix} \tau_{rr} & \tau_{r\theta} & \tau_{rz} \\ \tau_{\theta r} & \tau_{\theta\theta} & \tau_{\theta z} \\ \tau_{zr} & \tau_{z\theta} & \tau_{zz} \end{pmatrix}$$

The stress tensor is not used in derivations since we are dealing with a single non zero stress direction. The Herschel-Bulkley model becomes the power law model when $\tau_y \to 0$, which is what is used for the non-yield stress fluids we have studied.

1.1 Interfacial Instabilities

A fluid fluid interface with viscosity stratification across it is inherently unstable in many situations[3],[4],[13]. Perturbations will grow over time and lead to mixing of the two fluids. In terms of industrial applications of multi-layer flows, mixing of the two fluids lowers the quality of products and limits the production rate, as flow rates would have to be kept low to minimize mixing. The mechanism of instability across an interface with viscosity stratification is as follows:

1. An initially stable interface is perturbed by a fluctuation in flow rate.

2. The interface is perturbed away from the original equilibrium position.
3. Fluids on either side of the boundary experience a change in shear stress and accelerate according to their different viscosities.
4. The less viscous fluid responds to the perturbation by accelerating faster than the more viscous fluid.
5. The difference in velocities caused by unequal acceleration across the interface promotes vortices which cause further instability growth.

This is a classic instability and is shown in figure 1.2. Additional mechanisms of instability exist but are left out of this discussion because stability analysis is not a main focus of this thesis.

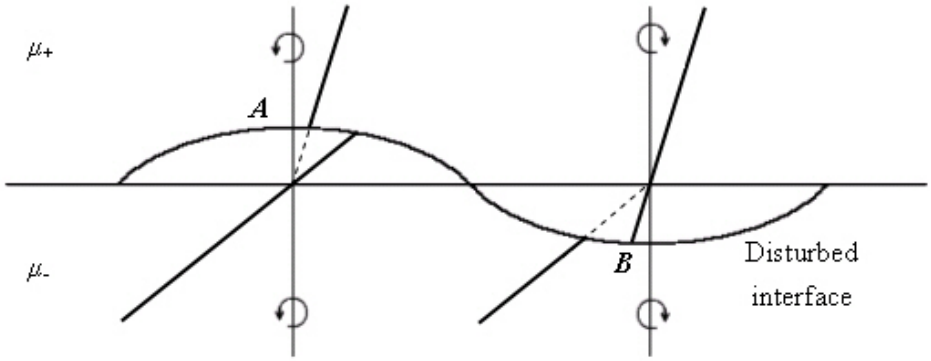

Figure 1.2: Classic viscous-viscous instability.

1.2 Stability of Multilayer Flows

Hickox [3]focused on concentric (core annular) multilayer flows in a pipe with two fluids of different viscosity and density. The stability was studied by introducing a change in flow rate that results in an alteration of the interfacial radius. By linearizing the Navier Stokes equations and applying a method that introduced long wave, small perturbations, Hickox found that even at small Reynolds numbers $\sim O(1)$, there was no evidence that the interface could remain stable indefinitely. Axisymetric (and asymetric) perturbations introduced to viscous-viscous core annular flows will initially grow at an exponential within the area close to equilibrium. This study was done using two newtonian fluids of different viscosity.

If a yield stress fluid is used as the lubricating fluid, the long wave instabilities studied in [3] can be eliminated. Essentially, the fluid-fluid interface is transformed into a fluid-solid interface that stabilizes the flow. The idea of using a yield stress lubricating fluid was first introduced in [2] in a paper that studied the linear stability of core annular 'visco-plastically lubricated' (VPL) flows. It has been demonstrated experimentally that VPL flows would be stable up to the point where the shear stress at the interface exceeds the yield stress of the lubricating fluid [10]. Compared to their purely viscous analogues, VPL flows are resistant to linear instabilities, even at moderate Reynolds number. This was a promising result suggesting that multi layers flows can be made stable. Frigaard ([2]) studied VPL flows in channel flows but the experimental work in this thesis is done on pipe flows. In addition, the practical use of linear stability analysis is low if this stability analysis cannot be extended into the non-linear regime.

The non-linear stability of VPL flows in ducts was studied in [11] where it was suggested that VPL flows can be stable under perturbations that displace the position of the interface a small distance away from an equilibrium position. This stability was seen to persist in some situations up to the same order of Reynolds number commonly seen in Newtonian pipe flows. Although not directly applicable to this research, this is an interesting result because it provides strong evidence that VPL flows can remain stable in experimental and industrial applications, where perturbations cannot be completely eliminated. An additional study in [12] showed that VPL flows are stable up to very high Reynolds numbers when a Carreau fluid is used as the core fluid. The effective viscosity of a Carreau fluid is:

$$\eta = \mu_{\text{inf}} + (\mu_0 - \mu_{\text{inf}})(1 + (\lambda\dot{\gamma})^2)^{\frac{n-1}{2}}$$

where μ_{inf} is the viscosity at infinite shear rate, μ_0 is the viscosity at zero shear rate, and λ is the relaxation time. A Carreau fluid behaves as both a power law and a newtonian fluid depending on the shear rate. A wide range of core fluids were also expected to be able to produce stable core annular flow when surrounded by an un-yielded plug. It was also noted in [12] that by choosing a high enough value for the lubricating fluid flow rate, the Couette component superimposed on the core fluid by the resulting interfacial velocity can increase the stability. It was demonstrated experimentally that a power law, shear thinning core fluid ($n < 1$) will produce stable flows within a pipe [10] that persist for 100s of pipe diameters.

Further work on the stability of VPL flows in pipes was done by [8]. In this extensive study, start-up, development length, and perturbations

were studied numerically for a VPL pipe flow. Perturbations of various amplitudes were introduced to a VPL flow and no instabilities were seen to develop at moderate Reynolds numbers $\sim O(100)$. This is evidence that VPL pipe flows are robustly stable in practice.

1.3 Multilayer Viscoplatic Lubrication Flows in Experimentation

The flows studied in this thesis are concentric flows with a power law or visco-elastic core fluid and a Herschel Bulkley lubricating fluid. The core fluid is surrounded by a 'plug' of fluid (unyielded fluid) where the Bingham number ($B = \frac{\tau_y L}{\mu w(r)}$) > 1. As mentioned above, Frigaard introduced this method of stabilizing fluid-fluid interfaces in [2]. In [10], Huen provided the first experimental evidence that these flows can be stable by using xanthan as the core fluid and carbopol as the yield stress lubricating fluid (the same fluids that will be used in this thesis). In [10], a 25 mm radius vertical pipe was filled with carbopol and then carbopol and xanthan were injected into the pipe simultaneously, xanthan in the center of the pipe and carbopol in the outer annulus of the pipe. The experimental results showed that after an initial period of mixing at startup, there was good agreement with the expectation that VPL flows remain stable up to the point where the lubricating fluid is yielded at the interface. Further experimental work was done in [5] where stable flows were observed with carbopol as the lubricating fluid and polyethylene oxide (PEO) and xanthan as the core fluids. In [5], the use of a visco-elastic fluid as the core fluid was experimented with and seen to produce an unexpected 'frozen wavy interface' pattern. In addition, multilayer VPL flows with viscoelastic core fluids were shown to be non-linearly stable in [8].

1.4 Interfacial Patterns in Experimental and Numerical Studies

Experimental and numerical studies have been carried out that suggest relatively large interfacial patterns can exist and even persist at the interface without causing extensive mixing. d'Olce [1] observed naturally occurring instability patterns in concentric pipe flow of two Newtonian fluids up to Reynolds number of 100. Generally, these instability patterns were classified as either 'mushroom' or 'pearl'. The mushroom patterns were observed

to form at low Reynolds number $\sim O(1)$ and lower interfacial radius, compared to the pearl patterns that formed at higher Reynolds numbers$\sim O(10)$ and higher interfacial radius. The patterns did not persist unchanged, rather evolving over time.

In [8], Hormozi found in a numerical study that at small Reynolds number $\sim O(10)$, perturbations introduced will decay in amplitude at a rate that depends on the Reynolds number. When the Reynolds number and amplitude of the perturbations are increased, the structures persist in the interface. This is supported by the non-linear stability analysis in [11]. If a velocity perturbation does not completely decay before the shear stress at the interface drops below the yield stress, the effect of the perturbation will be 'frozen into' the interface at the point where the interface Bingham number increases above 1. Interestingly, in [8],the interfacial stress was lower for higher frequency perturbations after they were frozen in. Experimentally, [7],[10], [5] recorded observations of perturbations that were frozen into the interface and persisted unchanged for lengths of the order of $100 * R_i$. It was suggested in [5] that the phenomena of perturbations being frozen into the interface could be utilized for polymer engineering, manufacturing, and food processing if the shapes can be precisely controlled.

1.5 Applications of VPL

VPL has possible applications in lubricated pipelining, slurry transport, co-extrusion processes in manufacturing and surface coating to name a few. The lubricated pipelining and slurry applications present challenges because of the increased energy required to shear the yield stress fluid compared with using a fluid like water, which can be used here because precise control over the interface is not required, only reduction in the required pressure drop for a given production rate (flow rate). It is possible that applications could exist in the transport of heavy oil products where pumping is too energy intensive. In this case, the oil is usually mixed with water or solvents to dilute it and alter it's rheology. Such an emulsion is expensive to separate and the dilution process often uses harmful chemicals. VPL flow as a lubrication method could allow for a large reduction of the energy required to overcome pipe wall friction if a suitable shear thinning, yield stress lubrication fluid is used. This would also allow pure, undiluted product to be transported.

VPL is promising for several manufacturing techniques. A co-extrusion process is where a product is made by extruding multiple layers of polymer/metal melts from the same die. These processes do require accurate

control over the shape and position of the interfaces by modifying the flow rates and rheologies of each layer. An example of a co-extrusion process in a pipe is the extrusion of tubing used in medical devices which require different properties on the inner and outer diameter of the tube. In this example, layers of different resins are co-extruded to meet the design requirements.

Another application of VPL is the possibly of 'near net shape manufacturing', where perturbations frozen into the interface form the geometry of products in molding processes. If our knowledge of VPL is extended to include the control of the 'freezing in' phenomena noted in [6],[8], this method could accurately define complex internal geometries by replacing either the core or outer fluid with, for example, a polymer melt. Investigating this phenomenon is one of the main objectives of this thesis.

1.6 Problem Description and Outline

VPL flows are studied experimentally in this thesis. The primary research objective is to investigate the possibility of freezing shapes into the interface of VPL flow by introducing perturbations to initially stable flows. The conditions varied include flow rate parameters and fluid parameters. The following three chapters describe the experimental approach to the problem, the results, and a short discussion of the contributions and future directions of this research.

Chapter 2

Materials and Methods

2.1 Physical Description of Apparatus

Figure 2.1 show the main apparatus used to perform all experiments. The flow of interest in the apparatus is through the 50.8 mm inner diameter, 63.5mm outer diameter transparent cast acrylic pipe. The pipe is 2.0 m in length, oriented vertically. At the top of the pipe a flange is fastened to a PVC ring on the bottom outside surface of a catch basin that contains the discharged fluid and transmits it to a drain through a 25.4 mm inner diameter vinyl hose. Hidden from view inside the catch basin is a 305 mm section of the same cast acrylic pipe with a flange on one end fastened to the same acrylic ring through the top surface of the catch basin. Fluid must travel through this extra section of pipe before overflowing into the catch basin so, although it is not part of the flow of interest, this extra section adds hydrostatic pressure to the system. The bottom of the pipe is terminated in a flange which butts to an annular manifold with a 50.8 mm diameter, 110 mm deep blind through-hole aligned with the center line of the main pipe. There are 8 x 6.4 mm ports evenly spaced around the manifold with the center lines of adjacent ports entering the through-hole intersecting at 45 degree angles. These ports are injection ports for the outer fluid and ensure that the outer fluid is injected into the main pipe evenly. At the bottom of the manifold, there is a PVC flange fastened with a threaded neck. The neck threads allow a central injector tube to be installed (Figure 2.2). The injector screws into the bottom of the manifold. Around the main 1524.0 mm long cast acrylic pipe is an "anti-distortion tank". The anti-distortion tank has a square profile in plan view and a rectangular profile in elevation view and is formed from acrylic sheets butted together with beveled edges. The basin, main pipe, anti-distortion tank, manifold, and central injector are supported on an aluminum frame. Four 20 watt fluorescent lights are mounted vertically on the aluminum frame on each corner of the frame between the floor and the roof. Mirrors are arranged to allow viewing of the three hidden sides of the anti-distortion tank. Three sides of the aluminium frame are filled in with sheets of white plastic to reflect light toward the

experimental apparatus. Two tripod mounted Nikon D800 DSLR cameras are positioned in front of the apparatus (Figure 2.3). The rear camera field of view includes the entire 1524 mm length of the apparatus and the smaller field of view of the front camera captures the development region of the flow and is adjusted for each experiment as needed.

2.2 Description of Flow Loop

Figure 2.4 shows a schematic of the flow loop used in all experiments. Each fluid is stored in a separate reservoir prior to pumping. The feed from the reservoir to the apparatus is provided by two pumps. The inner fluid is pumped by a Moyno 500 progressive cavity pump driven by a $\frac{1}{2}$ HP, 3 phase motor (Figure 2.7) which is controlled by a Baldor 240v 0-500 Hz variable frequency drive (VFD) (Figure 2.6). The same pump/motor combination is used for the outer fluid but the motor is controlled by a VF Drive sp500 240v 0-500 Hz VFD. The VFDs chosen can operate the pumps over their rated operating range and can be finely adjusted to a maintain a single motor RPM. Progressive cavity pumps were chosen because they do not alter the rheology of the fluids during pumping. Both fluids travel from the reservoirs through a 25.4 mm vinyl hose to the suction side of the pump. After leaving the pumps, but before entering the apparatus manifold, both fluids flow through separate Omega FPD1204 flow meters. These flow meters output a current from 4 to 20 milliamps depending on the flow rate and can be calibrated to overlap the flow rate operating ranges used in the experiments (see below). After exiting the flow meter an 8 way splitter separates the outer fluid flow with one flow going to each of the 8 injection ports on the manifold. After exiting its flow meter, the inner fluid is piped to a 13.7 mm inner diameter stainless steel tube that passes through the PVC flange at the bottom of the manifold and extends 305 mm up from the bottom of the pipe (pipe/manifold interface). The inner fluid is injected into the experimental pipe at the top of the stainless steel injection tube. The two fluids flow through the main pipe and the 305 mm top section and spill into the catch basin from which they drain via a 25.4 mm vinyl tube.

2.3 PID Control System

Figure 2.8 shows the Labview control interface of the control system based on a proportional/integral/derivative (PID) controller which allows fixed flow rates to be maintained throughout an experiment. A National Instru-

Figure 2.1: Main apparatus used to perform experiments

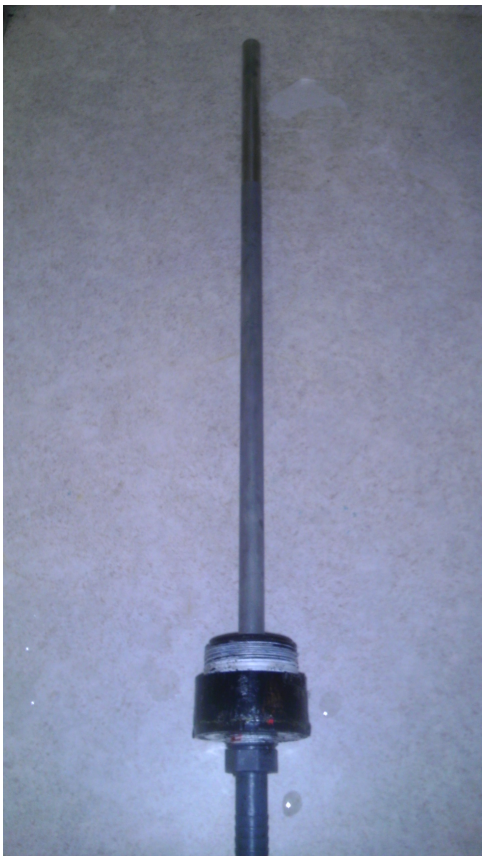

Figure 2.2: Injector used to inject core fluid (internal diameter is 13.7 mm, external diameter is 14.5 mm).

Figure 2.3: Arrangement of tripods (one camera absent for taking this image). See appendix **??** for specification.

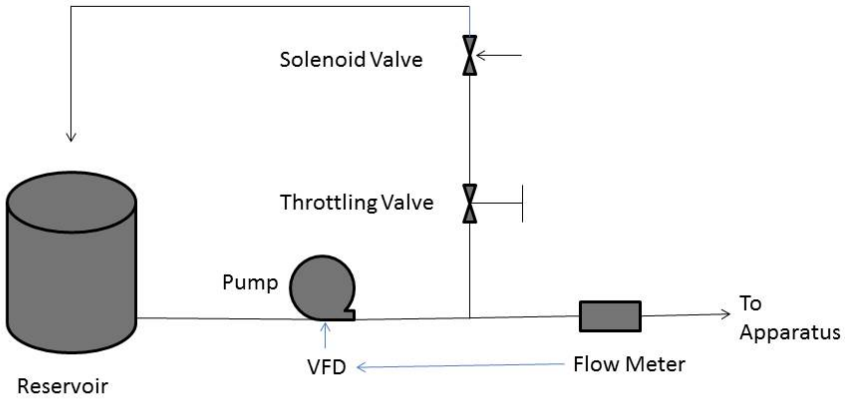

Figure 2.4: Flow loop schematic. The schematic shows the loop used to conduct fluid to the apparatus.

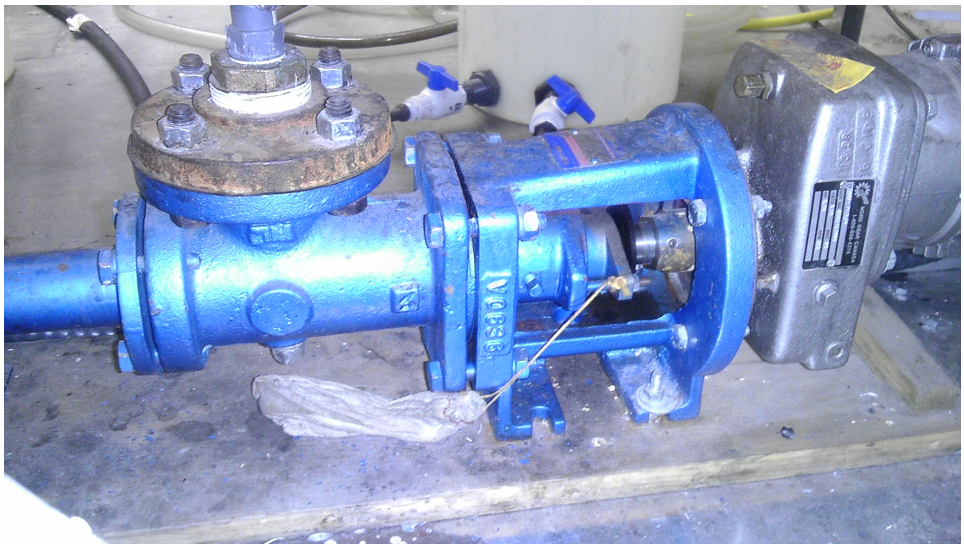

Figure 2.5: Moyno 1000 pump used to pump outer fluid. See appendix **??** for specifications.

Figure 2.6: Variable frequency drives (left SP500 for fluid 1, right Baldor Vector Drive for fluid 2) used to control pump motor speeds. See appendix **??** for specifications.

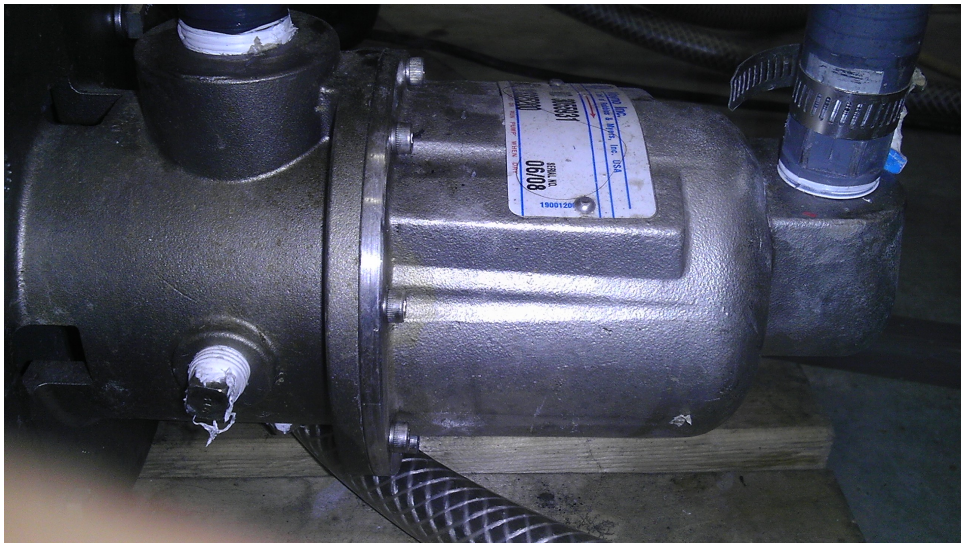

Figure 2.7: Moyno 500 pump used to pump inner fluid. See appendix **??** for specifications.

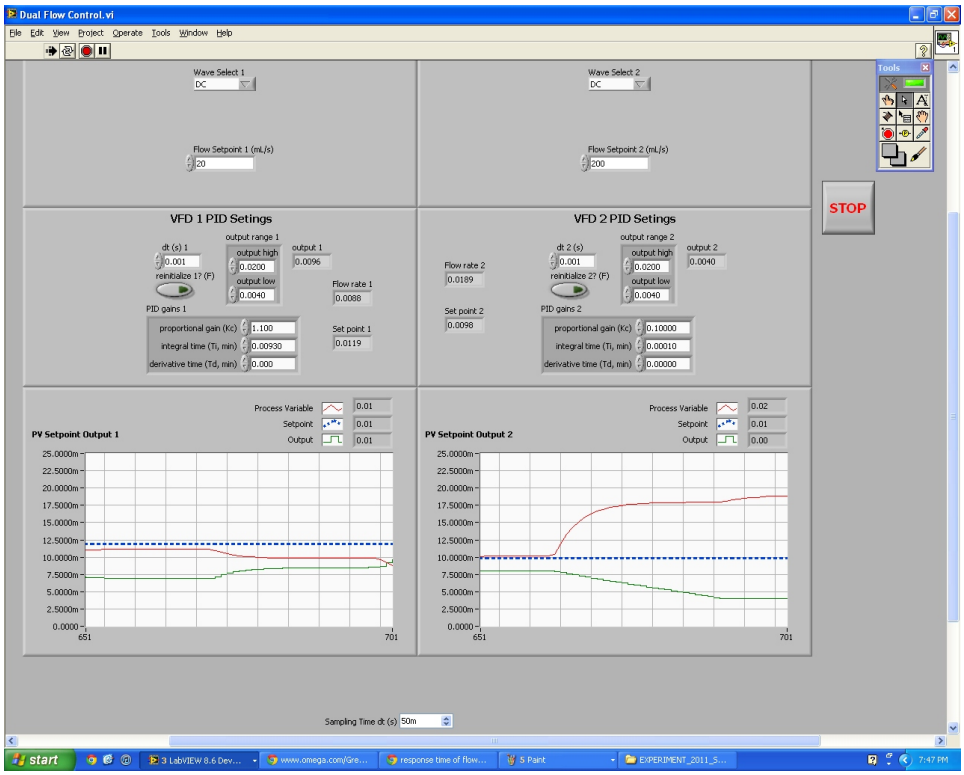

Figure 2.8: Labview PID control interface showing the control options available for the flow loop. The readouts on the two graphs correspond to the flow rates of the two fluids. The output was also saved to an excel spreadsheet that could be looked at during analysis to determine accurate flow rates.

that were created by a solenoid and throttle valve system (described below).

2.4 Solenoid and Throttle Valves

To produce the more rapid changes in flow rate required for some of the experimental treatments, an additional flow control system was incorporated consisting of solenoid and throttle valves. Figure 2.9 and Figure 2.10 show photos of the Solenoid and throttle valve in series and the arduino microprocessor and switching MOSFETs used respectively. An Omega 24V $\frac{1}{2}$ inch solenoid valve and a $\frac{1}{2}$ inch hand operated throttling gate valve were placed in series on a bypass loop at a T junction with each fluid upstream of the flow meters. The bypass loop is opened or closed by the position of the solenoid valve and throttled by the position of the gate valve. Precise flow control was needed later on in the experiments to produce an accurate experimental matrix. This was achieved by having 2 throttling valves in series. The two valves increase the precision by allowing twice the hand operated rotation between completely blocked and completely open. One valve was used to give a rough flow rate slightly higher than the desired flow rate while the second throttling valve was used to trim the flow rate to the desired value. The solenoid valve is controlled by an Arduino microprocessor running a program that controls the timing of its opening and closing. When the solenoid in the bypass loop is switched from closed to open the pressure in the feed loop drops significantly. It was found that this cause a transitory reverse flow in the inner fluid supply to the manifold. To eliminate reverse flows, a brass ball and spring type one way valve (check valve) was added between the flow meter and manifold .

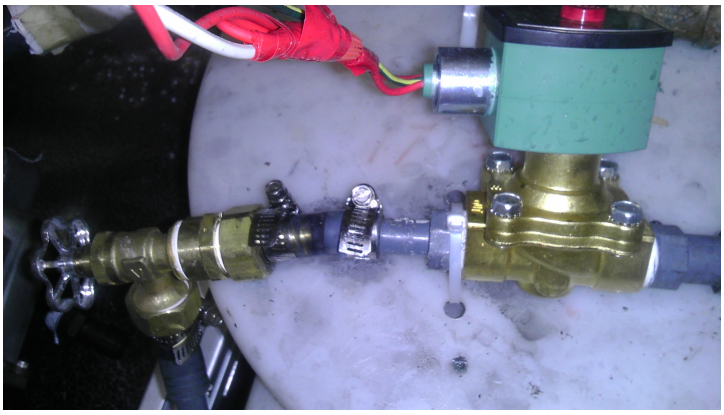

Figure 2.9: Asco 8210 solenoid valve and generic gate valve installed in series and used to introduce rapid changes in flow rate to the system. See appendix **??** for specifications on solenoid valve.

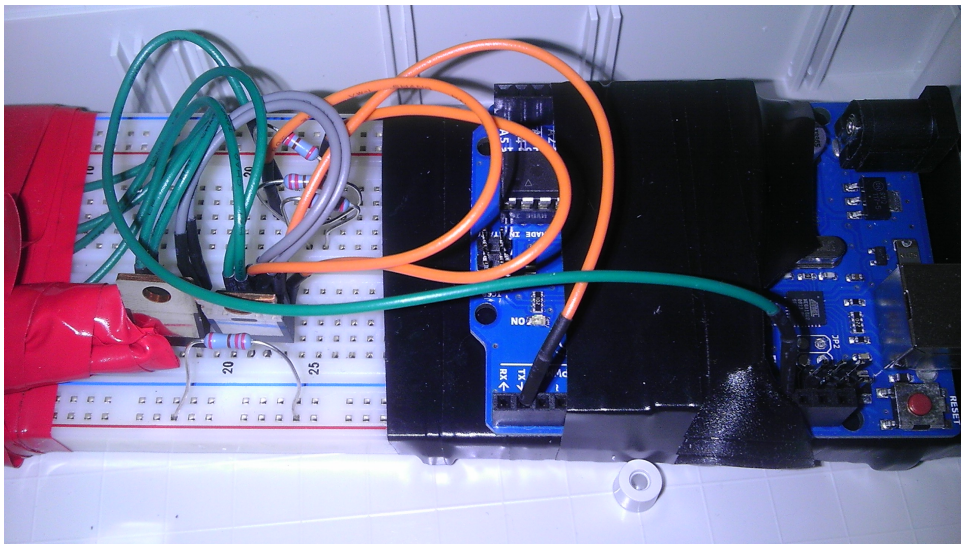

Figure 2.10: Arduino microcontroller and MOSFET transistor switching circuit. See appendix **??** for specifications of the Arduino. This circuit was used to boost the 5 v signal from the microcontroller by switching a transistor and sending 24 v DC to actuate the solenoid valve. Much of the accuracy and reproducibility of the experiments was based on the performance of this switching circuit.

2.5 Anti-distortion Tank

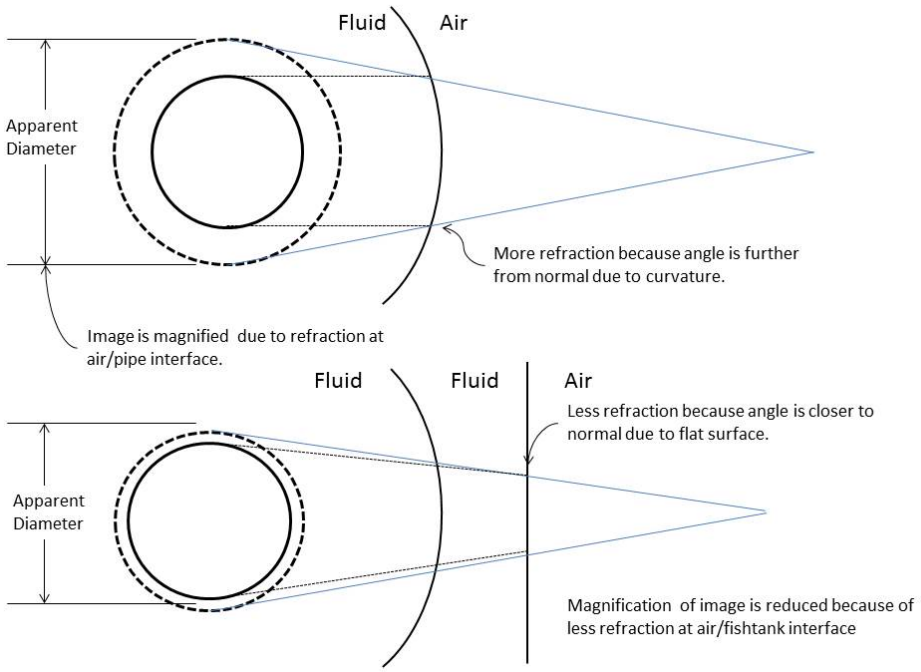

Figure 2.11: Optical abberation caused by a curved surface. The part of the diagram shows the distortion that occurs as a result of the curved pipe surface. The lower part of the diagram shows how this distortion is eliminated by the anti-distortion tank.

The space between the anti-distortion tank and the main pipe is filled with distilled, vacuum treated water. This is done to largely eliminate the optical magnification of the interfacial radius (Figure 2.11) that would be caused by refraction at the interface of the curved pipe and the air. This magnification would be large in the absence of the anti-distortion tank because of the substantial refractive index mismatch between acrylic (RI=1.49) and air, combined with the non-normal angle of incidence of the interfacial image edge with the curved acrylic/air interface. This magnification is much smaller with the anti-distortion tank in place primarily because the angle of incidence of the interfacial image edge with the flat interface of the anti-distortion tank and the air is nearly normal, producing only small refractive

magnification The visual effect of the anti-distortion tank is essentially to allow viewing as if the experiments took place in a tube with a plane face perpendicular to the viewing axis. Although the anti-distortion tank largely eliminates horizontal refractive magnification of the interfacial radius independent of vertical position, magnification could still effect measurements between vertically separated points because the vertical viewing angle becomes less normal as the distance from the pipe to the camera lens increases. To account for this effect a measuring tape was lowered into the center of the experimental pipe and its markings equated to vertically equivalent constant points marked on the outside of the apparatus. The actual vertical position of a point on the interfacial radius could then be obtained by noting its position relative to these points and then converting this position to the corresponding position on the calibration tape. The term 'fish tank' effect is often used in literature to explain this phenomena and the anti distortion tanks are often called fish tanks.

2.6 Fluids

There are three fluids that are used in these experiments:

1. Carbopol EZ2 polymer + NaOH Solution (carbopol)
2. SIgma Xanthan Gum (xanthan)
3. Sigma Polyethlyeneoxide Solution (PEO)

2.6.1 Carbopol EZ2 Polymer Solution

Carbopol was prepared from Carbopol EZ2 Polymer powder and water which was then neutralized with NaOH pellets. A digital scale was used to measure out 40 liters of tap water in a mixing bucket, assuming a water density of 1000 kg/m^3. A predetermined mass of Carbopol EZ2 powder was then measured with a digital analytic balance and added to the water. The concentrations used for all experiments was 0.005 mass fraction of dry Carbopol EZ2 powder to the mass of water. The Carbopol EZ2 + water was mixed for 8 hours with a stainless steel fin type mixing blade rotating at 350 RPM. The mixture was then allowed to stand for 6-8 more hours to de-gas and come to room temperature. At this stage, the mixture has Newtonian rheology, is milky in colour, and has a pH of around 5.0. Increasing the pH to 7.0 through the addition of NaOH allows the polymer to form bonds and develop a yield stress. A digital pH meter was used to measure the pH of the

solution as NaOH was gradually mixed in until the pH reached 7.0. The pH is measured with a hand held digital pH meter. At pH=7 the solution has developed a yield stress and becomes transparent. Mixing is stopped after the neutralized carbopol has a homogeneous consistency. The yield stress does not change very much between pH=7-10 but a pH of 7 was chosen for safety in the event of a spill and to prevent corrosion damage to equipment.

2.6.2 Xanthan Gum

Sigma Xanthan Gum (G1253) powder was used to create the xanthan solutions used in experiments. The xanthan preparation procedure was essentially identical to that of carbopol without the need to adjust pH. The resulting solution is a thick transparent fluid. To produce visual contrast between the xanthan and carbopol, the xanthan was colored by the addition of 30 ml of black fountain pen ink to 40 L of fluid. The concentration of xanthan used in this thesis by mass weight of xanthan to water was 0.005.

2.6.3 PEO

The PEO was mixed in an identical method to xanthan. The resulting solution is a thick fluid that has an apparent high extensional viscosity (when a gloved finger is dipped into the reservoir of PEO, strands of fluid form as the finger is removed). Concentrations of PEO used in this thesis by mass weight of PEO to water are 0.005 and 0.0025.

2.7 Rheometry

2.7.1 Carbopol

Carbopol, the outer fluid or lubricating fluid, is characterized as a yield stress fluid. The yield stress of the lubricating fluid is an important parameter in the experiments because it largely determines the transition between the stable and unstable multilayer flows.

Rheometry of a Yield Stress Fluid

A yield stress is the minimum stress that must be applied to a fluid to create a permanent deformation (ie. flow). In theory, below the yield stress, the fluid acts like a solid and obeys Hooke's law with a stress resulting in a proportional strain, but a zero shear rate. Above the yield stress, the fluid displays a non-zero shear rate. The yield stress is also known as the

Figure 2.12: Bohlin CS-10 rotational rheometer.

proportional limit because it is the limit of stress that will result in a proportional strain. Determining the yield stress of a fluid is difficult because in real fluids, the transition from solid behaviour to fluid behaviour is often gradual rather than abrupt. A common method of measuring yield stress is to perform a 'ramped stress test' and calculate the 'effective viscosity' after each successive increase in shear stress. The "effective viscosity" of a yield stress, Herschel-Bulkley fluid is here defined as the shear stress divided by the "transitory shear rate". "Effective viscosity" is calculated from the transitory rate of deformation (transitory shear rate) in the unyielded fluid shortly after the increase in shear stress, but before the fluid reaches an equilibrium strain. The "effective viscosity" will start low because, as Hooke's law states, the resistance to deformation is proportional to the instantaneous deformation. So the unyielded fluid will strain easily because it is not yet deformed. The "effective viscosity" will be the instantaneous ratio of stress/strain rate. The shear rate here is not truly a shear rate because it is transitory and will decay to zero given enough time since the stress is below the yield stress. If each transitory shear rate is measured shortly after the ramped increase in stress (5 seconds for these tests), it will be non-zero, allowing for the calculation of the effective viscosity. As the ramped stress increases the unyielded fluid strains more but at a decreasing rate, resulting in an increase in the "effective viscosity". The yield stress is taken as the stress corresponding to the highest "effective viscosity" measured using the ramped stress protocol. This is because once the fluid yields, the transitory strain rate will increase and the "effective viscosity" will decrease. The method of highest "effective viscosity" was used to determine the yield stress (used later for the analytical model).

Rheometry Tests Done on Carbopol

The carbopol rheometry tests were performed using a pneumatic Bholan CS10 digital controlled shear stress and strain rate rotational rheometer (Figure 2.12). The tests were done immediately after mixing to prevent thixotropic effects from causing error . The shear is between two parallel serrated plates 40mm in diameter with a gap thickness of 1.00 mm. Carbopol was measured with 40 mm parallel serrated plates because surface serration is required to enforce the 'no slip' condition that is critical in these rheometry measurements. During the tests, carbopol was loaded onto the bottom plate and the top plate is lowered down. The gap is then set to the 1.00 mm standard using a screw adjuster. The excess carbopol is then trimmed away manually. The fluid is pre-sheared for 120 seconds. A linear

Shear Stress Pa	Shear Rate $1/s$	Effective Viscosity Pa.s
2.55E+00	5.68E-04	4.48E+03
7.48E+00	3.65E-03	2.05E+03
1.25E+01	3.91E-03	3.20E+03
1.75E+01	4.16E-03	4.20E+03
2.25E+01	4.43E-03	5.07E+03
2.75E+01	4.77E-03	5.76E+03
3.25E+01	5.15E-03	6.31E+03
3.75E+01	5.55E-03	6.75E+03
4.25E+01	5.97E-03	7.11E+03
4.75E+01	6.36E-03	7.46E+03
5.25E+01	6.82E-03	7.69E+03
5.74E+01	**7.38E-03**	**7.78E+03**
6.25E+01	8.29E-03	7.54E+03
6.75E+01	9.96E-03	6.77E+03
7.26E+01	1.33E-02	5.48E+03
7.75E+01	1.94E-02	4.00E+03
8.25E+01	3.13E-02	2.64E+03
8.76E+01	6.92E-02	1.27E+03
9.25E+01	2.07E-01	4.47E+02
9.75E+01	5.18E-01	1.88E+02
1.02E+02	9.41E-01	1.09E+02
1.07E+02	1.53E+00	7.03E+01
1.12E+02	2.33E+00	4.83E+01
1.17E+02	3.29E+00	3.57E+01
1.22E+02	4.45E+00	2.75E+01
1.27E+02	5.77E+00	2.21E+01

Table 2.1: Rheometry data for 0.5% carbopol.

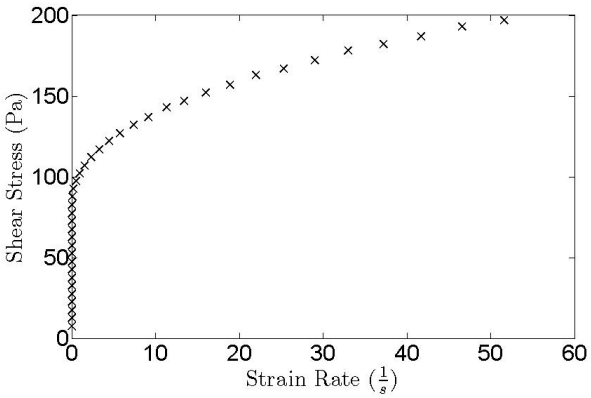

Figure 2.13: Typical stress shear strain rate curve for 0.5% carbopol.

controlled stress ramp test is then performed (see above) which starts below the yield stress and increases to well above the yield stress. The sampling rate and the time between the stress ramp increase and sampling were chosen to eliminate thixotropic effects (5 seconds/sample). Using this method, a stress is introduced for 5 seconds after which the transitory shear rate corresponding to that shear stress (used to calculate effective viscosity) is recorded. Figures 2.13 and 2.14 show the resulting curves from this test. Actual values are given in Table 2.1. The yield stress was determined to be 57.4 Pa (highlighted in bold in Table 2.1). In general, the yield stress of all carbopol batches used in experiments was very consistent in this value, differing by $+/-$ 1 Pa.

Shear stress versus shear rate curves are of primary interest in this thesis because it is the yield stress that determines the transition between stable and unstable flows. The Hershel-Bulkley model was used as a constitutive model for all fluids:

$$\tau_{=}\tau_y + \kappa\dot{\gamma}^n.$$

Fitting the rheological data to the Hershel-Bulkley model was done using Matlab least squares fit. Figure 2.15 shows the carbopol stress strain data from Figure 2.13 fit to the Herschel-Bulkley model. The resulting fit was

$$\tau = 57.4 + 45.0\dot{\gamma}^{0.28}$$

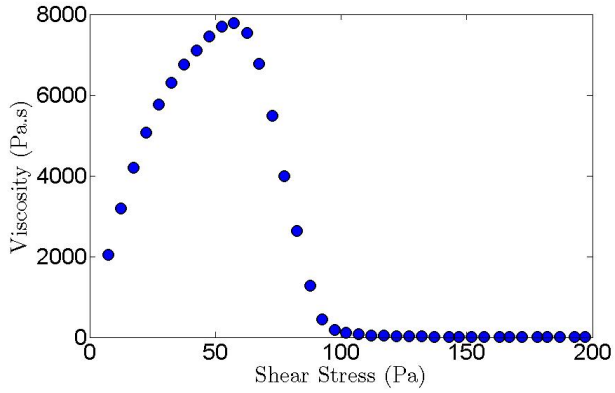

Figure 2.14: Shear Stress vs effective viscosity for 0.5% carbopol. The yield stress is taken as the shear stress that corresponds to the maximum effective viscosity.

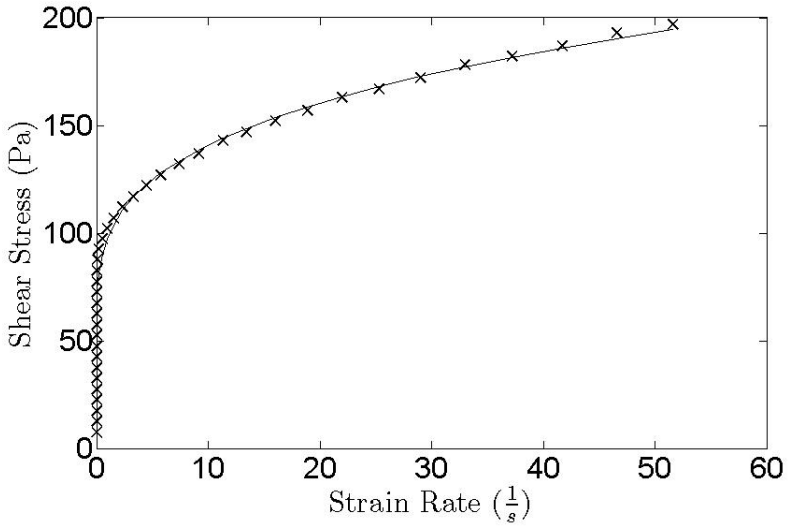

Figure 2.15: Typical stress strain for 0.5% carbopol with the least squares fit shown.

2.7.2 Rheometry Tests Done on Xanthan

Xanthan is used as the inner fluid during experiments. It is a pseudoplastic (shear thinning) fluid that has no yield stress (it flows at any non-zero shear stress) and exhibits long-term thixotrophy in the form of a reduced consistency coefficient if it is allowed to sit for a period of weeks [10]. For this reason, the xanthan was mixed immediately before the experiment so its behaviour would not be affected by thixotropy. The rheometry was performed using the same ramp test described for carbopol to produce stress vs. shear rate data. The one difference in testing xanthan was that a 40mm, 4 degree cone and plate was used to conduct the rheometry tests on xanthan. The cone plate was used because it is a more accurate way of measuring viscosity than parallel plates. This is because the shear rate in independent of radius in the cone and plate method. Xanthan does not require serrated plates because it will shear even on a smooth surface since it has no yield stress.and fit this data to the power law constitutive equation (Herschel-Bulkley model with a zero yield stress). For the 0.5% concentration used, the rheometry data was fit to the constitutive equation by a least squares test. The constitutive model was found to be:

$$\tau = 1.39\dot{\gamma}^{0.39}$$

2.7.3 Rheometry Tests Done on PEO

The rheology of PEO was quantified in a similar fashion to Xanthan. The main difference was that, since PEO is very viscoelastic, the sample was held at a constant shear stress until an equilibrium shear rate was reached. The reading was then taken by the rheometer. The equilibrium shear rate was chosen such that the value of shear rate did not change more than 0.05% in the second before the reading was taken. The readings taken therefore correspond to the rheological behaviour of the fluid in a fully developed steady flow in which the fluid is in a relaxed, equilibrium state. Shown are three plots of data obtained from 0.5% PEO. Figure 2.16 shows shear stress and plotted against the shear rate with the power law fit for 0.4 and 0.5% concentrations. The constitutive equations were found to be:

$$\tau = 1.5\gamma^{0.49}$$

and

$$\tau = 1.37\gamma^{0.50}$$

for 0.5 and 0.4% respectively using the Matlab non linear fit tool.

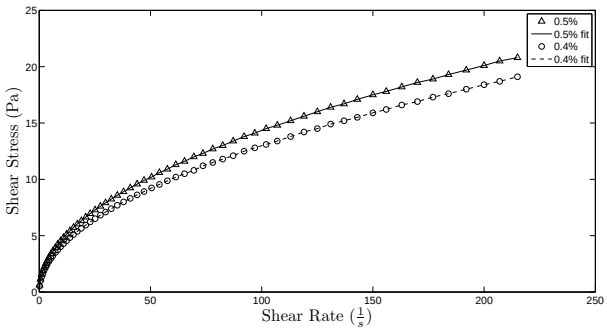

Figure 2.16: 0.4 and 0.5% PEO stress vs strain curve with the power law fit shown.

To quantify the visco-elastic behaviour of PEO, an oscillatory rheometry test was done to obtain plots for the viscous and elastic components of the fluid as a function of frequency. The visco-elastic behaviour of the PEO can be seen in Figure 2.17 c. The viscous modulus (G''), dominates the behaviour of the fluid at low frequencies and the phase angle, θ, of the complex modulus ($G = G' + iG''$) is close to 90 degrees (ie. the maximum stress occurs at the maximum strain rate as would be expected in a Newtonian fluid). In this region, the elastic stresses relax more quickly than the strain is applied. The phase angle of the complex modulus, G, decreases at higher frequencies and G', the elastic modulus, becomes greater than G'' at slightly less than 1 Hz. In this region, the elastic stresses caused by the visco-elastic property of the PEO release slower than the strain is applied and the phase angle drops below 45 degrees, meaning that the peak stress occurs closer to maximum displacement that to the maximum shear rate.

2.7.4 Rheometry Tests Done on Glycerol

Glycerol was tested with the Bohlin CS-10 rheometer using a 4 degree 40 mm cone and plate. Figure 2.18 shows a stress strain curve for the glycerol used in experiments. The Newtonian behaviour of glycerol is confirmed by the linear stress strain profile. The viscosity was found to be 1.21 Pa.s at 25 degrees (temperature of the lab at UBC during glycerol experiments).

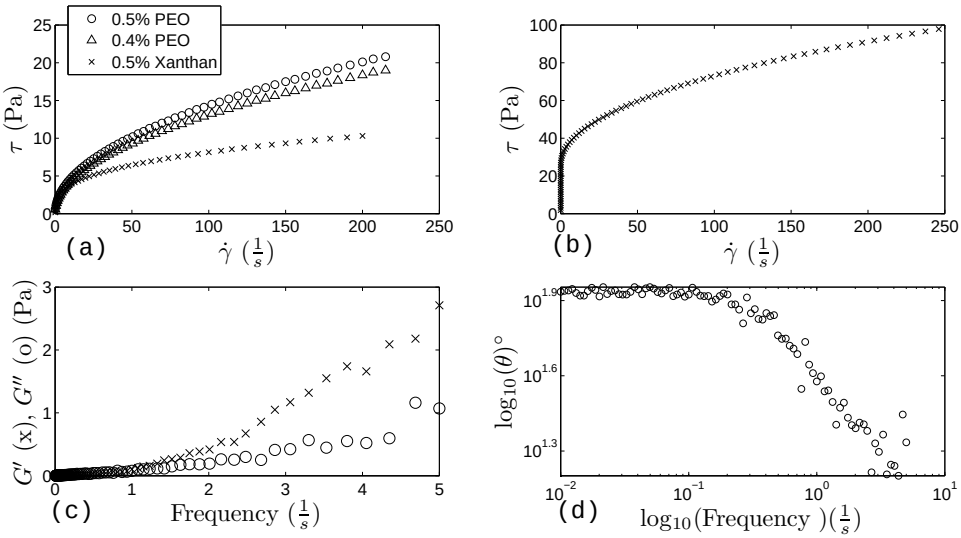

Figure 2.17: A summary of 2 PEO concentrations, carbopol and visco-elastic properties of PEO(a) Shear stress vs shear rate for 0.5% concentration of xanthan and 0.5 and 0.4% concetrations of PEO. (b) Shear stress vs shear rate for 0.5% concentration of carbopol.(c) Loss Modulus G'' and elastic modulus G' for 0.5% PEO. (d) Complex modulus phase angle vs frequency (angle between G' and G'').

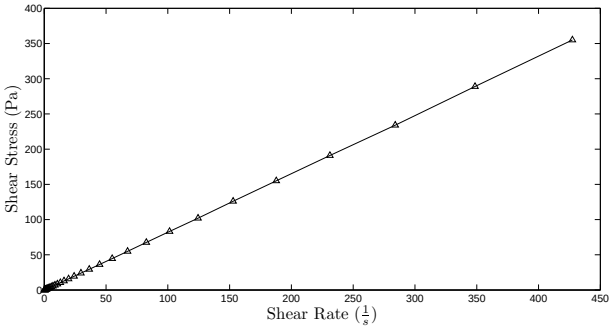

Figure 2.18: Glycerol stress vs shear rate curve with the power law fit shown.

Fluid	τ_y	κ	n
0.5% Carbopol	57.4	45.0	0.28
0.5% Xanthan	0	1.39	0.39
0.5% PEO	0	1.5	0.49
0.4% PEO	0	1.37	0.50
0.25%PEO	0	0.54	0.77
Glycerol	0	1.21	1.0

Table 2.2: Rheometry parameters for fluids used in this thesis.

2.7.5 Further Description of Rheometry Tests and Values Used

To ensure the rheometry curves are relevant for the experiments, a realistic range of experimental shear rate and shear stress was estimated. Selecting this range of shear rates and shear stresses to test was done by using the maximum value of the pressure gradient. This is obtained from the pump specifications and flow curves (figures 2.33,2.34,2.35). Using equation (2.7) (see below), the shear stress can be obtained as a function of radius for a given forward flow pressure gradient. The outer fluid (carbopol) is tested to a minimum shear stress of 150 Pa and the inner fluid is tested to a minimum shear stress of 12 Pa to ensure the experimental range of shear stresses is covered.

2.7.6 Summary of Rheometry Parameters

Table 2.2 shows the Herschel-Bulkley model fit parameters of all the fluids used in this thesis.

2.8 Calibration

2.8.1 Cameras

Two cameras were used to record still images and video of the apparatus during experiments. Measurements of the fluid inside the pipe, including the core fluid radius and position of development fronts and perturbations within the pipe, were extracted from these still images and video. The measurements of interest are all inside the main pipe and the measurement reference points used are outside the pipe. To account for this, a series of high resolution images were taken of a measuring tape inserted into the pipe

Figure 2.19: Omega milliamp output flow meter. See appendix **??** for specifications.

while it was filled with water. The image pixel distance between increments on the tape were then compared to the image pixel distance between permanent lines on the apparatus to produce a scaling factor for converting pixel distance in images to actual distance. The single image sequences taken from videos have a lower resolution than discrete single images (1920 x 1080 vs 5000 x 7000, respectively). Because more precise measurements can be taken from higher resolution images, full size discrete images were used for this purpose whenever possible. However, because of the limited frame rate possible using full size images, video was used to capture high speed phenomenon. The result is lower resolution in spatial measurements when using video because 1 pixel represents a greater proportion of the image field at the lower pixel density.

2.8.2 Flow Rate Measurement

As mentioned previously, two Omega flow meters were used, one for each fluid (Figure 2.8.2). The flow meters output a current between 1.5mA and 25mA depending on the rotation speed of the internal oval gears, which are driven by fluid flowing through the meter. High and low set points can be entered by moving fluid through the meter at a steady rate and pushing high and low set point buttons. The flow meters are advertised as maintaining

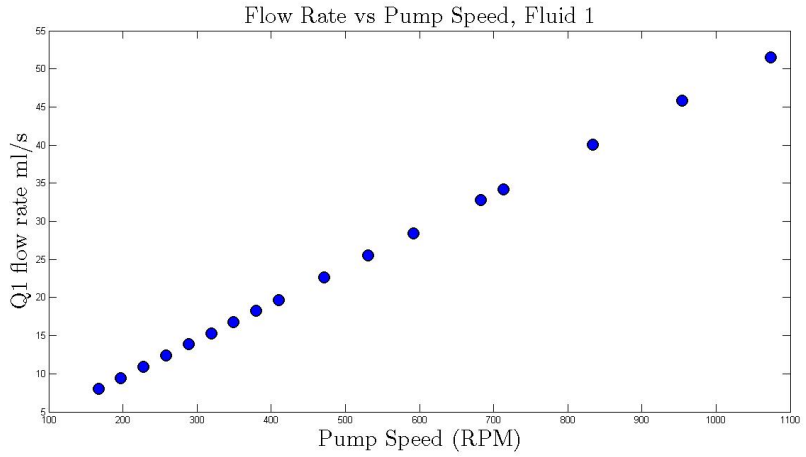

Figure 2.20: Flow Rate vs RPM test data for inner fluid (pump 1).

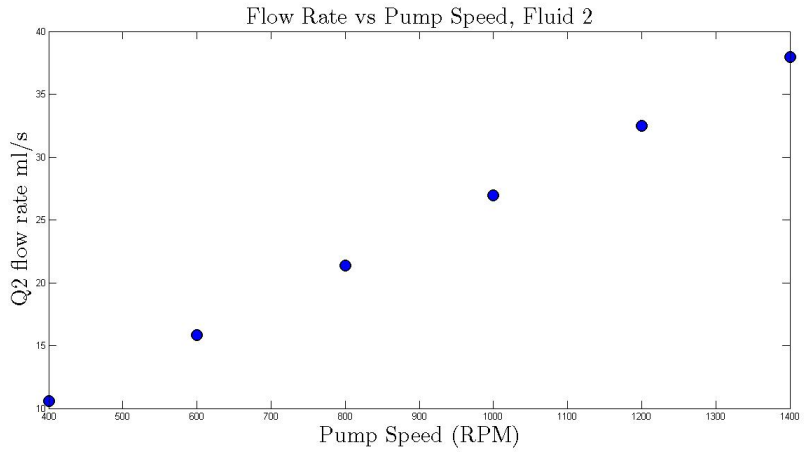

Figure 2.21: Flow Rate vs RPM test data for outer fluid (pump 2).

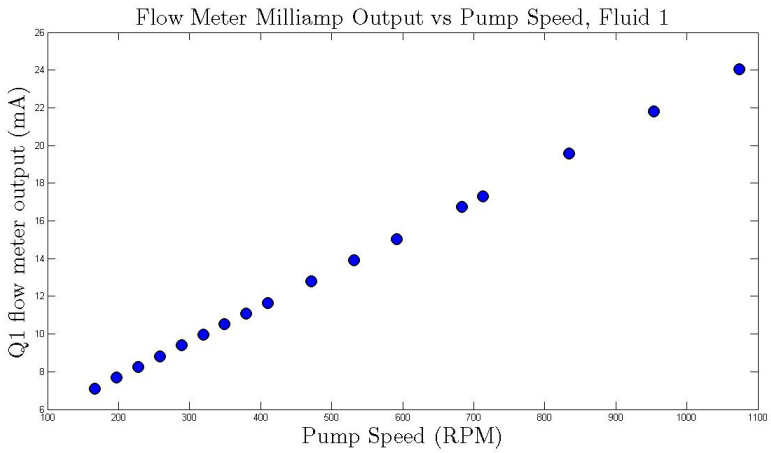

Figure 2.22: Flow meter output (mA)vs RPM test data for inner fluid (pump 1).

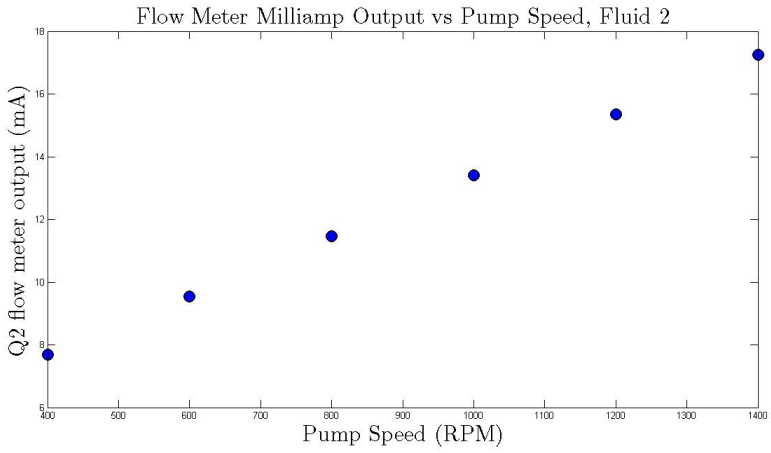

Figure 2.23: Flow meter output (mA)vs RPM test data for outer fluid (pump 2).

good linearity over the range 4-20mA. Because a linear relationship between the mA current output and the flow rate will make analysis of experiments easier, the low set point was chosen to be 4mA for zero flow rate in both flow meters. The upper limit of the flow rates were based on the theoretical flow curves of the system and were chosen such that the system would be stable past the upper set point. To measure flow rate, buckets of the experimental fluids (carbopol and xanthan or PEO) were placed on a digital scale with 0.1 gram resolution. The pumps were turned on and their output adjusted to a constant RPM using the motor controllers to produce constant flow rates somewhat in excess of the maximum used in the experiments. Digital scale readings were then taken 120 seconds apart and the flow meters set to an upper set point of 20 mA at the halfway point (60 seconds) in this interval. The actual flow rates (ml/s) corresponding to a 20 mA flow meter reading were calculated by dividing the change in the volume of liquid (ml) over the 120 second interval by 120. This gave high set point (20 mA) flow rates of 41.2 and 45.3 ml/sec for xanthan and carbopol, respectively. To verify that the flow meter output increased linearly with flow rate, a flow rate vs. motor RPM plot was constructed for each pump and fluid using the mass change over 120 s technique described above. Flow rate was found to be a linear function of RPM (figures 2.20,2.21), as indicated the pump manufacturer. Next the flow meter output was monitored while the pumps were run at constant RPM . This was repeated for a range of RPM values for each pump (figures 2.22, 2.23). The results indicated that the flow rate from the flow rate vs. RPM plots corresponded to the flow rate obtained from the calibrated flow meters because the flow meter output was linear with motor RPM as can be seen in the previous 4 figures. The flow meter calibrations were verified whenever there was an extended period between experiments, using the flow rate vs. pump RPM curves. These curves were also used to preform re-calibrations of the flow meters that were required periodically due to power outages and wear in the oval flow meter gears.

2.9 Data Analysis

2.9.1 Qualitative Stability Observations

Previous experiments using a similar apparatus [10] provided general conditions under which VPL flows may be established with constant flow rates. A small number of initial experiments were carried out to identify the boundary conditions within which VPL flows could be reliably produced in the apparatus. This allowed the subsequent variable flow rate experiments to

be performed well within this stable regime. The classification of experimental outcomes as stable or unstable was qualitative and based on the following criterion:

1. In steady flow experiments, the flow remained stable while being monitored for at least the transit time of the plug. The interface shows no signs of mixing and instabilities introduced in the development region shrink or remain the same size during the entire transit time (no mixing).

2. Unstable steady flow experiments showed signs of mixing within the transit time.

3. In step change experiments, stable flows showed no signs of mixing during the initial establishment of the VPL flow, the introduction of a step change, and one subsequent transit time.

4. Unstable step changes showed signs of mixing after the introduction of a step change. Flows that became unstable before the introduction of the step change were classified as unstable steady flow experiments.

5. Stable Pulse experiments showed no signs of mixing before, during or one transit time after the introduction of a pulse.

6. Unstable Pulse experiments showed signs of mixing after the introduction of a pulse. Figure 2.24 shows one such experiment that met this criteria. Note the growth of the step change and the mixing.

In all variable flow rate experiments, a stable flow was first established and confirmed by visual inspection (see above criterion). Variable flow rate experiments were initiated once the stability of the flow was confirmed and the initial region of stability had fully transited and cleared the experimental apparatus.

2.9.2 Yield Front Speed Analysis

A 'yield front' is a visible deformation of the interface produced during step change experiments and is the results of a transition between two base flows. The 'yield front' advects upwards following a step change in the flow rate of the inner fluid. During step change experiments, the VPL flow was first established. The cameras were turned on approximately 10 seconds before the step change was introduced to provide a background reading of the ambient

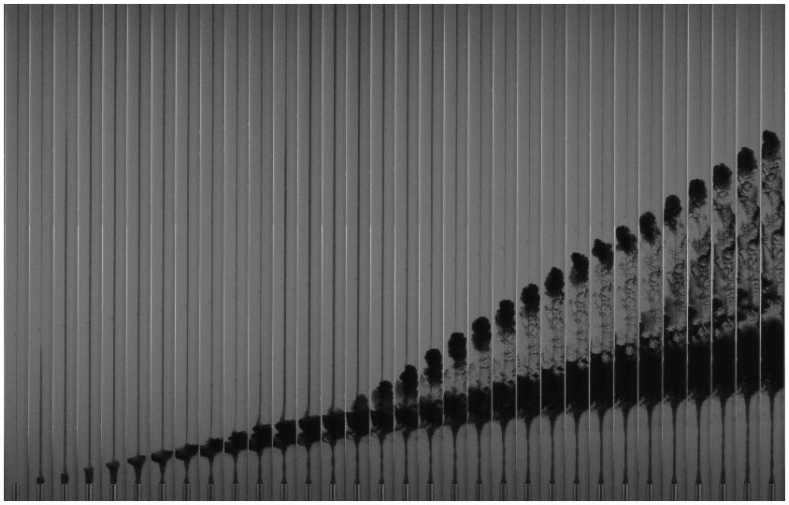

Figure 2.24: Sequence of a VPL flow being perturbed and rapidly progressing to an unstable flow (1 second intervals between images in sequence) $Q_1 = 21$ $\frac{ml}{s}$, $Q_1{}'$, $Q_2 = 9$ $\frac{ml}{s}$,$T = 5$ s.

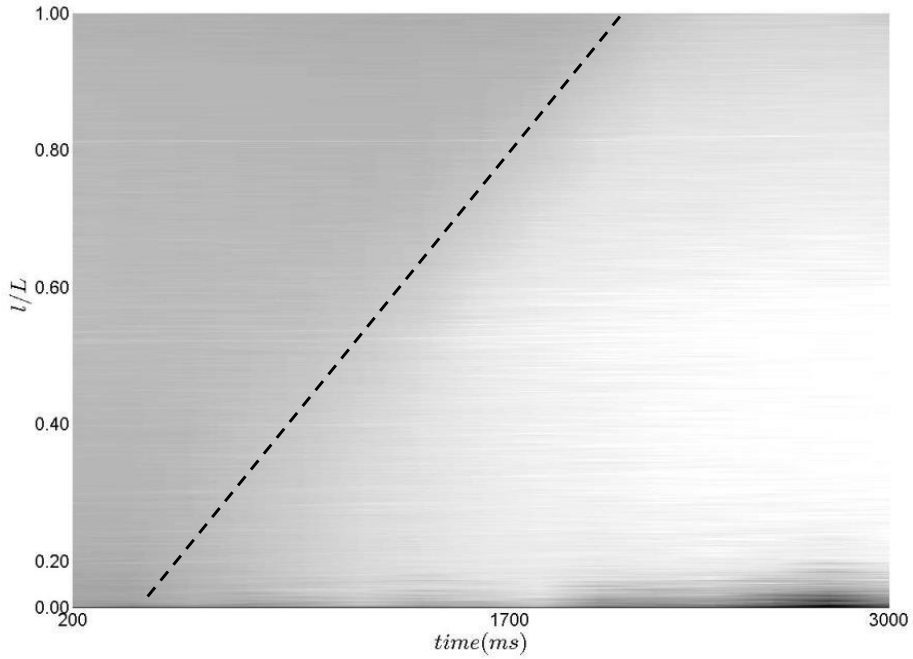

Figure 2.25: Example of a spatiotemporal plot used to estimate the yield front velocity. There is 100 cm of test pipe is shown. $Q_1 = 31\ \frac{ml}{s}$, $Q_1{}' = 15\ \frac{ml}{s}$, $Q_2 = 17\ \frac{ml}{s}$. The slope of the line is used to estimate the velocity of the yield front. Here the velocity is about 0.55 m/s.

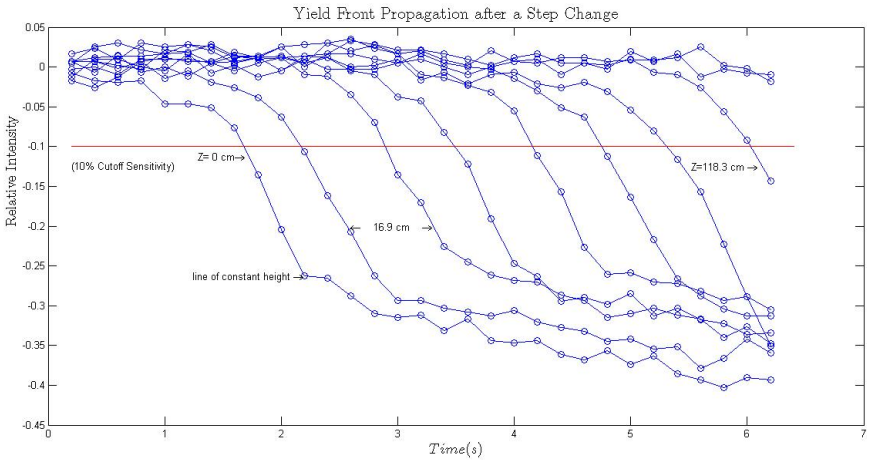

Figure 2.26: Plot used to more accurately determine the yield front velocity. $Q_1 = 31\ \frac{ml}{s}$, $Q_1{}' = 15\ \frac{ml}{s}$, $Q_2 = 17\ \frac{ml}{s}$.

light in the room used for error estimates (see below). The video sequences taken during high/low step change experiments capture the yield front as it advects upwards and are used to estimate its velocity. It is important to get an accurate estimate of the yield front speed under different conditions to see how it is related to the flow rates inside the pipe and determine if the introduction of the step change breaks the unyielded interface (plug interface). For each step change experiment, a spatiotemporal plot was produced (described below). A spatiotemporal plot can be an effective tool for examining yield fronts because changes in the radius of the inner fluid (containing black dye) alter the average pixel intensity in fixed-width areas overlapping the fluid-fluid interface. The subsequent filtering and re-scaling of the pixel data used to prepare the spatiotemporal plot can allow for a more precise identification of the yield front whose velocity can be approximated from the slope of the sharp contrast line between dark and light areas of the plot. These slopes were estimated for all step change experiments by fitting a straight line to the spatiotemporal contrast lines (Figure 2.25).

To get a better estimate of yield front velocity, a method here termed 'intensity propagation analysis' (IPA) was used, and is described below. To start with, consider a single image of a VLP flow. The image is made of an array containing columns and rows of pixels, and each pixel is a 3x1 matrix of RGB values. For IPA, the columns of pixels that include the entire core flow and flow outside, but near the fluid-fluid interface, are located in the pixel matrices of this single image. These columns span the entire image from top to bottom (the length of the test pipe). The result is an n x m (rows x columns) array of RGB pixel values. The m columns were divided into 10 equal groups of n/10 rows. The pixels of the top 10 rows of each group (a subgroup) were then converted to grey scale using the rgb2grey command in Matlab. The resulting subgroups were then averaged using the 'avg' command in Matlab to produce a single greyscale value for that subgroup. The result of this was a vector of 10 greyscale intensity values corresponding to the 10 subgroups. This was repeated for every photo in a sequence to obtain an 10xN matrix, where N is the number of images in a sequence.

At this point in the IPA analysis, as the yield front propagates, the change between high (light) and low (dark) intensity values occurs gradually rather than abruptly. This is analogous to the blurred division between light and dark in the spatiotemporal plots of step changes (Figure 2.25). To better estimate yield front speed the intensity values in the first IPA modified image before the step change were subtracted from each of the corresponding values in each of the subsequent IPA image (subtractive

normalization). A single intensity cut-off value was then chosen that was roughly two times the average standard deviation of the intensity of light in the 10 seconds before the step change was introduced. To obtain this value, the 'stddev' function in matlab was applied to each of the 10 values in each of the 300 IPA modified images from the last 10 seconds before the step change was introduced (30 frames/second * 10 seconds=300 imagesx10 intensities/image=3000 iintesities). The resulting value was multiplied by 2 to get an appropriate cutoff value that would avoid confounding noise with a step change. The cutoff value of 2xsd was determined by inspection. A 'while' loop in Matlab was applied to the 10xN matrix from step change images to find the point in the image sequence where the relative intensity dropped below the threshold at each of the 10 locations. The resulting data is presented in Figure 2.26. Each curve in the figure corresponds to the average intensity falling over time within a single subgroup, with the number of points in each curve being equal to the number of photos and the number of curves being 10.

The residual errors in measuring the front velocity in this way are caused mainly by small fluctuations in flow rate and flickering of the fluorescent illumination as well as the limited resolution of the cameras. These natural fluctuation can be seen in Figure 2.26 as the relative intensity fluctuates slightly before dropping off as the yield front passes. If the light flickering is assumed to be stochastic, then there is a 4.4% chance that a change in relative intensity of twice the standard deviation is a random occurrence. If the error is 1 image frame, the error is large. At 30 measurements per second, the error becomes $\frac{1}{30}$ seconds for each 10 cm section. The highest measured velocities in experimental results are approximately 0.7 m/s. This gives and error of $(1/30)/(0.1/0.7) = 20\%$. If the error is taken to be 4.4% of this (the probability of being out by a single frame), the error is reduced to 1%.

The reported speed of the yield front in the results section is the average transit time between the 10 sequential segments across the cutoff line. The spatiotemporal plots are used to check verify the values reported from the above described algorithm to prevent errors caused by, for example, the turning on of a light, opening of a door, or movement in the lab.

2.9.3 Image Sequences and Spatiotemporal Plots

Much of the data in this thesis is extracted from single image sequences and consecutive video frames. To compress the data presentation and because some phenomena are often not easily identified in conventional imagery,

Figure 2.27: Example of a photo sequence. A high to low step change in the core flow is introduced at time t=0 and can be seen to advect upwards. To report results of an experiment, in the results section, axis are put on a photo sequence to show when during the experiment the image was captured and the dimensions of the photos.

image sequences and spatio-temporal plots are often used to present and analyze these sequences. An image sequence is simply a sequence of images arrange to show the progression of an experiment. A code was written in matlab to extract the area of interest from the raw images and to adjust the colour to make the core fluid more visible. A spatio-temporal plot is a contour plot of image intensity in the time (X) and space (Y) plane. The spatio-temporal plots presented were constructed using data extracted from 10 to 400 sequential photos or video frames. To construct spatio-temporal plots from sequential images, the "area of interest" is first identified. The area of interest generally includes the full vertical dimensions of a frame (all pixel rows) but restricts the horizontal dimensions to the experimental pipe (eliminates pixel columns outside the pipe). The area of interest is identified in the first image in the sequence and the pixel values from this area are read into an array which then contains the red/green/blue (RGB) values for each pixel in the area of interest. This process is repeated for all images in the sequence using the same area of interest (identical pixel rows and columns). This RGB information for each pixel is initially stored as 3 values, each between 1 and 256, which represent the relative intensity of red, green, or blue in the pixel. The three RGB values for each pixel are then converted into

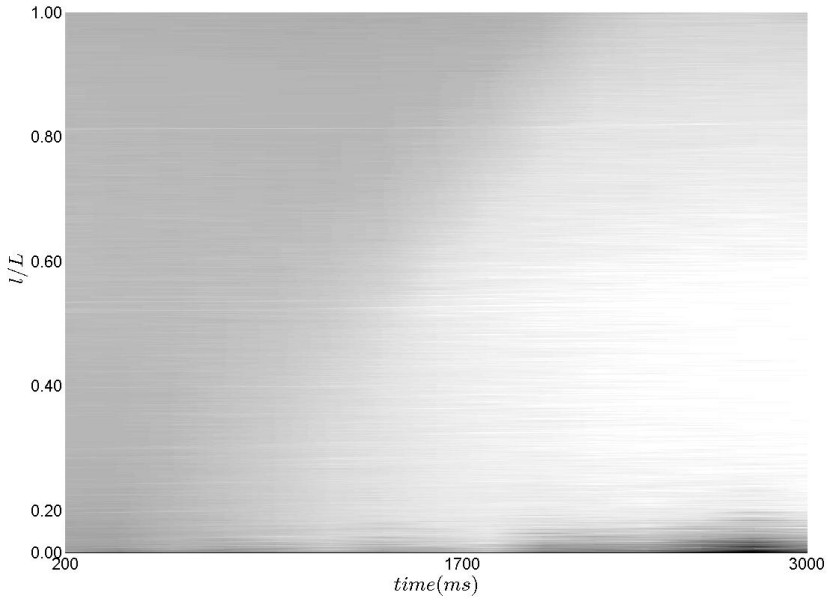

Figure 2.28: Spatiotemporal plot of a image sequence. Spatiotemporal plots are used to illustrate the concentration of dyed (core) vs clear fluid (annular fluid). In the results section, axis are clarified to convey the vertical dimensions.

a single greyscale intensity value using the rgb2bw function in MATLAB. In all the experiments presented here, the inner fluid contains a black ink dye and the outer fluid is transparent, so that this greyscale conversion provides excellent resolution of the flows while at the same time facilitating additional analyses. To produce the spatiotemporal plot, the greyscale data is smoothed by taking a running average of the values for adjacent pixels using smoothing function in matlab called 'medfilt2', to reduce the effect of small random intensity variations. Sequential images of the area of interest are then plotted side by side along the x (time) axis to produce what is essentially a filtered time lapse record of the area of interest. To account for differences in light intensity and interfacial radius between experiments, the grey scale is normalized to make the darkest parts of the image completely black (grey scale = 0) and the lightest parts of the image completely bright (greyscale=1) and with 50 intensity bins in between keep the initial image resolution. This is done after the smoothing process described above. This algorithm allows even small changes in the interfacial radius to be picked up by adjusting the resolution and the threshold values. 'Thresholding' the values essentially normalizes them by using the same darkest and lightest values for all the images in a sequence. Figure 2.27 and Figure 3.6 show an image sequence and a spatiotemporal plot, respectively. In the results section of the thesis, the vertical dimensions of the spatiotemporal plots and image sequences are given in the captions. Not all spatiotemporal plots and image sequences are the same scale due to noise and distortion near the top of the test pipe that caused irregularities and blurring in images which made it difficult to produce clear figures. This noise and distortion had to be eliminated by cropping the images on an experiment by experiment basis.

2.10 Experimental Procedures

A typical experimental run is begun by turning on the two cameras which were set to record either 1080X1920 video at 30 frames/s or time lapse photos at 1 frame/s. The Labview program, used to record flow data, was then activated and the flow loops were powered up to begin the flow of carbopol and xanthan to the experimental pipe. Experimental flow manipulations were not initiated until the two flows reached a stable core annular flow. The same flow loop was used to adjust and vary the flows in both fluids (see Figure 2.29).

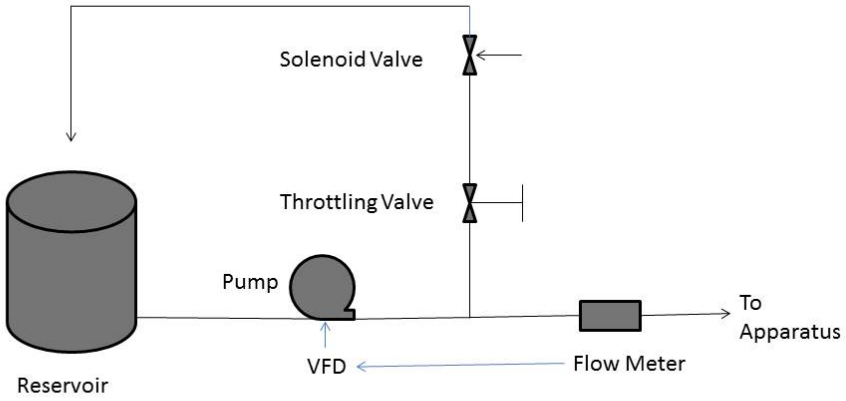

Figure 2.29: Flow loop used to vary and adjust flows in both fluids. See text for details.

Stable Flow Experiments

Constant flow rates were established by closing the solenoid valve and adjusting the VFD to desired flow rate, which was maintained for the duration of the experiment. These lasted, at a minimum, for the time required for a point on the interface to transit this pipe (transit time).

Step Change Experiments

Step change experiments were conducted by establishing a stable flow, then introducing a rapid and permanent change to either the inner flow, the outer flow, or the inner and outer flows simultaneously. The step change was controlled by the VFDs and the throttling and solenoid valves. For example, for a high to low step change, the desired high flow rate was set by first closing the solenoid valve and then adjusting the VFD to give the desired high flow. The low flow was then set by opening the solenoid valve and adjusting the flow by using the throttling valve on the bypass loop. The stable flow was then established by closing the solenoid valve prior to the beginning of an experimental run. The Arduno microcontroller is turned on before the experiment is started and runs a program that keeps the solenoid valve closed for 30 seconds, then opens the solenoid valve until the experimental run is terminated. For low to high step change experiments, this process is reversed.

Pulse Experiments

Pulse experiments were conducted by establishing a stable flow then introducing a pulse change (high/low/high) to the inner core flow. To achieve a 'near net shape' pattern the interfacial radius must be altered. The reason the inner flow was changed is because the interfacial radius is more sensitive to the core flow rate then to the annular flow rate. The pulse change was controlled by the VFDs and the positions of the solenoid and throttling valves. For example, for a high/low/high pulse experiment, the high and low flows were set as for a step change experiment. The initial change from high to low flow also used the procedure described for the step change. However, in the pulse experiments the low flow was only allowed to proceed for a set amount of time between 1 and 6 seconds, after which the solenoid valve was closed to reestablish the high flow. The solenoid valve remained closed for single pulse experiments, but the pulse procedure was repeated for multiple pulse experiments.

2.11 Differential Analysis of Visco-Plastic Lubrication

In order to initially identify VPL flow regimes, a simplified one dimensional model of flow is used [9]. This section will derive the equations used in this model and detail the computations used to predict flow regime and interfacial radius (r_i) based on a inner and outer flow rate (Q_1, Q_2).

2.11.1 Simplified Flow Problem

The starting point for deriving this model will be the continuity equation (2.1) and Navier Stokes equations (equations (2.2),(2.3),(2.4)) in cylindrical coordinates (origin is top center of pipe). The subscripts 1 and 2 (on ∇ and κ) are for the core and annular fluid, respectively. The pressure, P is the modified pressure (i.e. $P = p - \rho g z$).

$$\frac{1}{r}\frac{\partial}{\partial r}(r u_r) + \frac{1}{r}\frac{\partial u_\theta}{\partial \theta} + \frac{\partial w}{\partial z} = 0 \tag{2.1}$$

$$\rho\left(\frac{\partial u}{\partial t} + u\frac{\partial u}{\partial r} + \frac{v}{r}\frac{\partial u}{\partial \theta} - \frac{v^2}{r} + w\frac{\partial u}{\partial z}\right) = \left[\frac{1}{r}\frac{\partial}{\partial r}(r\tau_{k,rr}) + \frac{1}{r}\frac{\partial \tau_{k,r\theta}}{\partial \theta} + \frac{\partial \tau_{k,rz}}{\partial z} - \frac{\tau_{k,\theta\theta}}{r}\right] - \frac{\partial P}{\partial r} \tag{2.2}$$

$$\rho\left(\frac{\partial v}{\partial t} + u\frac{\partial v}{\partial r} + \frac{v}{r}\frac{\partial v}{\partial \theta} + \frac{vu}{r} + w\frac{\partial v}{\partial z}\right) = \left[\frac{1}{r^2}\frac{\partial}{\partial r}(r^2\tau_{k,r\theta}) + \frac{1}{r}\frac{\partial \tau_{k,\theta\theta}}{\partial \theta} + \frac{\partial \tau_{k,\theta z}}{\partial z}\right] - \frac{1}{r}\frac{\partial P}{\partial \theta} \tag{2.3}$$

$$\rho\left(\frac{\partial w}{\partial t} + u\frac{\partial w}{\partial r} + \frac{v}{r}\frac{\partial w}{\partial \theta} + w\frac{\partial w}{\partial z}\right) = \left[\frac{1}{r}\frac{\partial}{\partial r}(r\tau_{k,zr}) + \frac{1}{r}\frac{\partial \tau_{k,z\theta}}{\partial \theta} + \frac{\partial \tau_{k,zz}}{\partial z}\right] - \frac{\partial P}{\partial z} \tag{2.4}$$

In the case of fully developed, iso-density, 1 dimensional flow inside a pipe, there is no convective acceleration and the velocity is assumed to be nonzero only in the Z direction and depend on the distance from the center of the pipe only. So $(u, v, w) = (0, 0, w(r))$. Applying these simplifying assumptions to the continuity and Navier Stokes equations, the continuity equation becomes zero and equations (2.2) and (2.3) become:

$$\frac{\partial P}{\partial r} = 0, \tag{2.5}$$

$$\frac{\partial P}{\partial \theta} = 0, \tag{2.6}$$

and equation (2.4) becomes:

$$0 = \frac{1}{r}\frac{\partial}{\partial r}(r\tau_{k,zr}) - \frac{\partial P}{\partial z}. \tag{2.7}$$

Equation (2.7) can be integrated and solved keeping in mind $\tau_{rz} = 0$ at $r = 0$:

$$\int \left(\frac{\partial}{\partial r}(r\tau_{k,zr})\right) dr = \int \left(r\frac{\partial P}{\partial z}\right) dr$$

$$r\tau_{k,zr} = \int \left(r\frac{\partial P}{\partial z}\right) dr$$

$$\tau_{k,zr} = \frac{1}{r}\left(\frac{r^2}{2}\frac{\partial P}{\partial z} + C\right)$$

$$\tau_{k,zr} = \frac{r}{2}\frac{\partial P}{\partial z} \tag{2.8}$$

Equation (2.8) shows that the shear stress τ_{zr} at any point in the pipe for either fluid is necessarily linear and is proportional to the distance away from the center of the pipe. The pressure gradient is negative when the flow is upwards. This allows calculations of wall shear stress and interfacial shear stress to be performed easily if the pressure gradient is known and gives an idea of the pressure head required to overcome the yield stress of a fluid in a pipe at the wall, however, the parameters that can be easily altered during an experiment are only Q_1, Q_2. A model that takes flow rate as input is therefore needed.

2.12 VPL Flow Regimes

The primary interest in this thesis is to examine VPL flows. This section will use the equations described above to analytically solve the velocity profile and flow rates for VPL flow. **VPL flow** occurs when the plug thickness is non zero and there are three distinct regions: the inner core fluid, the un-yielded region of the lubricating fluid (the plug), and the yielded region

of the lubricating fluid. When the annular fluid is entirely yielded, the flow becomes **yielded flow**. Finally, if the annular fluid is entirely unyielded, a **static layer flow** will result. In the following sections, these three flow regimes are shown to be three cases of the parallel flow solution of the Navier-Stokes equations that governs multilayer hydraulics.

2.12.1 Integrating to Obtain a Velocity Equation

To derive equations for flow rate, the velocity equations must be integrated over both the inner and the outer fluid layer in the pipe. This requires separate solutions for the inner and outer fluids, so that the final velocity solution is piecewise smooth.

Constitutive Equation and Velocity Profile

The Herschel-Bulkley constitutive model is used to model the stress/strain rate of both the core and lubricating fluid

$$\tau_k = \tau_{k,y} + \kappa_k \dot{\gamma}^{n_k},$$

$$\dot{\gamma} = |\frac{\partial w}{\partial r}|.$$

This equation can be substituted into an equation for the velocity gradient. Keeping in mind $\hat{U} = (0, 0, w(z))$, the velocity profile can be written as two integrals. One for the core fluid (2.9) and one for the lubricating fluid (2.10).

$$w(r) = \int_r^{R_i} \frac{dw}{dr} dr = -\int_0^{R_i} \dot{\gamma}(r) dr \qquad R_i \geq r \geq 0 \tag{2.9}$$

$$w(r) = \int_R^{r} \frac{dw}{dr} dr = -\int_R^{r} \dot{\gamma}(r) dr \qquad R \geq r \geq R_y \tag{2.10}$$

Integrating to obtain the Velocity equation of the Core Fluid

Equation (2.9) is integrated by substituting the Herschel Bulkley equation (which is expressed in terms of $\dot{\gamma}$). Note the τ_y is dropped from the Herschel Bulkley equation when solving for core flow because the core fluid used in this thesis has zero yield stress (Xanthan).

$$w(r) = \int_r^{R_i} \left(\frac{\tau}{\kappa_1}\right)^{\frac{1}{n_1}} dr \qquad R_{int} \geq r \geq 0 \tag{2.11}$$

Using the result of equation (2.8), (2.11) can be rewritten as:

$$w(r) = \int_r^{R_i} \frac{1}{\kappa_1} \left[\frac{r}{2} |\frac{\partial P}{\partial z}| \right]^{\frac{1}{n_1}} dr \qquad R_{int} \geq r \geq 0 \tag{2.12}$$

Pressure gradient, κ_1, and n_1 are constants, so (2.12) can be written as:

$$w(r) = \left(\frac{1}{2\kappa_1} |\frac{\partial P}{\partial z}| \right)^{\frac{1}{n_1}} \int_r^{R_i} r^{\frac{1}{n_1}} dr$$

$$w(r) = \left(\frac{1}{2\kappa_1} |\frac{\partial P}{\partial z}| \right)^{\frac{1}{n_1}} \left[\frac{r^{\frac{1}{n_1}+1}}{\frac{1}{n_1}+1} \right]_r^{R_i}$$

$$w(r) = \left(\frac{1}{2\kappa_1} |\frac{\partial P}{\partial z}| \right)^{\frac{1}{n_1}} \left[\frac{(R_i - r)^{\frac{1}{n_1}+1}}{\frac{1}{n_1}+1} \right] \qquad R_i \geq r \geq 0 \tag{2.13}$$

The inner fluid velocity profile has boundaries with the outer fluid and the velocity must be continuous across the interface. The velocity at $r = R_i$ is non zero in a core annular flow if the outer fluid has a non zero flow rate. The 'plug', in this case, will be travelling at w_i. To make the equation accross this equation continuous across the interface, w_i is added to equation (2.13)

$$w(r) = \left(\frac{1}{2\kappa_1} |\frac{\partial P}{\partial z}| \right)^{\frac{1}{n_1}} \left[\frac{(R_i - r)^{\frac{1}{n_1}+1}}{\frac{1}{n_1}+1} \right] + w_i \qquad R_i \geq r \geq 0 \tag{2.14}$$

Integrating to obtain the Velocity equation of the Lubricating Fluid

In an identical method to that of the core fluid (above), the lubricating fluid's velocity equation is integrated:

$$w(r) = \frac{\left(\frac{1}{2\kappa_2} |\frac{\partial P}{\partial z}| \right)^{\frac{1}{n_2}}}{\frac{1}{n_2}+1} \left[(R - R_y)^{\frac{1}{n_2}+1} - (r - R_y)^{\frac{1}{n_2}+1} \right] \tag{2.15}$$

Summary of Velocity Profile

For two Herschel-Bulkley Fluids flowing in a pipe with the inner fluid having a zero yield stress, the velocity function is piecewise smooth:

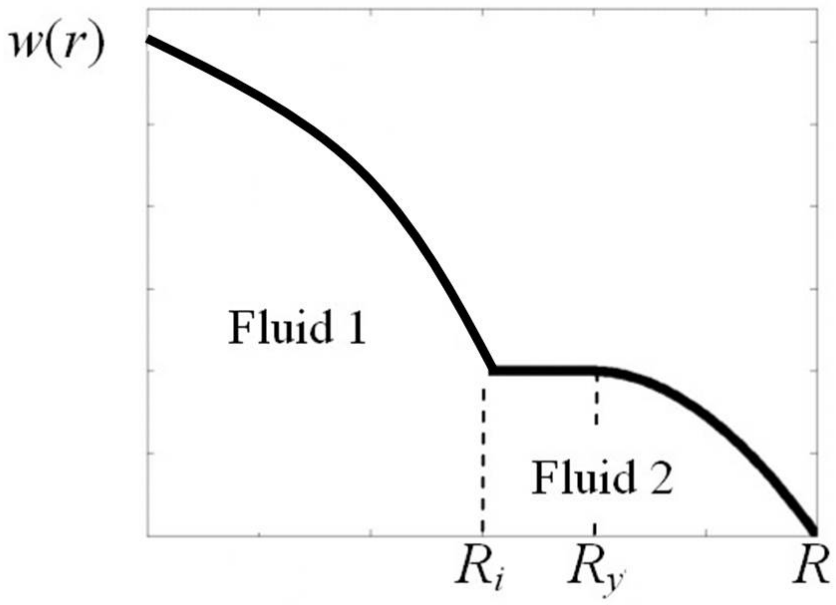

Figure 2.30: Schematic of a **VPL flow** velocity profile.

$$w(r) = \begin{cases} \left(\frac{1}{2\kappa_1}|\frac{\partial P}{\partial z}|\right)^{\frac{1}{n_1}} \left[\frac{(R_i - r)^{\frac{1}{n_1}+1}}{\frac{1}{n_1}+1}\right] + w_i & R_i \geq r \geq 0 \\ w_i & R_y \geq r \geq R_i \\ \frac{\left(\frac{1}{2\kappa_2}|\frac{\partial P}{\partial z}|\right)^{\frac{1}{n_2}}}{\frac{1}{n_2}+1} \left[(R - R_y)^{\frac{1}{n_2}+1} - (r - R_y)^{\frac{1}{n_2}+1}\right] & R \geq r \geq R_y \end{cases} \tag{2.16}$$

It can be seen from inspection that these equations are continuous across both the fluid-fluid interface and the un-yielded-yielded interface. Figure 2.31 shows a schematic of the velocity profile.

Integrating the Velocity Equation to Obtain a Core Flow Rate equation

Integration is over the area of the core fluid. Since the flow is assumed to be one dimensional, the area integral is a single integral over infinitesimal

rings of radius r (2.17)

$$Q_1 = \int_0^{R_i} 2\pi r \left[\left(\frac{1}{2\kappa_1} |\frac{\partial P}{\partial z}| \right)^{\frac{1}{n_1}} \left[\frac{(R_i - r)^{\frac{1}{n_1}+1}}{\frac{1}{n_1}+1} \right] + w_i \right] dr \tag{2.17}$$

$$= 2\pi \left(\left[\frac{\left(\frac{1}{2\kappa_1} |\frac{\partial P}{\partial z}| \right)^{\frac{1}{n_1}}}{\frac{1}{n_1}+1} \right] \int_0^{R_i} (R_i - r)^{\frac{1}{n_1}+1} dr + w_i \int_0^{R_i} r dr \right)$$

Using integration by parts.

$$= 2\pi \left(\left[\frac{\left(\frac{1}{2\kappa_1} |\frac{\partial P}{\partial z}| \right)^{\frac{1}{n_1}}}{\frac{1}{n_1}+1} \right] \left[\left(\frac{r(R_i - r)^{\frac{1}{n_1}+2}}{\frac{1}{n_1}+2} \right)_0^{R_i} - \int_0^{R_i} \frac{(R_i - r)^{\frac{1}{n_1}+2}}{\frac{1}{n_1}+2} dr \right] \right)$$

$$+2\pi \left(+w_i \int_0^{R_i} r dr \right)$$

$$Q_1 = \pi w_i R_i^2 + 2\pi \frac{\left(\frac{1}{2\kappa_1} |\frac{\partial P}{\partial z}| \right)^{\frac{1}{n_1}}}{\frac{1}{n_1}+1} \left[\frac{R_i^{\frac{1}{n_1}+3}}{\left(\frac{1}{n_1}+2 \right) \left(\frac{1}{n_1}+3 \right)} \right] \tag{2.18}$$

Integrating the Velocity Equation to Obtain the Lubricating Fluid Flow Rate

This has to be done over the plug region and yielded region of the lubricating fluid separately because of the discontinuity that exists between the yielded and un-yielded regions. In the yielded region ($R \geq r \geq R_y$), the integral is

$$Q_{2,yielded} = \int_{R_y}^{R} \left(\frac{\left(\frac{1}{2\kappa_2} |\frac{\partial P}{\partial z}| \right)^{\frac{1}{n_1}}}{\frac{1}{n_1}+1} \left[(R - R_y)^{\frac{1}{n_1}+1} - (r - R_y)^{\frac{1}{n_1}+1} \right] \right) dr$$

$$Q_{2,yielded} = 2\pi \frac{\left(\frac{1}{2\kappa_2} |\frac{\partial P}{\partial z}| \right)^{\frac{1}{n_2}}}{\frac{1}{n_2}+1} (R - R_y)^{\frac{1}{n_2}+2} \left(\frac{R - R_y}{\frac{1}{n_2}+3} + \frac{R_y}{\frac{1}{n_2}+2} \right)$$

In the un-yielded region, the velocity will be equal to w_i everywhere

$$Q_{2,unyielded} = \int_{R_i}^{R_y} 2\pi w_i dr$$

$$Q_{2,unyielded} = \pi w_i (R^2 - R_i^2)$$

$$Q_2 = Q_{2,unyielded} + Q_{2,yielded}$$

$$Q_2 = \pi w_i (R^2 - R_i^2) + 2\pi \frac{\left(\frac{1}{2\kappa_2}|\frac{\partial P}{\partial z}|\right)^{\frac{1}{n_2}}}{\frac{1}{n_2}+1}(R-R_y)^{\frac{1}{n_2}+2}\left(\frac{R-R_y}{\frac{1}{n_2}+3} + \frac{R_y}{\frac{1}{n_2}+2}\right) \tag{2.19}$$

where

$$w_i = w(R_y) = \frac{\left(\frac{1}{2\kappa_2}|\frac{\partial P}{\partial z}|\right)^{\frac{1}{n_2}}}{\frac{1}{n_2}+1}(R-R_y)^{\frac{1}{n}+1} \tag{2.20}$$

and

$$R_y = \frac{2\tau_y}{|\frac{\partial P}{\partial z}|} \tag{2.21}$$

The flow rate equations for Q_1, Q_2 are kept separate for both fluids since the flow rates can be controlled individually in the experiments.

2.12.2 Yielded and Static Regimes

Yielded Regime

In a yielded VPL flow, the velocity profile will different from in (2.16) because $R_y < R_i$:

$$w(r) = \begin{cases} \left(\frac{1}{2\kappa_1}|\frac{\partial P}{\partial z}|\right)^{\frac{1}{n_1}} \left[\frac{(R_i - r)^{\frac{1}{n_1}+1}}{\frac{1}{n_1}+1}\right] + w_i & R_i \geq r \geq 0 \\ \frac{\left(\frac{1}{2\kappa_2}|\frac{\partial P}{\partial z}|\right)^{\frac{1}{n_2}}}{\frac{1}{n_2}+1}\left[(R-R_i)^{\frac{1}{n_2}+1} - (r-R_i)^{\frac{1}{n_2}+1}\right] & R \geq r \geq R_i \end{cases} \tag{2.22}$$

where w_i is the same as in (2.20). Figure 3.8 shows a schematic of the yielded velocity profile and a lack of plug region at the interface. The flow rates of the two fluids are:

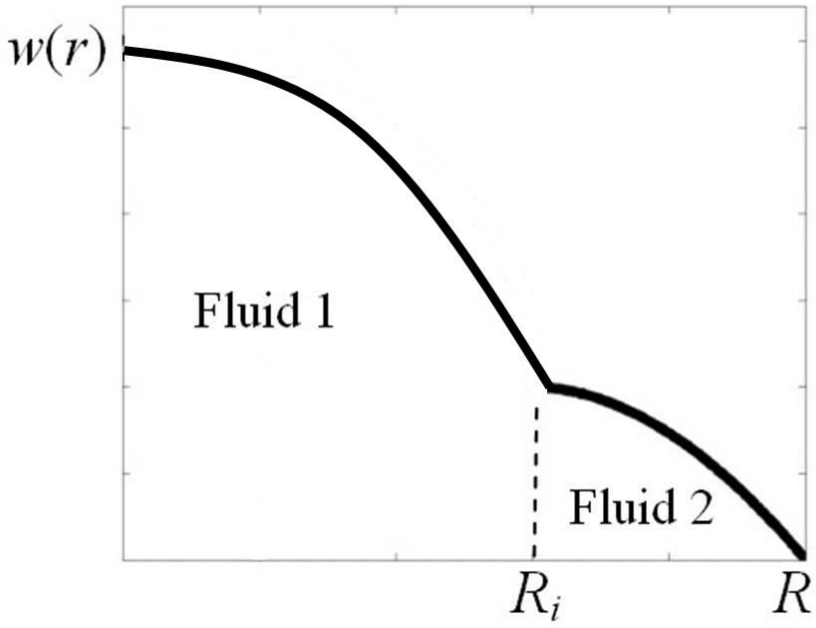

Figure 2.31: Schematic of an **yielded flow** velocity profile.

$$Q_1 = \pi w_i R_i^2 + 2\pi \frac{\left(\frac{1}{2\kappa_1}|\frac{\partial P}{\partial z}|\right)^{\frac{1}{n_1}}}{\frac{1}{n_1}+1}\left[\frac{R_i^{\frac{1}{n_1}+3}}{\left(\frac{1}{n_1}+2\right)\left(\frac{1}{n_1}+3\right)}\right] \tag{2.23}$$

which is the same as in the VPL regime since the core fluid profile is unaffected by the absence of a plug. The flow rate of the outer fluid will be the solved the same way as for the unstable portion in (2.28):

$$Q_{2_{unstable}} = \int_{R_i}^{R}\left(\frac{\left(\frac{1}{2\kappa_2}|\frac{\partial P}{\partial z}|\right)^{\frac{1}{n_1}}}{\frac{1}{n_1}+1}\left[(R-R_i)^{\frac{1}{n_1}+1} - (r-R_i)^{\frac{1}{n_1}+1}\right]\right)dr$$

$$Q_{2_{unstable}} = 2\pi \frac{\left(\frac{1}{2\kappa_2}\frac{\partial P}{\partial z}\right)^{\frac{1}{n_2}}}{\frac{1}{n_2}+1}(R-R_y)^{\frac{1}{n_2}+2}\left(\frac{R-R_y}{\frac{1}{n_2}+3} + \frac{R_y}{\frac{1}{n_2}+2}\right) \tag{2.24}$$

Static Regime

In cases of a low pressure gradient, the shear stress at the pipe wall can be below the yield stress of the lubricating fluid. This case is easily solved and a schematic of the velocity profile is shown in Figure 2.32:

$$w(r) = \begin{cases} \left(\frac{1}{2\kappa_1}|\frac{\partial P}{\partial z}|\right)^{\frac{1}{n_1}}\left[\frac{(R_i-r)^{\frac{1}{n_1}+1}}{\frac{1}{n_1}+1}\right] + w_i & R_i \geq r \geq 0 \\ 0 & R \geq r \geq R_i \end{cases} \tag{2.25}$$

$$Q_1 = \pi w_i R_i^2 + 2\pi \frac{\left(\frac{1}{2\kappa_1}|\frac{\partial P}{\partial z}|\right)^{\frac{1}{n_1}}}{\frac{1}{n_1}+1}\left[\frac{R_i^{\frac{1}{n_1}+3}}{\left(\frac{1}{n_1}+2\right)\left(\frac{1}{n_1}+3\right)}\right] \qquad R_i \geq r \geq 0 \tag{2.26}$$

$$Q_2 = 0$$

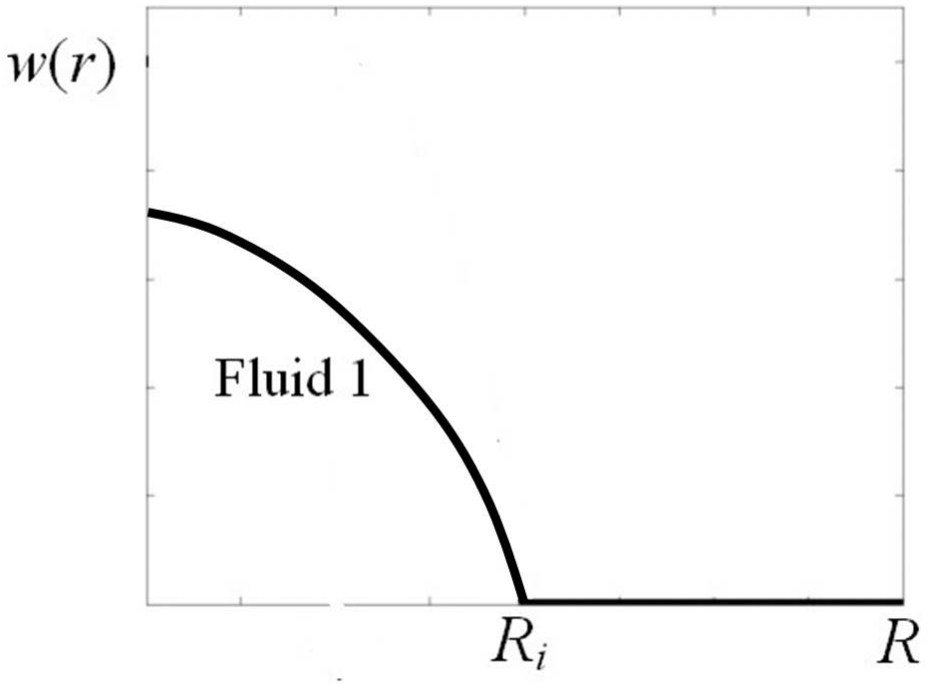

Figure 2.32: Schematic of a **static layer flow** velocity profile.

2.13 Applying the Analytical Model to Experimental Design

The motivation for the analytical solution was to develop a method for designing experimental matrices that would fall into the stable region. The flow rate equation derived above are dependant on κ_k, n_k where $k = 1, 2$. These values are found for the fluids as discussed in the rheometry section of materials and methods. The value R is the inner radius of the pipe (25.4 mm). The structure of the flow rate equations is then:

$$Q_1 = f_1(Ri, |\frac{\partial P}{\partial z}|)$$

$$Q_2 = f_2(Ri, |\frac{\partial P}{\partial z}|)$$

Because Q_1, Q_2 are monotonic functions of the same two parameters, the mapping $(Q_1, Q_2) \rightarrow (R_i, \frac{\partial P}{\partial z})$ is one to one, which means that a pair of flow rates will produce a unique pair of values for the pressure gradient and interfacial radius.

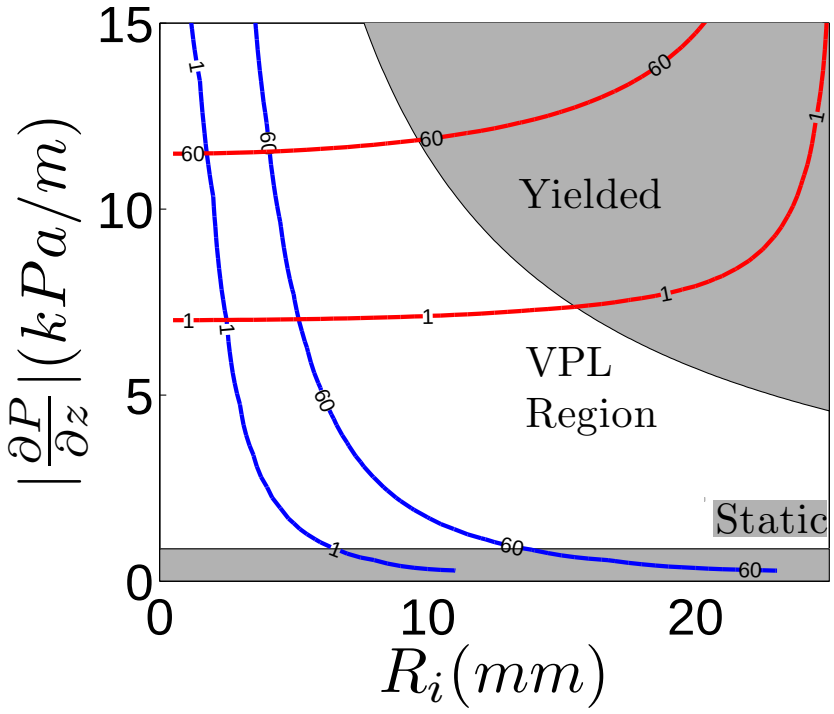

Figure 2.33: Flow rate contours plotted on the R_i,$|\frac{\partial P}{\partial Z}|$ plane for 0.5% xanthan and 0.5% carbopol fit with a Herschel-Bulkley model. The regime of **VPL flow** is shown as the unshaded region between the shaded **yielded** and **static** regions. The red lines are flow rate iso lines (in $\frac{ml}{s}$) for annular fluid (carbopol) and the blue lines are flow rate iso lines of core fluid (xanthan).

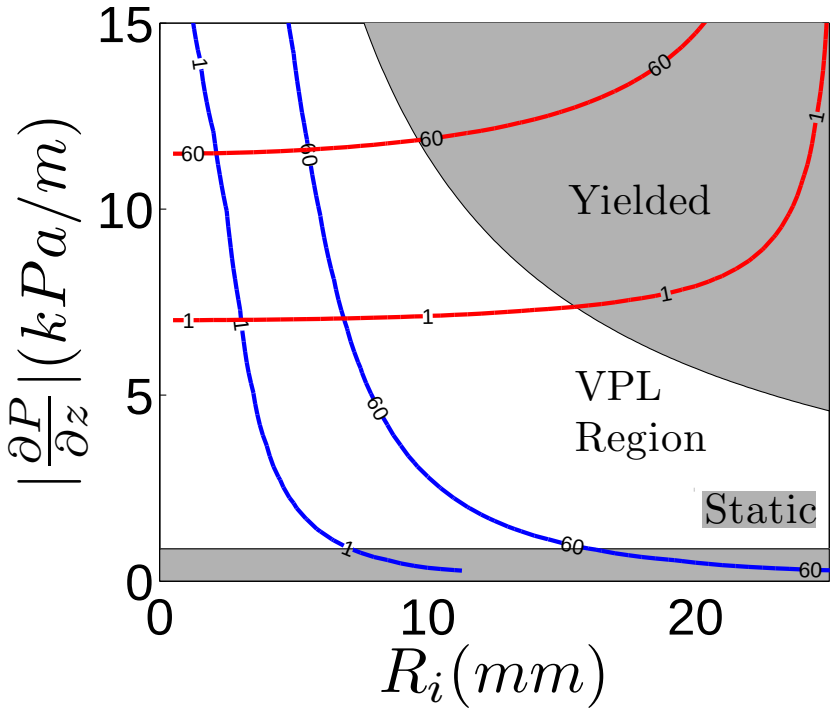

Figure 2.34: Flow rate contours on R_i, $|\frac{\partial P}{\partial z}|$. for 0.5% PEO and 0.5% carbopol fit with a Herschel-Bulkley model. The red lines are flow rate iso lines (in $\frac{ml}{s}$) for annular fluid (carbopol) and the blue lines are flow rate iso lines of core fluid (PEO).

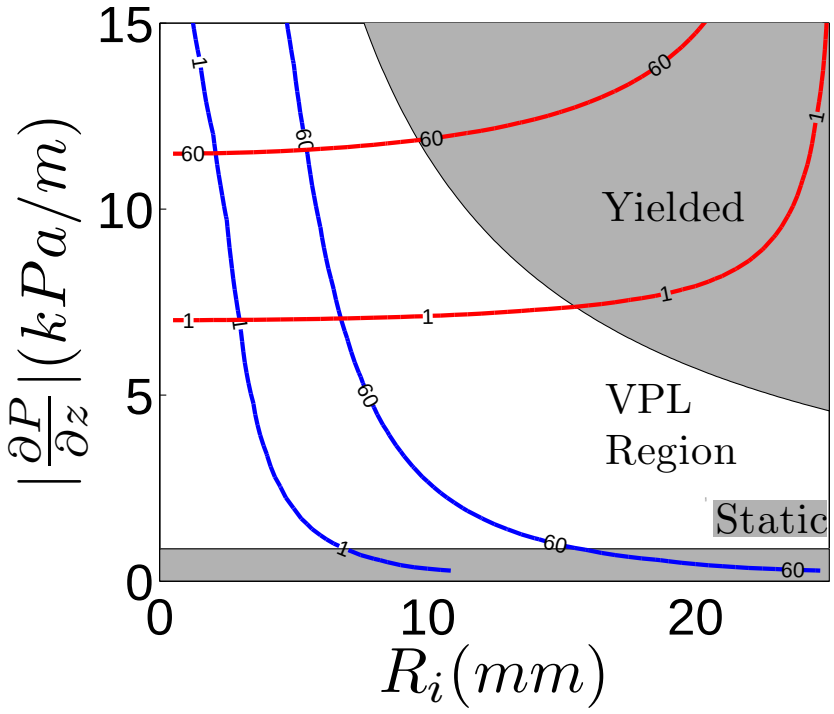

Figure 2.35: Flow rate contours on R_i, $|\frac{\partial P}{\partial z}|$. for 0.4% PEO and 0.5% carbopol fit with a Herschel-Bulkley model. The red lines are flow rate iso lines (in $\frac{ml}{s}$) for annular fluid (carbopol) and the blue lines are flow rate iso lines of core fluid (PEO).

A Matlab code was written to produce an array of values by using the 'meshgrid' function on vectors of pressure gradient and interfacial radius values that were assumed to give flow rates that lie within the operational envelope of the flow loop based on previous studies with similar flow loops (this required some iterations) [9]. The MATLAB program applied the flow rate equations to this array which produced a new array containing the corresponding flow rate. The VPL regime flow equation was used by the code. Contour plots of the resulting array with level lines corresponding to 1 and $60\frac{ml}{s}$ for both Q_1 and Q_2 is shown in figures 2.33 and 2.34 and 2.35. The level lines of Q_2 are distinguished from Q_1 in that they do not enter the static region (Q_2 is zero over this entire region). In the experiments performed in this thesis, a thick plug was needed to to prevent instabilities

during rapid changes. The plug thickness at a given pair of flow rates is the distance between the intersection of the flow rate contours and the boundary between stable and non stable. There is a region enclosed by the 4 flow contours in the graph. It can be seen that if the experimental matrix is contained within the regions $60 \geq Q_1, Q_2 \geq 1$ than the plug thickness will be a minimum of 4 mm.

2.13.1 Inversion of the Flow Equations

To set the limits of the experimental matrix, the flow curves in Figures 2.33,2.34, and 2.35 were used. To generate theoretical predictions of the interfacial radius and pressure gradient based on the controllable inputs to the system (the flow rates), an explicit method is needed. These predictions are generated by inverting the flow problem so that:

$$R_i = g_1(Q_1, Q_2)$$
$$\frac{\partial P}{\partial z} = g_2(Q_1, Q_2)$$

This was done by using the fsolve function in matlab (which finds zeros of functions) on the following equations to solve for interfacial radius and pressure gradient for a given pair of flow rates:

$$0 = \pi w_i R_i^2 + 2\pi \frac{\left(\frac{1}{2\kappa_1}|\frac{\partial P}{\partial z}|\right)^{\frac{1}{n_1}}}{\frac{1}{n_1}+1} \left[\frac{R_i^{\frac{1}{n_1}+3}}{\left(\frac{1}{n_1}+2\right)\left(\frac{1}{n_1}+3\right)}\right] - Q_1 \tag{2.27}$$

$$0 = \pi w_i (R^2 - R_i^2) + 2\pi \frac{\left(\frac{1}{2\kappa_2}|\frac{\partial P}{\partial z}|\right)^{\frac{1}{n_2}}}{\frac{1}{n_2}+1} (R-R_y)^{\frac{1}{n_2}+2} \left(\frac{R-R_y}{\frac{1}{n_2}+3} + \frac{R_y}{\frac{1}{n_2}+2}\right) - Q_2 \tag{2.28}$$

The results of the inversion are used in the results section to compare theoretical and actual values of r_i in chapter 3.

Chapter 3

Results

3.1 Calibration and Benchmarking

3.1.1 Observing the Plug

Estimates of plug thickness are theoretical and are obtained by subtracting the yield radius from the interfacial radius in Figures 2.33,2.34,2.35 in Chapter 2. Experiments were conducted within a range of flow rates that were predicted to have a plug thickness greater than 5 mm. To confirm that the plug thickness is roughly in this range, a flow visualization technique was used. In Figure 3.1, a small amount of dye was added to a pure carbopol flow just upstream of the suction side of the pump. The plug thickness can be approximated by measuring the section of displacement front that remains horizontal. This is measured to be 11.0 mm at the point shown by the white arrow, in Figure 3.1. This approximates the predicted plug thickness.

Figure 3.1: Sequence showing the presence of an unyielded plug. Images are taken 1 second apart, $Q = 20\frac{ml}{s}$. Camera captures 1.2 meters of test pipe. Fluid os 0.5% carbopol. Only the left half of the pipe is shown in each frame for clarity.

3.1.2 Establishing VPL Flows

Preliminary experiments showed that the apparatus was capable of sustaining VPL flows. Figure 3.2 shows a spatiotemporal plot of a startup of 0.5% solutions of carbopol and xanthan. The colour intensity is initially high (white left side of spatiotemporal plot) when Q_1 =0. Dyed xanthan is then pumped into the apparatus and the colour intensity drops (dark black band) near the inlet because of mixing throughout the area of interest. The mixed area is advected leaving a VPL flow (grey in spatiotemporal plot) behind.

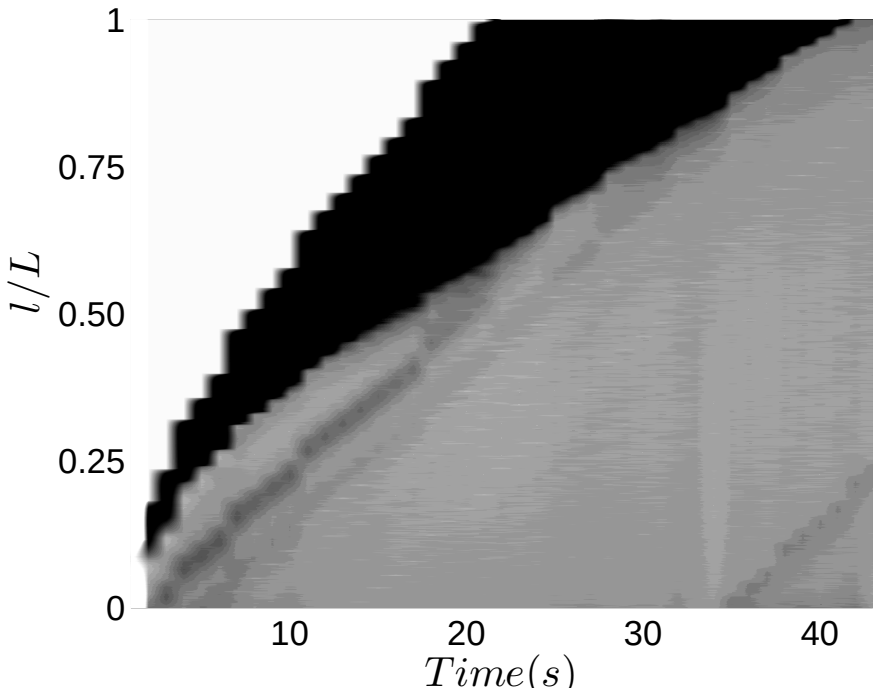

Figure 3.2: Spatiotemporal plot of a startup. The flow rates are Q_1 =48 and Q_2 =14 $\frac{ml}{s}$. 120 cm of test pipe are shown.

3.1.3 Calibration and Comparison with Model

The interfacial radius, r, was measured in 50 experiments and compared with the theoretical value using the rheometry parameters listed above. As in [10], the experimental results match the theoretical predictions closely. Figure 3.3 shows theoretical predictions plotted with measured results. A small error is also introduced in the predicted values since they are based on a fit to the Herschel-Bulkley model.

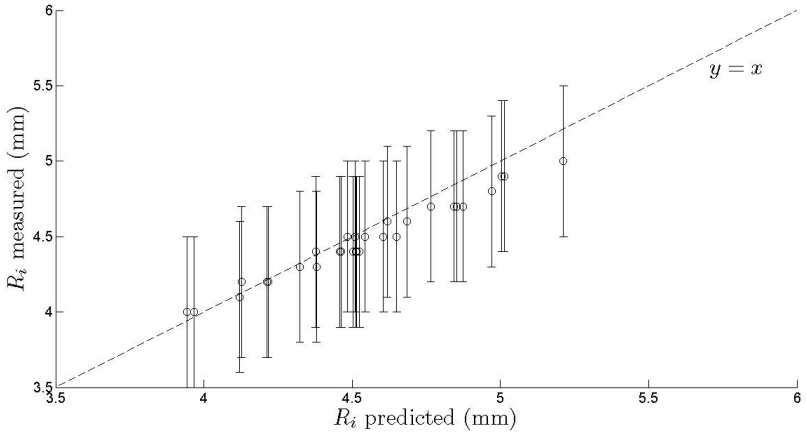

Figure 3.3: Theoretical and experimental values of r_i for 50 experiments. Fluids were 0.5% xanthan, 0.5% carbopol.

3.1.4 Efforts to Use PID Control System to Create Frozen in Effects

It was seen that flow rate could not be accurately controlled with the PD control system. In Figure 3.4, the structures produced are highly irregular and the spacing is un uniform. Based on a number of these experiments, it was determined that the PID control system could not control the flow rate accurately enough to study the interfacial effects during step change, single pulse, or multiple pulse experiments.

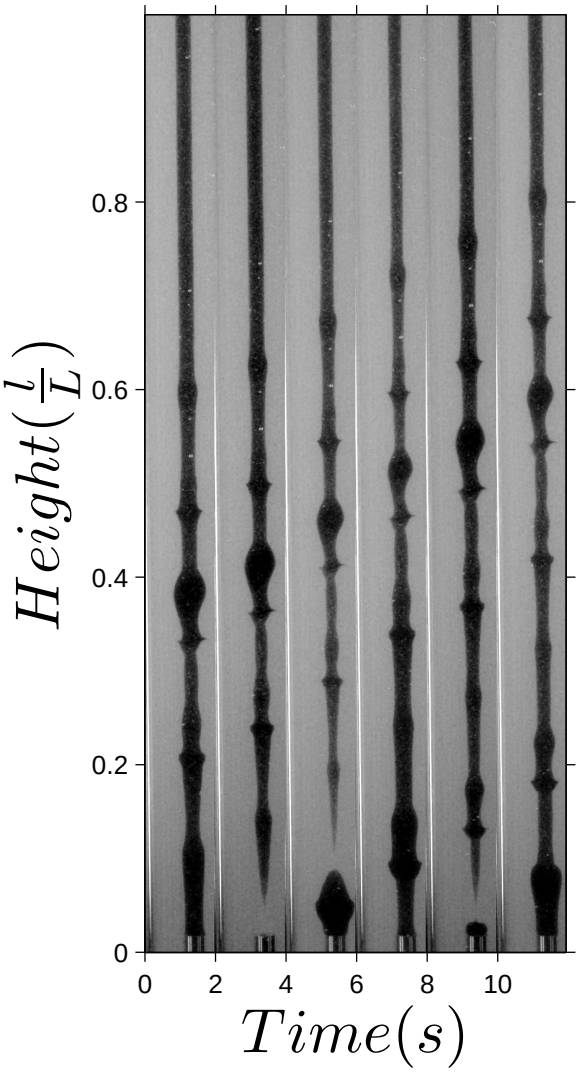

Figure 3.4: Preliminary experiment with 0.5% concentrations of PEO and carbopol. PID was set to make 5 second period square wave pulses at 0.5 relative amplitude to inner fluid. Flow rate is Q_1 =28, Q_2 =14 $\frac{ml}{s}$.

3.2 Scope of Experiments

Experiments (post calibration) consisted of the following:

- Experiments with carbopol and xanthan.
  - Step changes
  - Single pulses
- Experiments with carbopol and PEO (viscoelastic).
  - Multiple pulses.

A complete list of experiments conducted can be found in Appendix a.

3.3 Experiments with Carbopol and Xanthan

3.3.1 Step Changes in the Flow Rate

The main interest in this study is in determining to what extent shapes within the unyielded ring of fluid that surrounds the interface in core-annular flows can be generated and preserved. As the inner fluid flow rate changes ($Q_1 \rightarrow Q_1'$), there is a consequent change in the steady fully established core annular base flow interfacial radius. Assuming the VPL flow remains stable following the step change, the main question is how does the change from one steady flow to the other proceed? One notion might be that the new radius is established close to the inner fluid inlet, freezing into the interface (held by the yield stress), and propagates the length of the pipe at the velocity of the plug.

An example of one step change experiment is shown in Figure 3.5 (a). The core-annular flow is initially fully established with inner flow rate $Q_1 =$ 27.5 ml/s. It is seen that, following the reduction ($Q_1 \rightarrow Q_1'$), the radius of the inner fluid contracts and the contracted radius propagates along the length of the pipe, but not at the velocity of the interface. Figure 3.5(b) presents a spatiotemporal plot of the same experiment. The plot is constructed by averaging the image intensity across the pipe at each fixed height. The images are taken from a high definition video at 30 frames/second. The dark/light indicates the propagating change in radius of the interface. The transition in radius becomes approximately linear, i.e. moving at constant speed, and completes the the transit of the pipe in about 5 s.

Similar results were obtained from all our experiments. The propagation speed observed was significantly faster than the speed of the interface (or

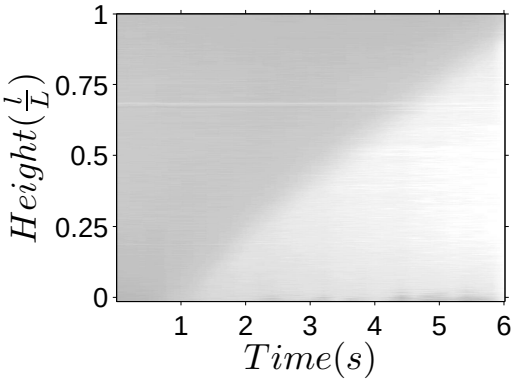

(a)

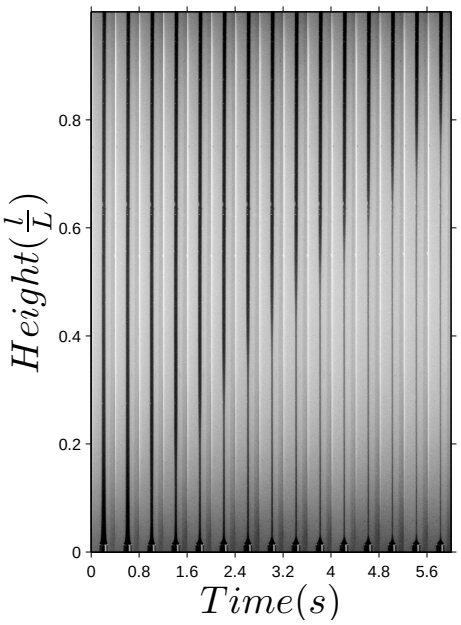

(b)

Figure 3.5: Example of a step change experiment using 0.5% carbopol and 0.5% xanthan. Flow rates: ($Q_1 \rightarrow Q_1'$): $Q_1 = 27.5$ ml/s, $Q_1' = 5.5$ ml/s, $Q_2 = 30.3$ ml/s. (a) A spatiotemporal plot of a 150 cm section of the test pipe shows the transition in interfacial radius after the step change in flow rate. This plot is constructed by averaging the image intensity across the pipe at each fixed height, with images taken from a high definition video at 30 frames/second. (b) Sequential images are shown at $\frac{1}{5}$ s intervals a 90 cm section of the test pipe.

equivalently unyielded plug) in the base flow, (as calculated either before or after the step change), e.g. up to 100 times faster in some cases. This dispels the notion that the step change can be frozen in by the yield surface. Indeed, we effectively observe a "yield front" that propagates the length of the pipe as we transition from one radius to the other.

In order to analyse this situation, we construct a control volume that follows the contour of the interface through the contraction and which propagates at the speed w_{Yf} of the yield front, assumed steady; see Fig. 3.6. With the notation of Fig. 3.6, mass conservation implies that:

$$A_{in}[\bar{w}_{in} - w_{Yf}] = A_{out}[\bar{w}_{out} - w_{Yf}]. \tag{3.1}$$

For the axial momentum balance, we subtract of the static pressure terms (as the fluid densities are the same), assume that the momentum correction factors β are identical at inflow and outflow, and find:

$$A_i\bar{\tau}_{i,z} + \tilde{p}_{out}A_{out} - \tilde{p}_{in}A_{in} = \beta\rho\left(A_{out}[\bar{w}_{out} - w_{Yf}]^2 - A_{in}[\bar{w}_{in} - w_{Yf}]^2\right), \tag{3.2}$$

where $\bar{\tau}_{i,z}$ is the z-component of the mean interfacial traction and $\tilde{p}$ is teh modified pressure. On eliminating $\bar{w}_{out}$ and re-arranging, we find:

$$\left|1 - \frac{w_{Yf}}{\bar{w}_{in}}\right| = \sqrt{\frac{|A_i\bar{\tau}_{i,z} + \tilde{p}_{out}A_{out} - \tilde{p}_{in}\bar{w}_{in}^2A_{in}|}{\beta\rho A_{in}(1 - A_{in}/A_{out})}}. \tag{3.3}$$

Typically, for the flows we have considered in our experiments the inertial stresses associated with $\bar{w}_{in}$ are significantly larger than the interfacial stresses. This is also evidenced by the fact that the flow rate change apparently yields the interface. Assuming that the modified pressure also scales with the viscous stresses, equation 3.3 suggests that the front speed $w_{Yf} \approx \bar{w}_{in}$, with a small correction associated with the interfacial stresses and modified pressure terms.

The mean velocity $\bar{w}_{in}$ is calculated from the flow rate after the step response, $Q_1' = \pi R_{in}^2\bar{w}_{in}$. Figure 3.7 plots $\bar{w}_{in}$ against w_{Yf} for each of our step change experiments. This is calculated from the spatiotemporal plot for each experiments. We can see a relatively close comparison.

The conclusion from this set of preliminary experiments is that any change in flow rate that is long with respect to the convective timescale of the flow is not likely to freeze in to the interface. The core-annular solution of §2.11.1 has a single solution, determined by the flow rates of inner and outer fluids. If a flow rate change is of sufficiently long duration, the flow will transition to the new steady core-annular solution and does so on a

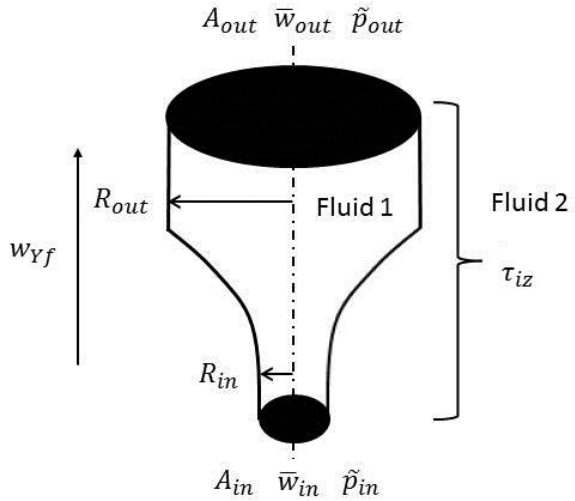

Figure 3.6: Control volume moving axially at speed w_{Yf}.

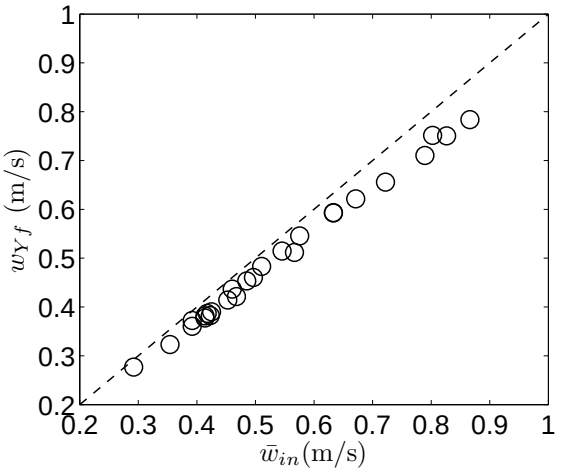

Figure 3.7: Plot of $\bar{w}_{in}$ against w_{Yf} for each of our step change experiments. Error is $\pm$ 0.1 m/s for w_{YF} and $\pm$ 0.15 m/s for $\bar{w}_{in}$ based on image capture and analysis error and flow rate measurement error.

timescale associated with advection along the pipe of the inner fluid. Early experiments with changing Q_2 showed that this produced very little change in the interfacial radius, and no frozen in effects could be produced using even large changes. This is consistent with the $1-D$ model, which predicts that the interfacial radius will change dramatically with changes in Q_1, but very little with changes in Q_2. Step changes with $Q_1 < Q_1'$ were done in early preliminary experiments and it was observed that that this type of change was highly unstable and generally produced mixing if Q_1 was larger than approximately one half the maximum flow rate the flow loop was capable of.

3.3.2 Freezing in of Pulses

Now consider whether a temporary change in core flow rate may freeze in a perturbation in the interface. For a single pulse experiment a step change is imposed to the inner fluid flow rate from Q_1 to Q_1', which is held constant for a duration T before returning to Q_1. The results of single pulse experiments fall into one of three categories:

1. Although the pulse disrupted the interface locally, there was no lasting structure that remained frozen into the interface. Over time the interface returned to its initial parallel configuration. An example of this is shown in Figure 3.8 (a).

2. The flow became unstable and mixing was observed. These results are qualitatively similar to those that have been observed in the start-up phase of establishing core-annular flows of this type, e.g. as in [**?**]. An example is shown in Figure 3.8 (b).

3. The pulse resulted in a deformation of the interface that remained a constant shape, frozen into the interface and moving upwards at the speed of the interface; see e.g. in Figure 3.9.

In the case of a stable structure, the constant speed of the frozen pulse was readily discernible from a spatiotemporal plot of the experiment, e.g. Figure 3.9 (b) shows an example from the experiment of Figure 3.9(a). Figure 3.10 shows a comparison of the speed of the frozen-in interfacial structures, taken from the spatiotemporal plots for ≈ 80 structures, compared with the predicted interfacial speeds w_i.

The occurrence of the above 3 flow regimes is now presented for different pulse amplitudes, durations and outer fluid flow rates. Figure 3.11 presents the data for four pulse durations, T' (1,2,4, and 6 seconds) with Q_2 plotted

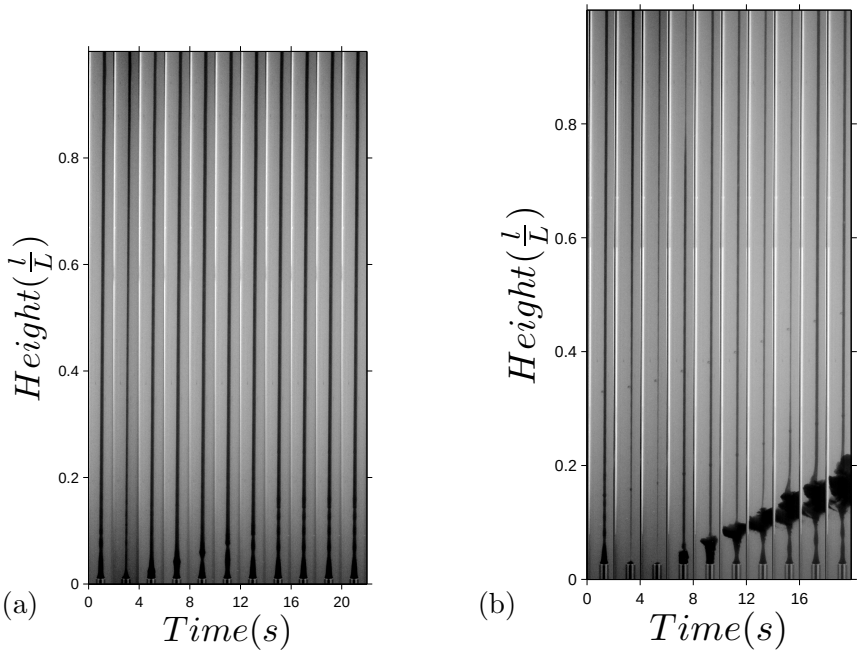

Figure 3.8: (a) No frozen structure: $Q_1 = 21.9$ ml/s, $Q_1' = 7.7$ ml/s, $Q_2 = 20.1$ ml/s, $T' = 1$ s. Photos show 90 cm of the test pipe. Images are 2 seconds apart. (b) An example of a single pulse experiment that resulted in flow instability: $Q_1 = 20.6$ ml/s, $Q_1' = 2.6$ ml/s, $Q_2 = 8.6$ ml/s, $T = 3$ s. Photos show 100 cm of test pipe and images are 2 second apart.

(a)

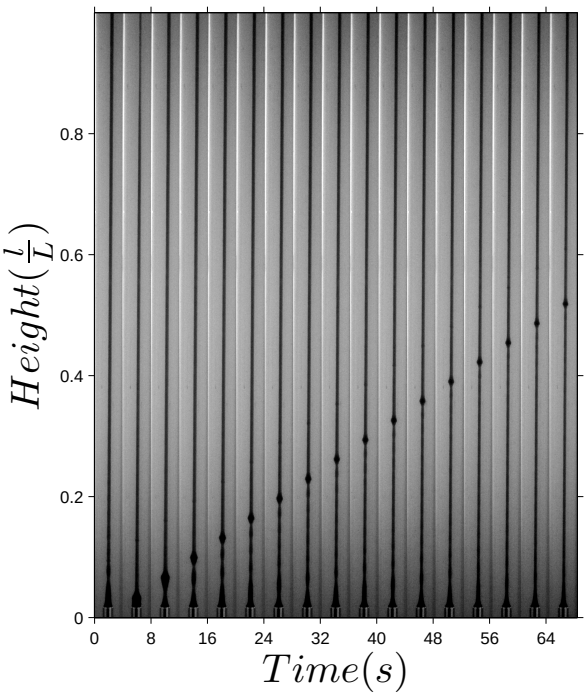

(b)

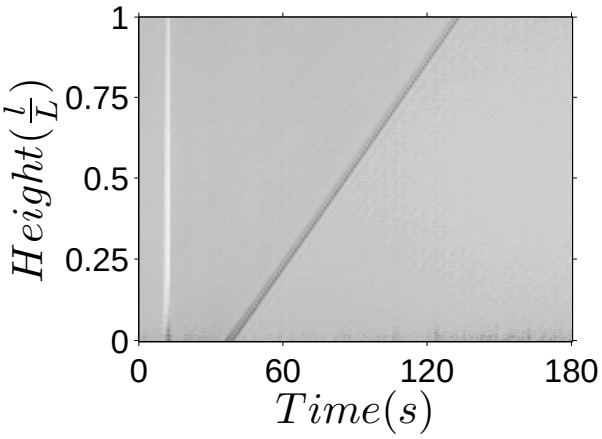

Figure 3.9: Stable single pulse photo sequence (a) and spatiotemporal plot (b) of a single pulse experiment. $Q_1 = 15.4$ ml/s, $Q_1' = 2.6$ ml/s, $Q_2 = 15.2$ ml/s, $T' = 1$ s. 100 cm of test pipe is shown in (a) and 120 cm is shown in (b).

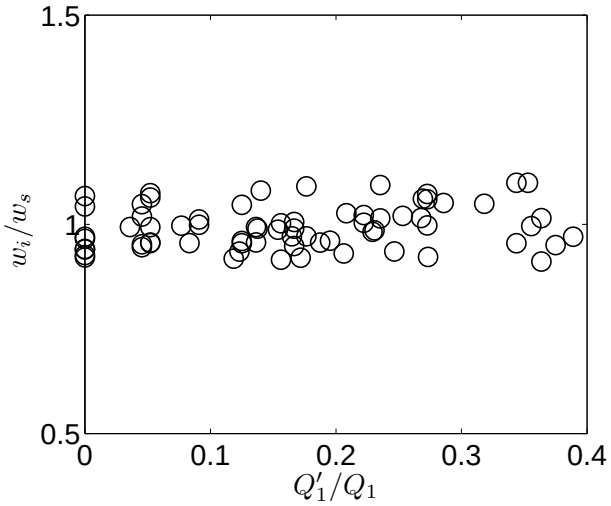

Figure 3.10: Plot of the measured speed of frozen-in structures divided by the speed of the fluid-fluid interface, for approximately 80 experiments.

against Q_1'/Q_1. Each experiment has been categorized as either unstable, producing stable structures, or producing no structures. It can be see that when Q_1'/Q_1 is closer to unity, it is more likely that frozen structures will not be observed. It appears that for a structure to freeze into the interface requires a significant drop in Q_1, i.e. large relative amplitude. However, if the pulse duration is long, then the larger amplitude pulses also risk destabilising the flow.

The results are presented in 3.11. The pulses that froze in were generally created from pulses in which $\frac{Q_1'}{Q_1}$ was less than 0.3. Instabilities were frequently observed when $\frac{Q_1'}{Q_1}$ was less than 0.1. Additionally, graphs of three different values of Q_2 (10, 20, 30 $\frac{ml}{s}$) show that instabilities could be produced at all values of Q_2. Graphs of constant T' show that instabilities are more common observed at higher T'. Large amplitude pulses lasting more than 6 seconds generally produced mixing resembling that after a complete restart of the system and pulses longer than this were not explored.

Figure 3.12 shows the variation in flow regime for changes in Q_2 for different fixed flow rates (10, 20, 30 ml/s). Frozen-in structures are observed largely independent of Q_2 and below a threshold $Q_1'/Q_1 < 0.3$. Instabilities arise for $Q_1'/Q_1 < 0.1$ at longer durations of pulse $T > 2$ s. It is not clear what the relevant timescale is that would enable extension of these results

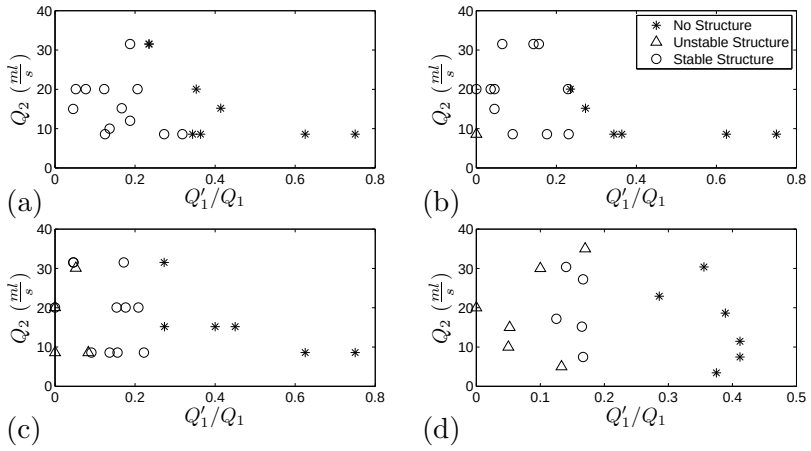

Figure 3.11: Observed flow regimes for different durations of pulse (T'), plotted against Q_1'/Q_1 and Q_2 for different single pulse experiments. (a) 1 second, (b) 2 second, (c) 4 seconds (d) 6 second.

more generally.

3.4 Experiments with Visco-elastic Fluids

Although in the previous section we have seen that it is possible to freeze structures into the interface following imposition of a single pulse, the results were unsatisfactory in some respects. Firstly, the shapes that were frozen in were not particularly well-defined or controlled. Secondly, we found that introducing additional pulses before the stable structures had exited the pipe often resulted in interfacial instability and mixing. In order to stabilize the flows so as to have more flexibility in the flow controls used, we turned to a visco-elastic core fluid (PEO).

In [8] it was found that, provided the base core-annular flow had a interfacial radius smaller than the inlet radius, the PEO tended to stabilize the VPL flows. Here, sequences of pulses are introduced to this regime. Different PEO concentrations were used in order to assess the effects of elasticity and viscosification on the inner fluid, i.e. increasing the PEO concentration increases viscosity as well as elasticity.

Generally speaking, pulses applied to a stable carbopol/PEO core-annular

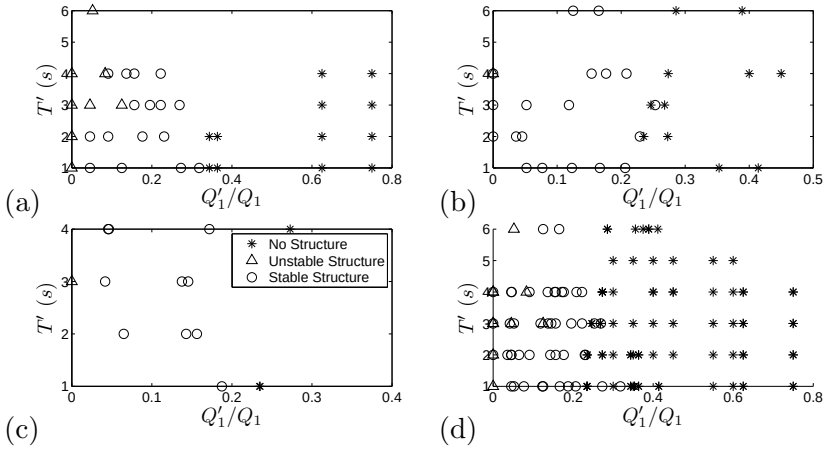

Figure 3.12: Observed flow regimes for different durations fixed Q_2, plotted against Q_1'/Q_1 and T for different single pulse experiments. (a) 10 ml/sec, (b) 20 ml/sec, (c) 30 ml/sec.(d) presents the entire experimental matrix.

flow were seen to create stable structures for a wide range of relative amplitudes. Figure 3.13 shows the range of behaviours observed for single pulse experiments. Low concentration (0.25%) PEO was found to be mostly unstable. At moderate concentrations (0.4%), where the shear viscosity of PEO was similar to that of xanthan over the range of experimental shear rates, we can observe a wider range of parameters that lead to stable flows (compare Fig. 3.11d and Fig. 3.13b). This suggests that fluid elasticity can play a significant role in freezing in stable structures.

Higher concentrations of PEO (0.5%) increase both the elasticity and viscosity of the inner fluid, both of which may have stabilizing effects. This further increases the range of flows for which stable structures are found; see Fig. 3.13a. We also see that it is easier to freeze in stable structures even for longer pulse durations (compare Fig. 3.11a and Fig. 3.13d).

Apart from the increased prevalence of stable structure, use of PEO as the inner fluid also gave rise to better defined shapes than xanthan, typically of a diamond form. The increased stability allowed for experiments with repeated pulsation, which led to strings of diamonds. Figure 3.14 shows examples of "diamond necklaces" produced with 0.4% and 0.5% PEO. The remaining experiments sought to understand how to control frequency,

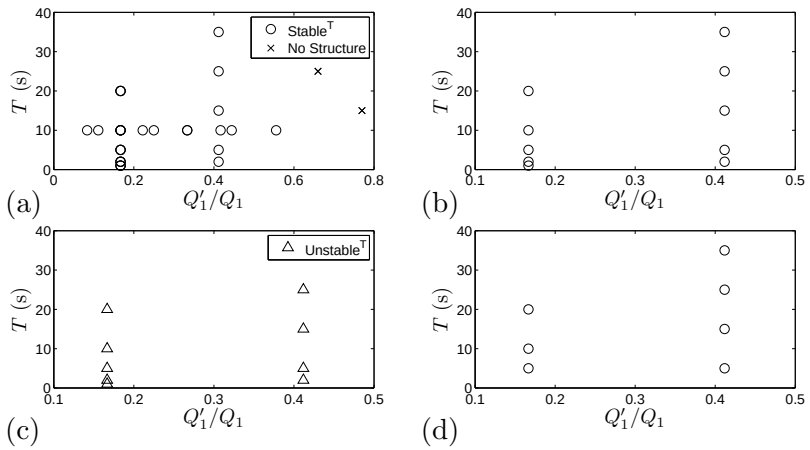

Figure 3.13: (a), (b), (c). The flow regimes observed during single pulse experiments with 3 different concentrations of PEO as the inner core fluid and T' =1 s. (a) 0.5% PEO, (b)0.4% PEO, (c) 0.25% PEO. (d) Flow regimes observed for 0.5% PEO and $T' = 6$ s.

amplitude and shape of the diamond patterns. Apart from the flow rates and relative amplitude of the pulses, the pulse spacing T and pulse duration T' were varied.

3.4.1 Pulse Duration and Spacing

Changing pulse duration $T\prime$ did not create any significant effects for pulse durations $6 > T\prime > 1$ second. Durations below 1 second, resulted in in very small or no visible interfacial shape being frozen in. For durations greater than 6 seconds, the flow exhibited an instability similar to that observed during some flow start-ups. Local instability/mixing propagated along the pipe until the entire flow destabilized. For this reason, $T\prime = 1$ second pulses were used for the majority of experiments with PEO. This maximized the possible range of pulse spacing that could be investigated in the flow loop.

For pulse durations between 1 and 6 seconds, the diamond shape was always observed. Upon close inspection, the shape is created by a single "step change" as the flow rate returns from $Q_1\prime$ to Q_1 and is a form of swelling/overshoot as the radius adjusts to its equilibrium value. The process of diamond structure formation can be seen in Figure 3.14, where the diamond forms near the end of the development region, close to the nozzle exit.

Figure 3.15 shows the effect of varying pulse spacing on the spacing of the diamond shapes. As might be expected, shorter T produces a correspondingly shorter distance between diamonds. For large T the diamonds remain segregated and apparently independent. However, below some critical pulse duration we begin observe interaction between successive diamonds. Here, for $T = 2$ we see an interesting satellite diamond pattern, whereby each second diamond is smaller; see Fig. 3.15 (c). At still higher frequencies, no uniform strands between the diamonds could be observed. Presumably in this range acceleration effects of the pulsing dominate the formation process.

As the inner fluid flow rate is pulsed between Q_1 and Q_1', the velocity of the unyielded plug in the base flow would also be expected to vary. The interfacial (or in this case plug) velocities can be calculated from the base flows of §2.11.1, say w_i and w_i', respectively. A simple prediction of the wavelength λ, between successive diamonds, is given by

$$\lambda \approx w_i T + w_i' T', \tag{3.4}$$

i.e. assuming the diamond structures are frozen in and advected at the plug speed of the base flows. Figure 3.16 shows the measured relationship between λ and $w_i T + w_i' T'$ for multiple pulsation experiments using 0.5% PEO. As

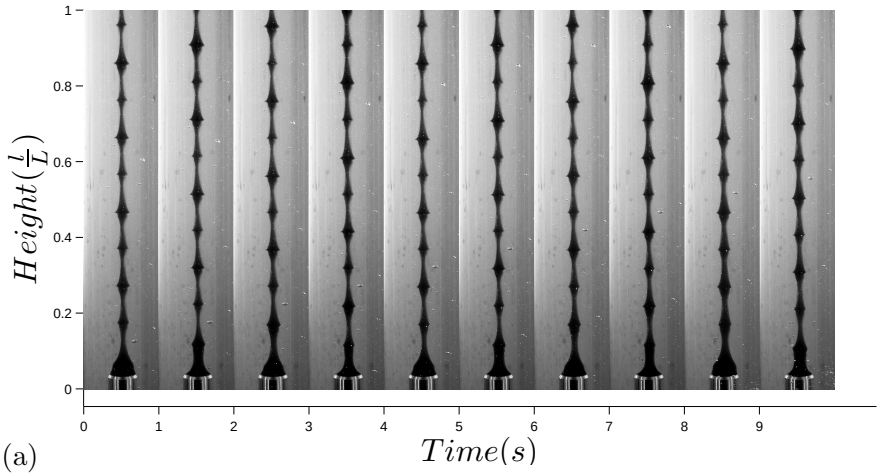

(a)

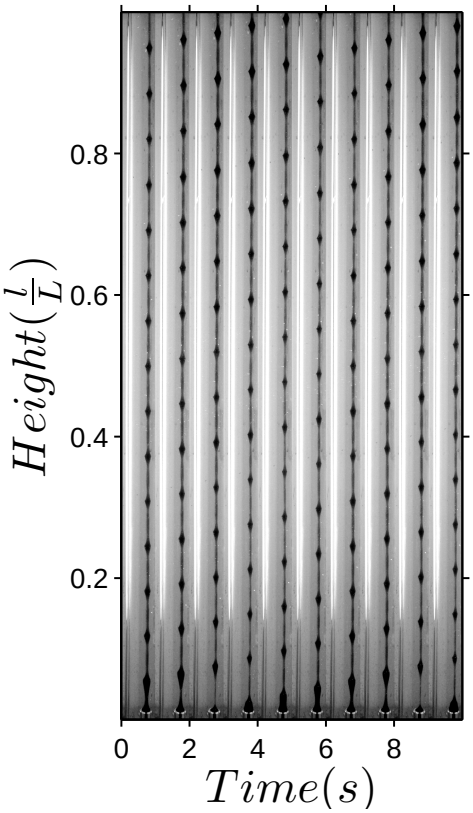

(b)

Figure 3.14: Sequences of images showing the continuous formation of a stable "diamond necklace" pattern. (a) 0.5% PEO, $T = 2$s, $T' = 1$s, relative amplitude $Q_1'/Q_1 = 0.167$, $Q_1 = 10.0\frac{ml}{s}$, $Q_2 = 10.0\frac{ml}{s}$, images show 45 cm section of test pipe. (b) 0.4% PEO,$T = 10$s, $T' = 1$s, relative amplitude $Q_1'/Q_1 = 0.17$, $Q_1 = 15.4\frac{ml}{s}$, $Q_2 = 8.6\frac{ml}{s}$, images show 100 cm section of test pipe.

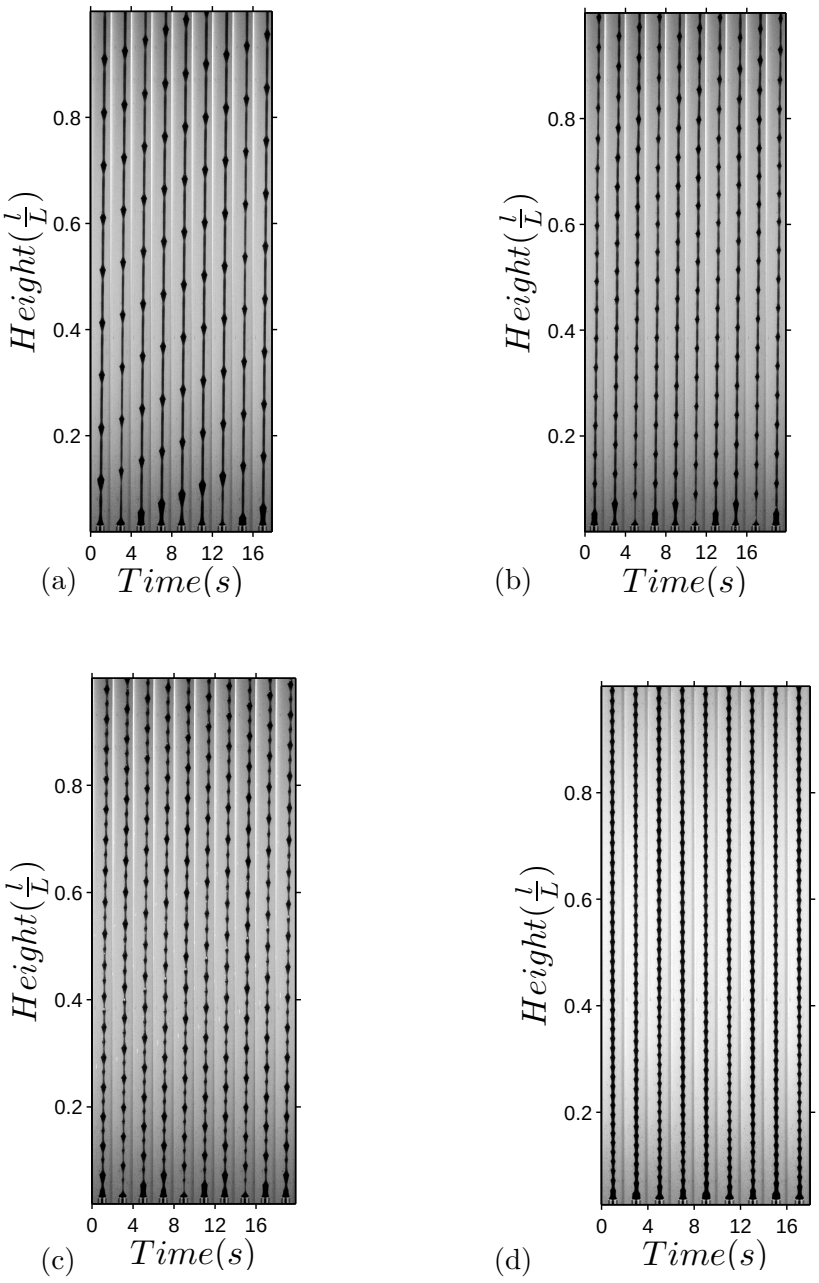

Figure 3.15: Frequency effects on the formation and retention of "diamond necklace" patterns: a) $T = 10$s; b) $T = 5$s; c) $T = 2$s; d) $T = 1$s. Other parameters: $Q_1 = 22\frac{ml}{s}$, $Q_2 = 15\frac{ml}{s}$, relative amplitude $Q_1'/Q_1 = 0.1$, 0.5% PEO is used, $T' = 1$s. Approximately 100cm of the test pipe is shown.

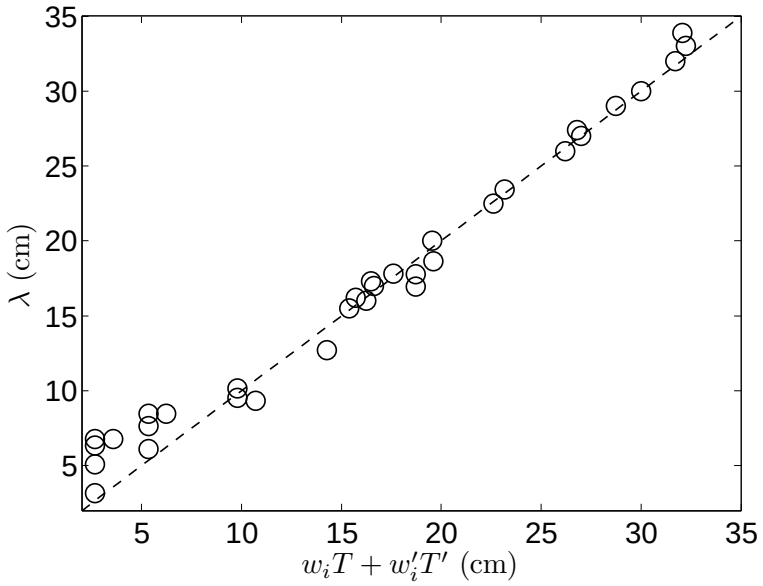

Figure 3.16: Plot of the measured wavelength between diamonds, λ, and the simple prediction of $w_iT + w_i'T'$, for 34 experiments conducted with 0.5% PEO and 0.5% carbopol.

can be seen, the simple prediction of Figure 3.4 is followed reasonably closely for longer wavelengths. As the majority of the experiments had $T' = 1$s, the long wavelengths in practice correspond to larger pulse spacings T.

For lower wavelengths a nonlinear departure from Figure 3.4 is seen. This nonlinearity is associated with the onset of the alternating pattern of large and small diamonds (e.g. Fig. 3.15c), which was observed widely in experimental sequences at lower T; see e.g. also Figure 3.14b. This critical T is associated with the a development time (or length) required in order to establish the base flow uniform interfacial radius r_i.

Changing pulse relative amplitude

Pulse relative amplitude was observed to affect the size of the diamond shapes. Figure 3.17a shows the change in size of the diamonds resulting from

different relative amplitudes, for two different experimental sequences with different pairs of (Q_1, Q_2). The chief variation occurred between relative amplitudes of $0.3 - 0.1$. For relative amplitudes above 0.3 the size of the diamond structures was barely visible. Below this threshold there was a nonlinear increase in the amplitude of the diamonds shapes, leveling out for relative amplitudes below about 0.2. Figure 3.17b shows examples of the change in shape of the diamond structures with relative amplitude.

3.4.2 Other Experiments

Figure 3.18 (a) and (b) show the core fluid injector being displaced by roughly 10 mm, held for 10 seconds, and then returned to the center. A VPL flow with a 'country road' shape results. Figure 3.19 shows an experiment performed with glycerol. Glycerol did produce VPL flows, but large scale mixing occurred in all cases less than a single transit time (ie, $L_{apparatus}/w_i$) after the introduction of multiple pulses. A 'pearl necklace' shape structure was seen compared to the diamond necklace with viscoelastic core fluid.

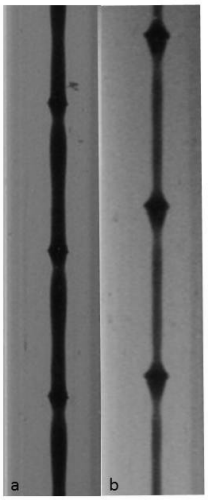

(a) (b)

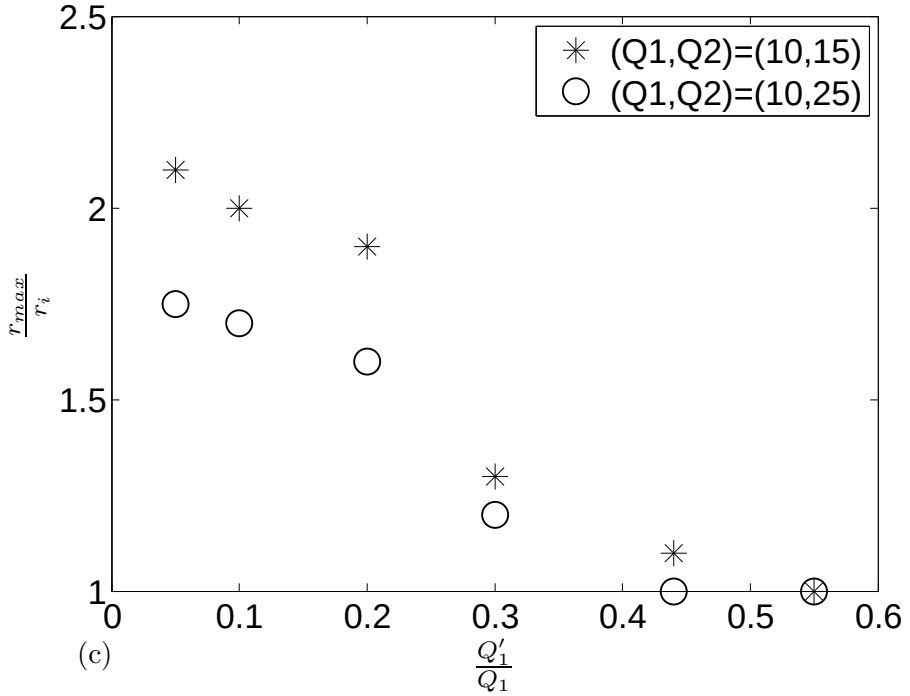

(c)

Figure 3.17: Images showing diamond shapes with (a) relative amplitude of 0.36 and (b) relative amplitude of 0.17. (c) Structure size response to relative amplitude for two flow rates.

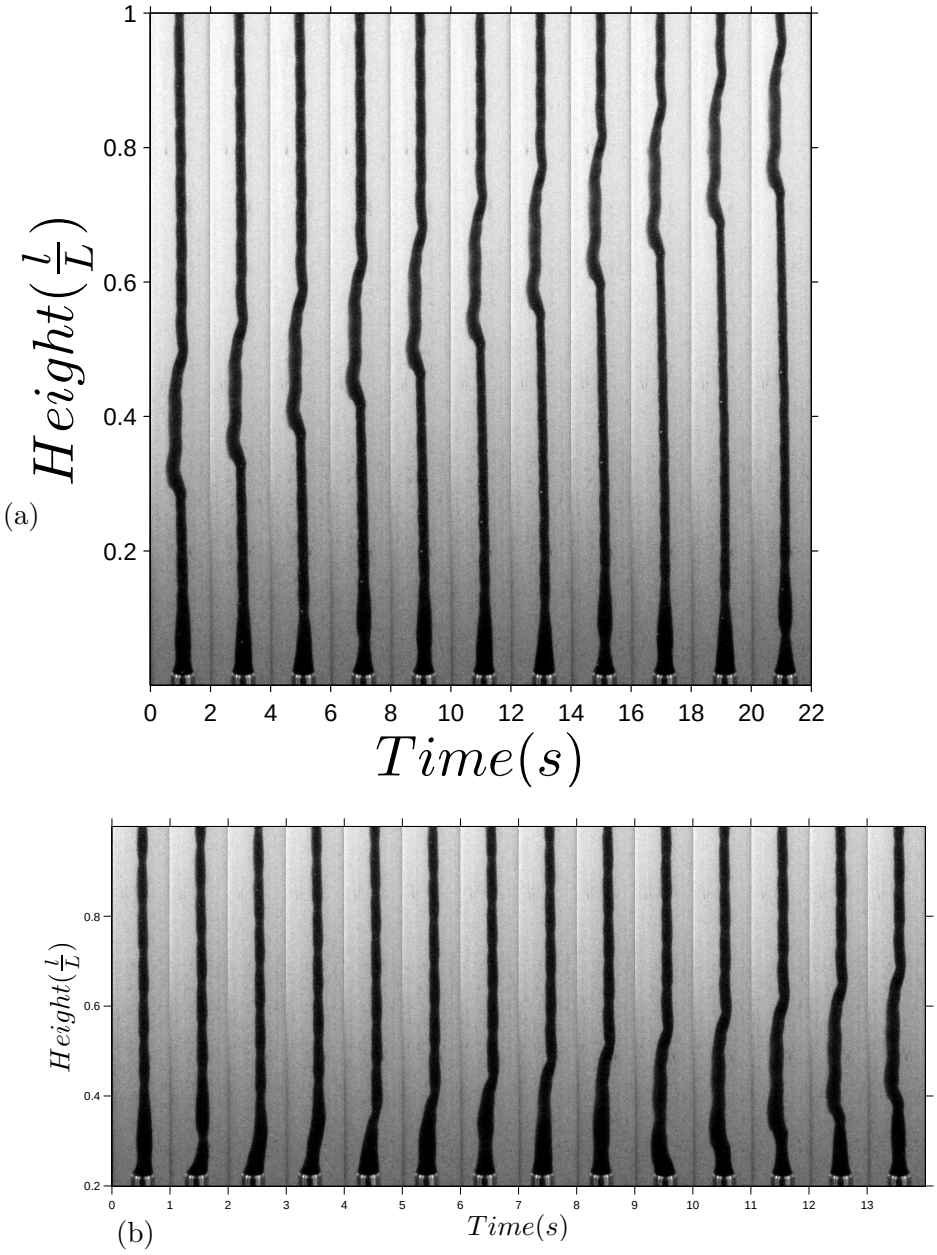

Figure 3.18: (a) An example of another effect; displacing the core fluid to produce a 'country road' shape with 0.5% PEO and carbopol. (b) Formation of the country road. Q_1 =12, Q_2 =8 $\frac{ml}{s}$.

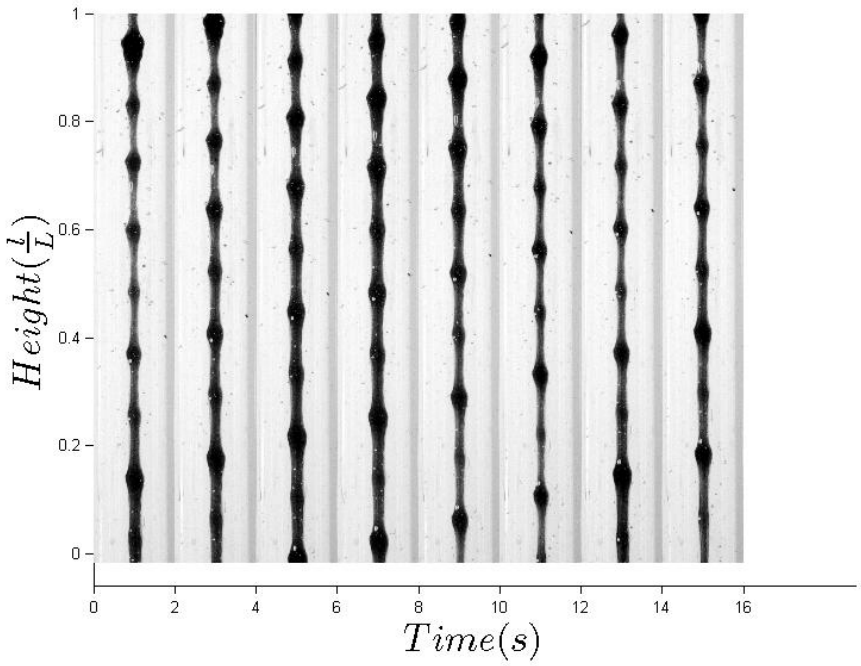

Figure 3.19: Experiment done using glycerol as the core fluid. Q_1 =15, Q_1' =3, Q_2 =15 $\frac{ml}{s}$, T = 10, T' =1 second.

Chapter 4

Contributions and Future Research Directions

4.1 Contributions of the Thesis

This thesis has presented original research contributing to the understanding of VPL flows and the possibility of "freezing in" different interfacial shapes, other than a uniform core-annular interface. This can be viewed as a form of near net shape forming process. Within the range of parameters studied in this thesis, VPL flows have been shown to behave in the following ways:

- Introducing step changes to VPL flows with power law core fluids creates a 'yield front' that travels the length of the test pipe at a velocity that scales well with $\bar{w}_1'$. This yield front represents the transition between two "base flows", found at flow rates (Q_1, Q_2) and (Q_1', Q_2), respectively.
- Introducing singe pulse changes to a VPL flow with a power law core fluid was observed to result in one of three cases:
  1. A stable structure is formed within the initial VPL flow.
  2. The flow becomes yielded and large scale mixing occurs.
  3. The VPL flow returns to the initial state with no structure formed.
- Introducing multiple pulses to a VPL flow with a viscoelastic core fluid will result in multiple stable structures existing simultaneously.
- The 'diamond necklace' pattern seen in VPL flows with viscoelastic core fluids is consistent and robust across many flow rates.
  - Controlling the shape of the structures could not be accomplished by changing the flow rates alone. Shape is also a complex function of the fluid rheology.
  - By changing the relative amplitude of the pulses, we were able to very the maximum amplitude of the frozen-in diamond structures.

  - The spacing of the diamonds in a diamond necklace is relatively easy to control. At spacial frequencies that are shorter than the flow development length, we begin to observe more interference in the form of satellite structures that freeze in between diamonds.

4.2 Future Research Directions

Some future research directions of VPL flows include the following.

- Studying additional near net shape related effects such as perturbing the core fluid to create 'country road' or helical geometries.
- Experimenting with a prototype moulding machine that extrudes polymer melts as either the core or annular fluid.
- Experimenting with VPL pipeline lubrication in an industrial setting.
- Experimentally encapsulating droplets of various types of fluids within an unyielded layer of yield stress fluid.

Bibliography

[1] M. d'Olce, J. Martin, N. Rakotomalala, D. Salin, and L. Talon. Pearl and mushroom instability patterns in two miscible fluids' core annular flows. *Physics of Fluids.*, 20:024104, 2008.

[2] I.A Frigaard. Super-stable parallel flows of multiple visco-plastic fluids. *J. Non-Newtonian Fluid Mech.*

[3] C.E Hickox. Instability due to viscosity and density stratification in axisymetric pipe flow. *The Physics of Fluids*, 14(2):251–262, February 1971.

[4] A.P Hooper and W.G Boyd. Shear flow instability at the interface between two viscous fluids. *J. Fluid Mech.*

[5] S. Hormozi. Multiayer flows with yield stress fluids. *PhD Thesis.*

[6] S. Hormozi, G. Dunbrack, and I.A. Frigaard. Stable core-annular fows of viscoelastic fluids using the visco-plastic lubrication technique. *Annual Transactions of the Nordic Rheology Society.*, 20, 2012.

[7] S. Hormozi, D.M Martinez, and I.A. Frigaard. Stable core-annular fows of viscoelastic fluids using the visco-plastic lubrication technique. *J. Non-Newtonian Fluid Mech.*, 166:1356–1368, 2011.

[8] S. Hormozi, K. Wielage-Burchard, and I.A. Frigaard. Entry, start up and stability effects in visco-plastically lubricated pipe flows. *J. Fluid Mech.*, 673:432–467, 2011.

[9] C.K. Huen.

[10] C.K. Huen, Frigaard I.A, and Martinez D.M. Experimental studies of multi-layer flows using a visco-plastic lubricant. *J. Non-Newtonian Fluid Mech..*, 142:150–161, 2007.

[11] Moyers-Gonzalez M.A, Frigaard I.A, and Nouar C. Nonlinear stability of a visco-plastically lubricated vsicous shear flow. *J. Fluid Mech.*, 506:117–146, 2004.

[12] M.A Moyers-Gonzalez, I.A Frigaard, and Nouar C. Stable two-layer flows at all re; visco-plastic lubrication of shear-thinning and viscoelastic fluids. *J. Non-Newtonian Fluid Mech.*, 165:1578–1587, 2010.

[13] C.S Yih. Instability due to viscosity stratification. *J. Fluid Mech.*, 27(2):337–352.

Appendix A

List of Experiments

In tables A.1,A.2,A.3 and A.3 we catalogue the main experimental parameters tested.

A.1 Step Change Experiments

A.2 Single Pulse Experiments

A.3 Experiments with Visco-Elastic Fluids

ID	$Q_1(\frac{ml}{s})$	$Q'_1(\frac{ml}{s})$	$Q_2(\frac{ml}{s})$	Q'_1/Q_1
S1	21.9	9.0	7.4	0.4
S2	21.9	9.0	11.5	0.4
S3	23.1	9.0	18.6	0.4
S4	23.1	8.2	28.4	0.4
S5	24.7	1.3	30.1	0.1
S6	24.7	8.2	27.2	0.3
S7	27.5	4.1	30.4	0.1
S8	28.8	3.9	22.9	0.1
S9	32.9	8.2	17.2	0.3
S10	24.9	4.1	15.2	0.2

ID	$Q_1(\frac{ml}{s})$	$Q'_1(\frac{ml}{s})$	$Q_2(\frac{ml}{s})$	Q'_1/Q_1
S11	24.9	4.1	7.4	0.2
S12	41.2	15.4	3.4	0.4
S13	48.0	8.0	5.0	0.2
S14	48.0	8.0	20.0	0.2
S15	48.0	8.0	25.0	0.2
S16	48.0	8.0	42.5	0.2
S17	37.2	4.4	5.0	0.1
S18	48.8	15.3	5.0	0.3
S19	20.6	2.6	11.5	0.1
S20	25.7	7.7	11.5	0.3
S21	30.9	15.4	17.2	0.5
S22	15.4	2.6	15.8	0.2
S23	28.3	14.1	15.8	0.5
S24	33.4	5.1	15.8	0.2
S25	33.4	3.9	40.1	0.1
S26	33.4	12.9	40.1	0.4

Table A.1: Table of step change experiments performed for 0.5% Xanthan and 0.5% carbopol. Q_1 is the core fluid flow rate before the step change in introduced, Q'_1 is the core fluid flow rate after the step change in introduced, Q_2 is the annular fluid flow rate that remains constant during these experiments.

ID	$Q_1(\frac{ml}{s})$	$Q'_1(\frac{ml}{s})$	Q'_1/Q_1	$Q_2(\frac{ml}{s})$	T'
P1	32.9	7.7	0.2	31.5	1.0
P2	28.3	0.0	0.0	31.5	3.0
P3	28.3	7.7	0.3	31.5	4.0
P4	21.9	5.1	0.2	31.5	1.0
P5	16.5	2.8	0.2	31.5	4.0
P6	20.6	2.8	0.1	31.5	3.0
P7	21.9	7.7	0.4	20.1	1.0
P8	21.9	5.1	0.2	20.1	2.0
P9	20.3	5.1	0.3	20.1	3.0
P10	21.9	3.9	0.2	20.1	4.0
P11	24.9	5.1	0.2	20.1	1.0
P12	24.7	5.7	0.2	20.1	2.0
P13	36.5	9.0	0.2	20.1	3.0
P14	24.7	5.1	0.2	20.1	4.0
P15	24.7	1.3	0.1	20.1	1.0
P16	28.3	1.3	0.0	20.1	2.0
P17	24.7	1.3	0.1	20.1	3.0
P18	33.4	5.1	0.2	20.1	4.0
P19	33.4	2.6	0.1	20.1	1.0
P20	28.3	0.0	0.0	20.1	2.0
P21	34.7	4.1	0.1	20.1	3.0
P22	35.7	0.0	0.0	20.1	4.0
P23	33.4	4.1	0.1	20.1	1.0
P24	35.7	1.3	0.0	20.1	2.0
P25	32.9	0.0	0.0	20.1	3.0
P26	32.9	0.0	0.0	20.1	4.0
P27	20.6	2.6	0.1	8.6	1.0
P28	33.4	7.7	0.2	8.6	2.0
P29	33.4	9.0	0.3	8.6	3.0
P30	28.3	2.6	0.1	8.6	4.0
P31	33.4	0.0	0.0	8.6	1.0
P32	34.7	0.0	0.0	8.6	2.0
P33	34.7	0.0	0.0	8.6	3.0
P34	34.7	0.0	0.0	8.6	4.0

ID	$Q_1(\frac{ml}{s})$	$Q'_1(\frac{ml}{s})$	Q'_1/Q_1	$Q_2(\frac{ml}{s})$	T'
P35	28.3	7.7	0.3	8.6	1.0
P36	28.3	2.6	0.1	8.6	2.0
P37	32.9	6.4	0.2	8.6	3.0
P38	28.3	3.9	0.1	8.6	4.0
P39	28.3	9.0	0.3	8.6	1.0
P40	21.9	3.9	0.2	8.6	2.0
P41	20.6	2.6	0.1	8.6	3.0
P42	15.4	1.3	0.1	8.6	4.0
P43	28.3	10.3	0.4	8.6	1.0
P44	28.3	10.3	0.4	8.6	2.0
P45	23.1	5.1	0.2	8.6	3.0
P46	23.1	5.1	0.2	8.6	4.0
P47	20.6	15.4	0.8	8.6	1.0
P48	20.6	15.4	0.8	8.6	2.0
P49	20.6	15.4	0.8	8.6	3.0
P50	20.6	15.4	0.8	8.6	4.0
P51	16.5	10.3	0.6	8.6	1.0
P52	16.5	10.3	0.6	8.6	2.0
P53	16.5	10.3	0.6	8.6	3.0
P54	16.5	10.3	0.6	8.6	4.0
P55	16.5	5.7	0.3	8.6	1.0
P56	16.5	5.7	0.3	8.6	2.0
P57	21.9	9.0	0.4	7.4	6.0
P58	21.9	9.0	0.4	11.5	6.0
P59	23.1	9.0	0.4	18.6	6.0
P60	23.1	8.2	0.4	30.4	6.0
P61	28.8	8.2	0.3	22.9	6.0
P62	41.2	15.4	0.4	3.4	6.0
P63	28.3	7.7	0.3	15.2	2.0
P64	28.8	7.7	0.3	15.2	3.0
P65	32.9	9.0	0.3	15.2	4.0
P66	32.9	13.6	0.4	15.2	1.0
P67	28.3	1.3	0.0	11.0	3.0
P68	24.7	1.3	0.1	30.1	4.0
P69	24.7	1.3	0.1	5.0	5.0
P70	24.7	1.3	0.1	15.0	6.0

ID	$Q_1(\frac{ml}{s})$	$Q'_1(\frac{ml}{s})$	Q'_1/Q_1	$Q_2(\frac{ml}{s})$	T'
P71	24.7	4.1	0.2	27.2	6.0
P72	27.5	3.9	0.1	30.4	6.0
P73	32.9	4.1	0.1	17.2	6.0
P74	24.9	4.1	0.2	15.2	6.0
P75	24.7	4.1	0.2	7.4	6.0
P76	16.5	2.6	0.2	8.6	3.0
P77	16.5	2.6	0.2	8.6	4.0
P78	28.3	1.3	0.0	15.0	1.0
P79	28.3	1.3	0.0	15.0	2.0
P80	28.3	3.9	0.1	10.0	1.0
P81	41.2	7.7	0.2	12.0	1.0
P82	15.4	2.6	0.2	15.2	1.0
P83	27.8	1.3	0.0	31.5	4.0
P84	30.9	1.3	0.0	31.5	3.0
P85	19.8	1.3	0.1	31.5	2.0
P86	28.3	1.3	0.0	31.5	4.0
P87	27.0	3.9	0.1	31.5	2.0
P88	16.5	3.1	0.2	31.5	1.0
P89	28.3	4.1	0.1	31.5	3.0
P90	16.5	2.6	0.2	31.5	2.0

Table A.2: Table of single pulse experiments performed for 0.5% xanthan and 0.5% carbopol. T' is the time spent at Q'_1 during the reduced flow pulse.

ID	$Q_1(\frac{ml}{s})$	$Q_1'(\frac{ml}{s})$	$Q_2(\frac{ml}{s})$	Q_1'/Q_1	T'	T
V1	15.4	3.1	8.6	0.2	1	20
V2	15.4	3.1	8.6	0.2	1	10
V3	15.4	3.1	8.6	0.2	1	5
V4	15.4	3.1	8.6	0.2	1	2
V5	21.9	8.7	24.3	0.4	1	20
V6	21.9	8.7	24.3	0.4	1	10
V7	21.9	8.7	24.3	0.4	1	5
V8	21.9	8.7	24.3	0.4	1	2
V9	21.9	8.7	24.3	0.4	1	1
V10	30.9	6.2	35.8	0.2	1	20
V11	30.9	6.2	35.8	0.2	1	10
V12	30.9	6.2	35.8	0.2	1	5
V13	30.9	6.2	35.8	0.2	1	2
V14	30.9	6.2	35.8	0.2	1	1
V15	30.9	1.5	35.8	0.05	2	20
V16	30.9	1.5	35.8	0.05	2	10
V17	30.9	1.5	35.8	0.05	2	5
V18	30.9	1.5	35.8	0.05	2	2
V19	30.9	1.5	35.8	0.05	2	1
V20	30.0	1.5	15.0	0.05	1	10
V21	30.0	3.0	15.0	0.1	1	10
V22	30.0	6.0	15.0	0.2	1	10
V23	30.0	9.0	15.0	0.3	1	10
V24	30.0	12.9	15.0	0.43	1	10
V25	30.0	12.7	15.0	0.55	1	10
V26	23.1	1.2	14.3	0.05	1	10
V27	23.1	4.6	14.3	0.2	1	10
V28	23.1	5.8	14.3	0.25	1	10
V29	23.1	6.9	14.3	0.3	1	10
V30	23.1	10.1	14.3	0.44	1	10
V31	23.1	12.7	14.3	0.55	1	10

Table A.3: Table of experiments performed for 0.5% PEO and 0.5% carbopol. T' is the time spent at the reduced flow (Q_1') and T is the time spent at the base flow (Q_1).

ID	$Q_1(\frac{ml}{s})$	$Q_1'(\frac{ml}{s})$	$Q_2(\frac{ml}{s})$	$\frac{Q_1'}{Q_1}$	$T_{Q_1'}$	T_{Q_1}
V32	15.4	3.1	8.6	0.2	1.0	20.0
V33	15.4	3.1	8.6	0.2	1.0	10.0
V34	15.4	3.1	8.6	0.2	1.0	5.0
V35	15.4	3.1	8.6	0.2	1.0	2.0
V36	15.4	3.1	8.6	0.2	1.0	1.0
V37	21.9	8.7	24.3	0.4	1.0	20.0
V38	21.9	8.7	24.3	0.4	1.0	10.0
V39	21.9	8.7	24.3	0.4	1.0	5.0
V40	21.9	8.7	24.3	0.4	1.0	2.0
V41	21.9	8.7	24.3	0.4	1.0	1.0

Table A.4: Table of experiments performed for 0.4% PEO and 0.5% carbopol.

Appendix B

Detailed Experimental Procedures

B.1 Startup

- Turn on computer, power Box, and four fluorescent apparatus lights.
- Turn on cameras both cameras and individually focus the lenses until an 12 point font on 8x11 paper can be read at full zoom.
- Connect suction side of SP500 pump to core fluid with a push on fitting and tighten hose clamp.
- Connect suction side of SP1000 pump to annular fluid with a push on fitting and tighten hose clamp.
- Open valves on core and annular fluid buckets.
- Check level of overflow drain and empty if there is any fluid in it.
- Set RPM of 1000 series carbopol pump to 144 rpm and allow annular fluid to fill test pipe and flush through until clear fluid fills the test pipe.
- Stop SP1000 pump.
- Turn off laboratory lighting.

B.2 Experiments

- Perform startup procedure.
- Start Labview.

- Turn on sp1000 pump and sp500 pump to desired Q_1' and Q_2 using RPM and fit to double check flowrate displayed on front pannel of 'dualflowcontrol.vi'. Turn ps500 pump rpm up until flow rate reaches desired Q_1.
- Allow flow to stabilize.
- Turn on Power to solenoid valve.
- Open throttling valve
- Open Solenoid valve by writing code and compiling to Arduino microprocessor.
- Adjust throttling valve until flow rate read on front panel of 'dualflowcontrol.vi' in Labview is at Q_1'.
- Close throttling valve.
- Write program to input stepchange, single pulse, multiple pulse (loop single pulse with delay time of xxxxx ms to throttling valve.
- Turn on cameras to interval timing mode setting frequency and number of shots or HD video to capture entire experiment on SD memory cards.
- Compile Arduino program and monitor flow rates and overflow drain level until experiment is over (> 1 transit time).
- Allow a single transit time before next experiment.

B.3 Fluid Preparation

- Place bucket on postal scale.
- Use hose and gate valve to fill a 40 L bucket with lower valve attachments, with 40.00 kg of tap water.
- Allow water to sit for 60 mins to degas.
- Plug mixer into timer.
- Put on a respirator and safety glasses.
- Measure out desired quantity of powder on analytical balance.

- Put mixer with stainless steel blades in water bucket and turn on to 300 rpm.
- Slowly add powder to water with a spoon.
- Set timer and leave to mix for 10 hours.
- (Carbopol) Add 26 grams of NaOH to carbopol and mix for 20 more mins.
- (Carbopol) Use pH meter to check pH is around 6.0. Add NaoH as necessary to raise pH to 7.0.
- (Core fluids) Add 50 ml of fountain pen ink and mix for 5 minutes.

Appendix C

Computer Programs

C.1 Mutilayer Flow Curves

```
1
2
3 %datadir='L:\May25';
4 Ty=57.2;
5 n1=0.50; %Xanthan
6 n2=0.28; %Carbopol
7 k1=1.37;%Xanthan
8 k2=45.4;%Carbopol
9
10
11 R=.0254;
12 ni=100;
13 nj=100;
14
15 Ri(1)=.0005;
16 for i=2:ni
17       Ri(i)=Ri(i-1)+.0005;
18 end
19 dp(1)=280.0;
20 for j=2:nj
21       dp(j)=dp(j-1)+280.0;
22 end
23 for j=1:nj
24       Ri1(j)=Ri(j)*1000;
25 dp1(j)=dp(j)/1000;
26 end
27
28 [X,Y] = meshgrid(Ri1,dp1) ;
29 for j=1:nj
```

```
30      for i=1:ni
31 Ry(j)=2*Ty/(dp(j));
32          if Ry(j)>Ri(i)
33          B1(j)=((dp(j)*(1/(2*k1)))^(1/n1))/((1/n1)+1);
34          B2(j)=((dp(j)*(1/(2*k2)))^(1/n2))/((1/n2)+1);
35          ui(i,j)=B2(j)*(R-Ry(j))^((1/n2)+1);
36          uc(i,j)=B1(j)*(Ri(i))^((1/n1)+1)+ui(i,j);
37          Q1(i,j)=(pi*uc(i,j)*Ri(i)^2-2*pi*B1(j)*(Ri(i)
                ^((1/n1)+2))*(Ri(i)/((1/n1)+3)))*10^6;
38      gamma1(i,j)=Q1(i,j)*10^-6/(pi*Ri(i)^3);
39          Q2(i,j)=(pi*ui(i,j)*(R^2-Ri(i)^2)-2*pi*B2(j)*(
                R-Ry(j))^((1/n2)+2)*(((R-Ry(j))/((1/n2)+3))
                +(Ry(j)/((1/n2)+2))))*10^6;
40          gamma2(i,j)=Q2(i,j)*10^-6/(pi*(.0254^2-Ri(i)
                ^2)*.0254);
41      Beta(i,j)=0;
42
43 end
44          if Ry(j)<=Ri(i)
45          B1(j)=((dp(j)*(1/(2*k1)))^(1/n1))/((1/n1)+1);
46          B2(j)=((dp(j)*(1/(2*k2)))^(1/n2))/((1/n2)+1);
47          ui(i,j)=B2(j)*(((R-Ry(j))^((1/n2)+1))-((Ri(i)-
                Ry(j))^((1/n2)+1)));
48          uc(i,j)=B1(j)*(Ri(i))^((1/n1)+1)+ui(i,j);
49          alpha(i,j)=(R-Ry(j))^((1/n2)+2)*(((R-Ry(j))
                /((1/n2)+3))+(Ry(j)/((1/n2)+2)))-(Ri(i)-Ry(
                j))^((1/n2)+2)*(((Ri(i)-Ry(j))/((1/n2)+3))
                +(Ry(j)/((1/n2)+2)));
50      Q1(i,j)=(pi*uc(i,j)*Ri(i)^2-2*pi*B1(j)*(Ri(i))
            ^((1/n1)+2)*(Ri(i)/((1/n1)+3)))*10^6;
51          gamma1(i,j)=Q1(i,j)*10^-6/(pi*Ri(i)^3);
52      Q2(i,j)=(pi*(R^2-Ri(i)^2)*(ui(i,j)+B2(j)*(Ri(i)-Ry
            (j))^((1/n2)+1))-2*pi*B2(j)*alpha(i,j))*10^6;
53          gamma2(i,j)=Q2(i,j)*10^-6/(pi*(.0254^2-Ri(i)
                ^2)*.0254);
54      Beta(i,j)=-20.0;
55
56 end
57          if Ry(j)>R
58          B1(j)=((dp(j)*(1/(2*k1)))^(1/n1))/((1/n1)+1);
```

```
59            uc(i,j)=B1(j)*(Ri(i))^((1/n1)+1);
60            Q1(i,j)=(pi*uc(i,j)*Ri(i)^2-2*pi*B1(j)*(Ri(i))
                  ^((1/n1)+2)*(Ri(i)/((1/n1)+3)))*10^6;
61        gamma1(i,j)=Q1(i,j)*10^-6/(pi*Ri(i)^3);
62        Q2(i,j)=0;
63        gamma2(i,j)=Q2(i,j)*10^-6/(pi*(.0254^2-Ri(i)^2)
              *.0254);
64        Beta(i,j)=20.0;
65
66    end
67
68    end
69
70    end
71    for i=1:ni
72        for j=1:nj
73            Beta2(i,j)=Beta(j,i);
74            Q1p(i,j)=Q1(j,i);
75            Q2p(i,j)=Q2(j,i);
76            gammap1(i,j)=gamma1(j,i);
77            gammap2(i,j)=gamma2(j,i);
78        end
79    end
80    xx1(1)=.1;
81     yy1(1)=2*Ty/xx1(1);
82    for i=2:250
83        xx1(i)=xx1(i-1)+0.1;
84        yy1(i)=2*Ty/xx1(i);
85    end
86    xx1(251)=25.0;
87    yy1(251)=30.0;
88    xx1(252)=xx1(55);
89    yy1(252)=30.0;
90    %#######
91    xx2(1)=0.0;
92     yy2(1)=0.866;
93    for i=2:250
94        xx2(i)=xx2(i-1)+0.1;
95        yy2(i)=.866;
96    end
```

```
97 xx2(251)=25.0;
98 yy2(251)=0.866;
99 xx2(252)=25.0;
100 yy2(252)=0.0;
101 xx2(253)=0.0;
102 yy2(253)=0.0;
103
104 figure1=figure;
105 h1 = gcf;
106 set(h1,'Position',[100   100   600   500]); % sets the
      size and shape of the window on your screen
107 h = axes('Visible','off','Parent',figure1,'Position'
      ,[0 0 1 1],'Color',[0.8 0.8 0.8]); % defines the
      drawing area as [0,1] x [0,1]
108 axes1=axes('Parent',figure1,'Position',[.2 .2 .7 .7],'
      FontSize',24,'Color',[0.8 0.8 0.8]); % set your
      axes within that unit square
109
110
111
112
113 % % figure1=figure;
114 % % axes('Visible','off','Parent',figure1,'Position
      ',[0 0 1 1],'Color',[0 1 1]);
115 % % axes1 = axes('Parent',figure1,'Position',[0.2 0.2
      0.6 0.6],'FontSize',18,'Color',[0 1 0]);
116
117
118 % Uncomment the following line to preserve the X-
      limits of the axes
119 % xlim([0 1]);
120 % Uncomment the following line to preserve the Y-
      limits of the axes
121 % ylim([0 100]);
122
123
124 box('on');
125 hold on
126 fill(xx1,yy1,[0.7 0.7 0.7]);
127 fill(xx2,yy2,[0.85 .85 .85 ]);
```

```
128 xlabel('$r_i(mm)$','Interpreter','latex','FontSize'
      ,24);
129 ylabel('$p_z(kPa/m)$','Interpreter','latex','FontSize'
      ,24);
130 xlim([0. 25]);
131 ylim([0 15]);
132 % Create textbox
133 annotation(figure1,'textbox',[0.2198 0.4783 0.1333
      0.05094],...
134     'Interpreter','latex',...
135     'String',{'Stable'},...
136     'FontWeight','bold',...
137     'FontSize',24,...
138     'FitBoxToText','off',...
139     'LineStyle','none',...
140     'BackgroundColor','none');
141
142 % Create textbox
143 annotation(figure1,'textbox',[0.2194 0.2480 0.0926
      0.005043],...
144     'Interpreter','latex',...
145     'String',{'Static'},...
146     'FontWeight','bold',...
147     'FontSize',24,...
148     'FitBoxToText','off',...
149     'LineStyle','none',...
150     'BackgroundColor',[0.85 0.85 0.85]);
151
152 % Create textbox
153 annotation(figure1,'textbox',[0.6911 0.6068 0.1326
      0.01843],...
154     'Interpreter','latex',...
155     'String',{'Unstable'},...
156     'FontWeight','bold',...
157     'FontSize',24,...
158     'FitBoxToText','off',...
159     'LineStyle','none',...
160     'BackgroundColor',[0.7 0.7 0.7]);
161 hold on
162 contour(X,Y,Q1p,'ShowText','on','LineWidth',2,...
```

```
163     'LevelList',[ 1   60 ]);
164 hold on
165
166 % Create contour
167 contour(X,Y,Q2p,'ShowText','on','LineWidth',2,...
168     'LevelList',[1   60]);
169 hold off
170 fname = [datadir 'dp_R_75'];
171 print(gcf,'-depsc', '-noui','-r200',fname);
172 saveas(gcf,'dp_R_75.fig');
173 figure2=figure;
174 h1 = gcf;
175  set(h1,'Position',[100   100   600   500]); % sets
       the size and shape of the window on your screen
176  h = axes('Visible','off','Parent',figure2,'Position'
       ,[0 0 1 1],'Color',[1 1 1]); % defines the drawing
        area as [0,1] x [0,1]
177  axes1=axes('Parent',figure2,'Position',[.2 .2 .7 .7],
       'FontSize',24,'Color',[0 1 0]); % set your axes
       within that unit square
178
179
180 box('on');
181 hold on
182 fill(xx1,yy1,[0.7 0.7 0.7]);
183 fill(xx2,yy2,[0.85 .85 .85 ]);
184 xlabel('$r_i(mm)$','Interpreter','latex','FontSize'
      ,24);
185 ylabel('$p_z(kPa/m)$','Interpreter','latex','FontSize'
      ,24);
186 xlim([0. 25]);
187 ylim([0 4]);
188 % Create textbox
189 annotation(figure2,'textbox',[0.687 0.4347 0.1277
      0.05094],...
190     'Interpreter','latex',...
191     'String',{'Unstable'},...
192     'FontWeight','bold',...
193     'FontSize',24,...
194     'FitBoxToText','off',...
```

```
195      'LineStyle','none',...
196      'BackgroundColor','none');
197
198 % Create textbox
199 annotation(figure2,'textbox',[0.687 0.4403 0.1333
       0.05094],...
200      'Interpreter','latex',...
201      'String',{'Stable'},...
202      'FontWeight','bold',...
203      'FontSize',24,...
204      'FitBoxToText','off',...
205      'LineStyle','none')%,...
206      %'BackgroundColor',[0 1 0]);
207
208 % Create textbox
209 annotation(figure2,'textbox',[0.687 0.2768 0.1326
       0.01843],...
210      'Interpreter','latex',...
211      'String',{'Static'},...
212      'FontWeight','bold',...
213      'FontSize',24,...
214      'FitBoxToText','off',...
215      'LineStyle','none',...
216      'BackgroundColor','none');
217 hold on
218 [C,h]=contour(X,Y,Q1p,'ShowText','on','LineWidth',2,'
       linestyle','-.',...
219      'LevelList',[ 10 20 40  70 ],'color','k');
220 clabel(C,h,'FontSize',24,'Color','k','Rotation',0,'
       LabelSpacing',340);
221 hold on
222
223 % Create contour
224 [C,h]=contour(X,Y,Q2p,'ShowText','on','LineWidth'
       ,2,... %'linestyle','-.',
225      'LevelList',[10 20 40  60],'color','k');
226 clabel(C,h,'FontSize',24,'Color','k','Rotation',0,'
       LabelSpacing',340);
227 % Create textbox
```

```
228 annotation(figure2,'textbox',[0.1227 0.044 0.1123
    0.08],...
229     'Interpreter','latex',...
230     'String',{'(a)'},...
231     'FontSize',28,...
232     'FontName','AlArabiya',...
233     'FitBoxToText','off',...
234     'LineStyle','none');
235
236 hold off
237 fname = [datadir 'Geoff'];
238 print(gcf,'-depsc', '-noui','-r200',fname);
```

C.2 Photo Sequence

```
1 %Written by Geoffrey Dunbrack, UBC Mechanical
    Engineering, 2013
2 %Takes .jpg photo files in a folder and produces an
    enhanced sequence of photos with
3 %the backgound light subtracted from the pixel matrix
4
5 %%
6 clear;
7 datadir='C:\Users\Geoffrey\Desktop\PEO & glycerine
    experiments\0.4% PEO\';
8  images=dir([datadir,'*.JPG']);
9  iimages=imread([datadir,images(1).name]);
10
11  average=mean2(iimages(700:4833,4355:4500));
12  for i=1:length(images) %228%
13
14 iimages=imread([datadir,images(i).name]);
15 iimages=rgb2gray(iimages);
16 iimages=iimages(700:4833,4355:4822);
17 iimages=iimages+0.3*average;
18 iimages = imadjust(iimages);
19 iimages = medfilt2(iimages);
20 S(:,:,i)=iimages;
21  end
22
```

```
23  %%
24 width=467;
25
26  close all
27  hold all
28  k=1;
29 for i=1:10
30
31      X(:,width*(i-1)+1:width*i+1)=S(:,:,k);
32
33      k=k+1;
34 end
35 close all
36 hold on;
37 imshow(X);
38 xlabel('$Time(s)$','Interpreter','latex','FontSize'
       ,24);
39 ylabel('$Height (\frac{l}{L})$','Interpreter','latex',
       'FontSize',24);
40 axis on
41 set(gca, 'XTick',[1:467:4671]);
42 set(gca,'XTickLabel',[0:1:10]) ;
43 set(gca,'YTick',[1:827:4134]);
44 set(gca,'YTickLabel',[1  0.8  0.6  0.4  0.2  0.0]);
```

C.3 Inverted Flow Problem

```
1
2 %Equation for the inverted multilayer flow problem.
      Accepts Global variables Q1, Q2
3 %and takes a 1x2 martix 'X' from 'invertedflowproblem.
      m'
4 %January 28 2013, Author: Geoffrey Dunbrack, UBC MECH,
       geoffdunbrack@gmail.com
5
6 function F=inverted(x)%R,Ry1,Ry2,k1,k2,n1,n2,Q1,Q2)
7 global Q1;
8 global    Q2;
9 R=0.0254;
10 Ry1=0;
```

```
11
12
13 %increasing ty2 increases pressure gradient and lowers
       Ri
14 ty2=57.4;
15
16 %Ri is directly proportional to k1. Does nto effect dp
      /dz very much
17 k1=0.8;
18 k2=45;
19 n1=0.6;
20
21 %increases pressure gradient and lowers Ri
22 n2=0.28;
23
24 % combined equations for solver
25 F=[pi*((((x(1)*(1/(2*k1))).^(1/n1))/(1/n1+1))*((x(2)-
       Ry1).^(1/n1+1))+(((x(1)*((1/(2*k2))).^(1/n2)))/(1/
       n2+1)*(R-(2*ty2/x(1))).^(1/n2+1))) ...
26 *(x(2).^2)-2*pi*((x(1)*(1/(2*k1))).^(1/n1))/(1/n1+1))
       *((x(2)-Ry1).^(1/n1+2))*((x(2)-Ry1)/(1/n1+3)+Ry1
       /(1/n1+2))-Q1;
27
28 pi*(((x(1)*(1/(2*k2))).^(1/n2)/(1/n2+1))*(R-2*ty2/x(1)
       ).^(1/n2+1))*(R.^2-x(2).^2)-2*pi*((x(1)*(1/(2*k2)))
       .^(1/n2)/(1/n2+1)) ...
29 *(R-(2*ty2/x(1))).^(1/n2+2)*((R-(2*ty2/x(1)))/(1/n2+3)
       +(2*ty2/x(1))/(1/n2+2))-Q2];
30
31
32 end
```

C.4 Spatiotemporal Plot

```
1 clear;
2 datadir='C:\Users\Geoffrey\Desktop\MSc Research\
      EXPERIMENTS\2012SinglePulse Experiments\DEC15_PULSE
      \subsetNS2\';
3
4  images=dir([datadir,'*.JPG']);
```

```
 5  for i=1:length(images) %228%
 6 % iImage=imread([datadir,images(i).name]);
 7 % iImage=rgb2gray(iImage);
 8 % H=iImage(:,1810:1920);
 9 % M(:,:,i)=H;
10 iimages=imread([datadir,images(i).name]);
11 iimages=rgb2gray(iimages);
12 iimages=iimages(:,2660:2822);
13 level=graythresh(iimages);
14 bw=im2bw(iimages,level);
15 H=medfilt2(bw);
16 S(:,:,i)=H;
17
18
19  end
20 figure,imshow(S(:,:,10));
21 for i=1:length(images)
22 for j=200:3650
23  for k=1:size(S,2)
24      M(j-199,k,i)= S(j,k,i);
25  end
26 end
27 end
28
29  figure,imshow(M(:,:,10));
30 %%
31  p=zeros([3450  3586]);
32  M=double(M);
33 for i=1:1:length(images) %228%
34 for j=1:1501
35 for k=1:size(M,2)
36 p(j,i)=p(j,i)+M(j,k,i);
37 end
38 end
39 end
40  for i=1:1:length(images) %228%
41 for j=1:1501
42 p(j,i)=p(j,i)/(size(M,2));
43 end
44  end
```

```
45
46
47 figure1 = figure;
48 colormap('gray');
49 % Create axes
50 axes('Visible','off','Parent',figure1,'Position',[0 0
       1 1]);
51 xlim([2 10]);
52 ylim([500 1501]);
53 % Create axes
54 axes1 = axes('Parent',figure1,...
55     'YDir','reverse',...
56     'FontSize',16,...
57     'CLim',[0.8 1]);
58 %% Create axes
59  axes1 = axes('Parent',figure1,...
60      'XTickLabel',{'0','10','20','30','40','50','60'
          },...
61      'XTick',[1 301 601 901 1201 1501 1801 ],...
62      'YTickLabel',{'80', '70', '60', '50', '40', '30',
          '20','10'},...%      'YTick',[31 86 141 196
          251 306 361 416],...
63      'YDir','reverse',...
64      'FontSize',16,...
65      'CLim',[50 110]);
66 % Uncomment the following line to preserve the X-
       limits of the axes
67 % xlim([1 length(images)]);
68 %% Uncomment the following line to preserve the Y-
       limits of the axes
69 %  ylim([1 1501]);
70
71
72 % Uncomment the following line to preserve the Y-
       limits of the axes
73
74
75  hold('all');
76 box('off');
77 % Create contour
```

```
78 contour(p,'LineColor','none','LevelStep',.1,'Fill','on
    ','Parent',axes1);
79 %% Create xlabel
80 % xlabel('$t(s)$','Interpreter','latex','FontSize',20)
    ;
81 %
82 %% Create ylabel
83 % ylabel('$h(cm)$','Interpreter','latex','FontSize
    ',20,...
84 %     'HorizontalAlignment','left');
85 % %imagesc(p),colormap(gray);
86
87 xlabel('$frame$','Interpreter','latex','FontSize',20);
88
89 % Create ylabel
90 ylabel('$pixel$','Interpreter','latex','FontSize'
    ,20,...
91     'HorizontalAlignment','left');
92 %imagesc(p),colormap(gray);
93
94
95 fname = [datadir 'spatio2'];
96 print(gcf,'-depsc2', '-noui','-r200',fname);
97 saveas(gcf,'spatio2.fig');
```

C.5 Yield Front Speed Analysis

```
1 %Creates spatiotemporal plots from a folder of jpg
    images.
2 %Geoffrey Dunbrack, Complex fluids Lab, UBC
3 %read .jpg images from specified folder into a vector
    of size
4 %Nx1('images'), N is number of images in folder
5
6 clear;
7 %%
8 datadir='C:\Users\Geoffrey\Desktop\MSc Research\
    EXPERIMENTS\2012stepchangeexperiments\SEPT25\
    SEPT25A\camera2\';
9
```

```
10
11
12  images=dir([datadir,'*.jpg']);
13
14  top_row=100;
15  bottom_row=3000;
16  num_row_avg=10;
17  %YY_axis=zeros(num_row_avg,length(images));
18  %S=zeros(num_row_avg,length(images));
19  %A=zeros(num_row_avg);
20  %y_axis=zeros(num_row_avg);
21  number_section=10;
22  spaceing=(bottom_row-top_row)/number_section;
23
24
25
26  %iimages=rgb2gray(iimages);
27
28 % iimages=iimages(top_row+j*(spaceing):(top_row+j*(
       spaceing)+num_row_avg),3030:3130);
29
30 iimages=imread([datadir,images(1).name]);
31 for j=1:number_section
32
33 iiimages=iimages(top_row+(j-1)*(spaceing):(top_row+(j
       -1)*(spaceing)+num_row_avg),3040:3090);
34 level=graythresh(iiimages);
35 iiimages=im2bw(iiimages,level);
36
37 A_background(j,:)=mean2(iiimages);
38
39
40 end
41
42
43
44  %%
45 step_thru=1:4:length(images);
46
47  for i=1:length(step_thru) %228%
```

```
48
49
50
51 %iimages=iimages(top_row+j*(spaceing):(top_row+j*(
       spaceing)+num_row_avg),3030:3130);
52 iimages=imread([datadir,images(step_thru(i)).name]);
53
54 %level=graythresh(iimages);
55 iimages=rgb2gray(iimages);
56
57 for j=1:number_section
58
59
60     iiimages=iimages(top_row+(j-1)*(spaceing):(top_row
           +(j-1)*(spaceing)+num_row_avg),3040:3100);
61     level=graythresh(iiimages);
62     iiimages=im2bw(iiimages,level);
63      A(j,:)=mean2(iiimages);
64      y_axis(j,:)=(top_row+j*(spaceing)+5);
65      A_normalized(j,:)=A(j,:)/A_background(j,:);
66
67 end
68 %iimages=iimages(1500:3000,3030:3130);
69 %A=iimages(2900:3000,3030:3130);
70 %B=mean2(A);
71 %T=mean2(iimages(100:200,3030:3130));
72
73
74
75 %H=medfilt2(bw);
76
77 S(:,i)=A_normalized;
78 YY_axis(:,i)=y_axis;
79 %U(i)=T;
80
81 i=i+4
82
83
84  end
85 %%
```

```
86 close all
87 %for j=1:10
88
89 i=1:31%length(images)
90 for j=1:10
91
92       plot(i,(1-S(j,:)),'-*k');
93     hold on
94
95 end
96 l=ones(length(images));
97 y=-0.1*l
98 x=1:length(images);
99 plot(y,'-k');
100
101  %inittopcon=U(1);
102  %initbotcon=S(1);
103  %i=1
104 % x=0
105  %y=0
106  %while abs(S(i)- initbotcon)<0.05*initbotcon
107  %      x=x+1
108  %      i=i+1
109  %end
110  %i=1
111
112  % while (abs(S(i)- inittopcon)<0.05*inittopcon) && (i
         < length(S))
113  %      y=y+1
114  %      i=i+1
115  %end
```